KERNFORSCHUNGSANLAGE JÜLICH GmbH
Institut für Reaktorentwicklung

INVESTIGATION OF NEUTRON SPECTROMETERS AS FUSION PLASMAS DIAGNOSTIC METHODS

von
Mona Mobasher

Jül-2094
November 1986
ISSN 0366-0885

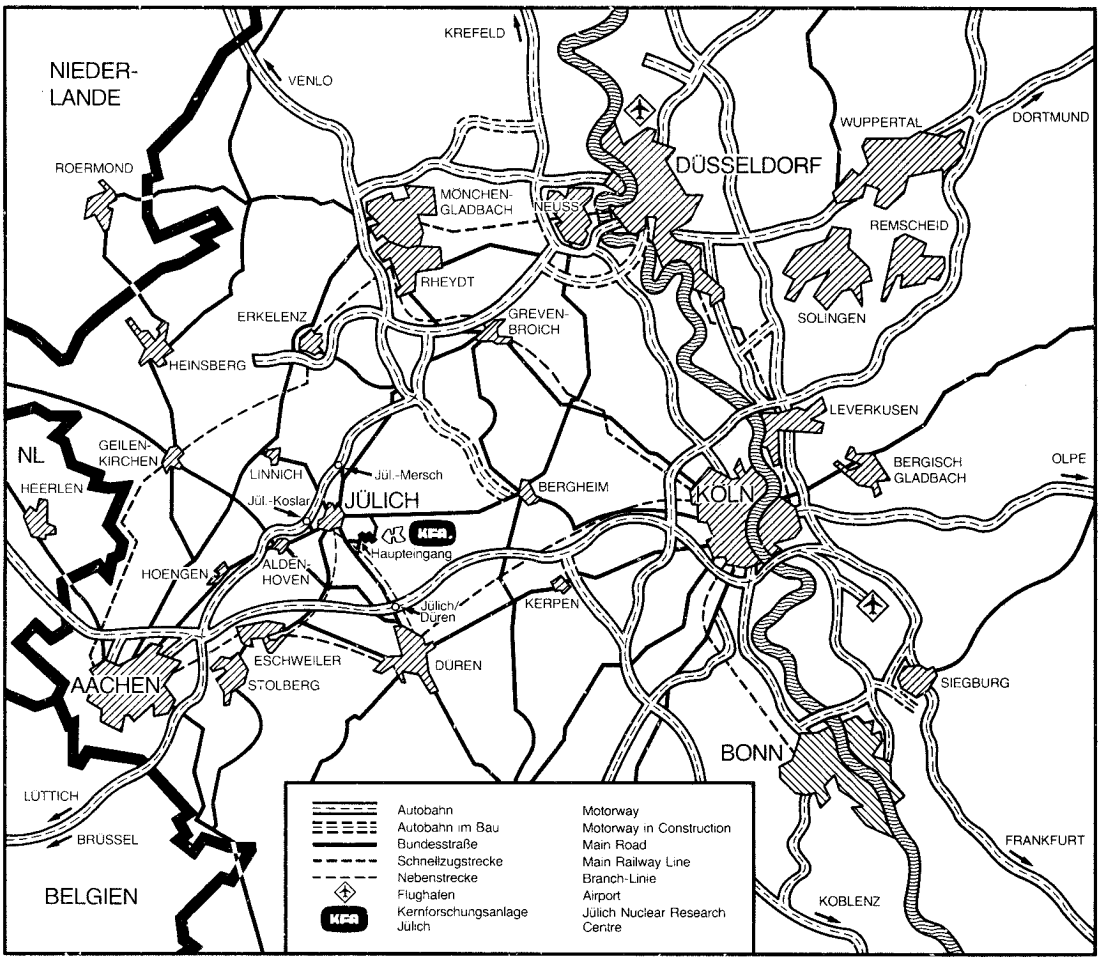

Als Manuskript gedruckt

Berichte der Kernforschungsanlage Jülich – Nr. 2094
Institut für Reaktorentwicklung Jül-2094

Zu beziehen durch: ZENTRALBIBLIOTHEK der Kernforschungsanlage Jülich GmbH
Postfach 1913 · D-5170 Jülich (Bundesrepublik Deutschland)
Telefon: 02461/610 · Telex: 833556-0 kf d

INVESTIGATION OF NEUTRON SPECTROMETERS AS FUSION PLASMAS DIAGNOSTIC METHODS

von

Mona Mobasher

D 82 (Diss. T.H. Aachen)

Abstract

Two neutron spectrometer systems were investigated to be used as fusion plasmas diagnostic methods. The first, NE-213 proton recoil spectrometry system has been assembled with two different detector sizes to be used for both D-D and D-T measurements. The detectors' efficiencies and response functions (Response Matrices) were calculated with CECIL Monte Carlo code. Several improvements have been made for this code to agree with the measurements of this spectrometer. Neutron energy spectra were obtained by unfolding the measured pulse height spectra. The FERDOR unfolding procedure after several improvements have been used in unfolding the measured spectra.

A second neutron spectrometer using a He-3 semiconductor sandwich detector was used to measure the neutron spectrum for D-D neutrons. The efficiency was calculated and the resolution was determined from the neutron energy spectra. These spectrometers approved to be efficient for fusion plasma diagnostics for temperature $\geq$ 1 keV.

TABLE OF CONTENTS

1. INTRODUCTION

1.1 Neutron Diagnostic for Fusion Plasmas

Neutron generation rates due to Deuterium-Deuterium (D-D) or Deuterium-Tritium (D-T) fusion are aboundant in recent and planned experiments. As a result it is now possible to apply spectroscopic techniques used in nuclear physics to neutron diagnostic measurements in advanced fusion experiments, with the objective of deducing the optimum amount of information concerning the parameters of the reacting plasma, such as temperature and density /1/.

Ideally, the neutron diagnostic equipment would function impartially with neutrons of 2.45 MeV from D-D operation and with neutrons of 14.06 MeV from D-T operation. There will inevitably be some small contribution from D-T reactions during D-D reactions and vice-versa. As will be discussed later, the characteristics of neutron spectrometers alter substantially with increasing energy. This circumstance results in a proposal to construct separate spectrometer systems for D-D and D-T operation, although the D-T spectrometer systems may be usable during the later stages of D-D operation where ion densities, and temperatures should be high. In order to specify the required performance for a neutron diagnostic system it is essential to have available estimates of the expected neutron yields, fluxes and energy spectra.

An estimate of the maximum possible neutron yield from a Tokamak machine can be obtained in the following manner. Assume that the ratio of thermonuclear power generated (in a D-T plasma) to heating power provided reaches the desired goal of unity. If the burn time is taken to be 10 seconds, the upper limit to the thermonuclear energy generation will be 100 MJ.

This corresponds to a production of 3.6×10^9 DT neutrons per plasma discharge (or "shot") /2/.

If we assume that the plasma is of uniform density and temperature, and fills the vacuum chamber, the neutron production rate becomes

$$R = 1/4 \, (n_D + n_T)^2 \, \sigma v \quad n/cm^2 s$$

for equimolar DT, where n_D, n_T are the deuterium and tritium density respectively. The value estimated as the upper limit to R can be shown to correspond to an ion density of 3×10^{13} ions/cm^3 (a typical value), reacting at a temperature of 10 keV.

The D-D neutron production will be significantly lower. Adopting the same density and temperature for D-D as for D-T results in a neutron yield about 100 times less than for D-T (a fifty-fold reduction in σv, combined with a factor of two reduction due to there being two fusion reactions for each neutron produced).

In Table 1.1 we present figures for the neutron production rates for D-D and D-T plasmas for a range of ion temperatures, assuming an ion density of 3×10^{13} ions/cm^3. The production rates are found from $1/4 \, n^2 \, \langle \sigma v \rangle$ for D-D and for D-T plasmas, where n is the total ion density. Where /3/

$$\langle \sigma v \rangle_{D-D} = 2.33 \times 10^{-14} \, T^{-2/3} \exp(-18.76 \, T^{-1/3})$$

and

$$\langle \sigma v \rangle_{D-T} = 3.68 \times 10^{-12} \, T^{-2/3} \exp(-19.94 \, T^{-1/3})$$

is used with T in keV. The neutron yields quoted in Table 1.1 are based on the assumption of a plasma volume of 1.64×10^8 cm^3. The flux values refer to a radius (measured from the plasma centre) of 1.5 m and are derived by dividing the yield by the area of the vacuum chamber surface (1.75×10^6 cm^2). These fluxes

correspond to the undirected neutrons escaping from the plasma, with no scattering from surrounding structure, they do not represent neutrons which might enter a neutron spectrometer through a collimator.

A measurement of the neutron yield provides a sensitive indicator of the plasma ion temperature providing the ion density is known. In the absence of reliable density measurements, the ion temperature can be deduced from the Doppler broadening of the fusion neutron energy spectrum. Following Muir /4/, the neutron peak can be shown to be approximately Gaussian shaped

$$S(E) = \frac{1}{W\sqrt{\pi}} \exp\left(-\left(\frac{E-E_0}{W}\right)^2\right)$$

$$W = \left(\frac{4\, m\, E_0\, kT}{m_1 + m_2}\right)^{Y2}$$

The full width at half maximum (FWHM) of the distribution is given by W2√ln2. In this formula m is the neutron mass, whilst m_1 and m_2 refer to the reacting ions. The FWHM for D-D neutrons is 82.41 √KT, with KT in keV, and for D-T neutrons is 176.6 √KT. Fig. 1.1 illustrates the FWHM as a function of temperature for D-D and D-T plasmas, the percentage energy broadening (ΔE/E) is also provided:

$$\Delta E/E = 3.36\ \sqrt{KT}\ \%\ \text{for D-D}$$

and $\Delta E/E = 2.256\ \sqrt{KT}\ \%$ for D-T, KT in keV.

It is interesting to note that the spectrometer energy resolution needed for 2.45 MeV neutrons is less restrictive than that needed for 14.06 MeV neutrons by almost a factor of 3, i.e. if an instrumental resolution of 3.7% is acceptable at 2.45 MeV, the corresponding 14.06 MeV resolution is 2.0%.

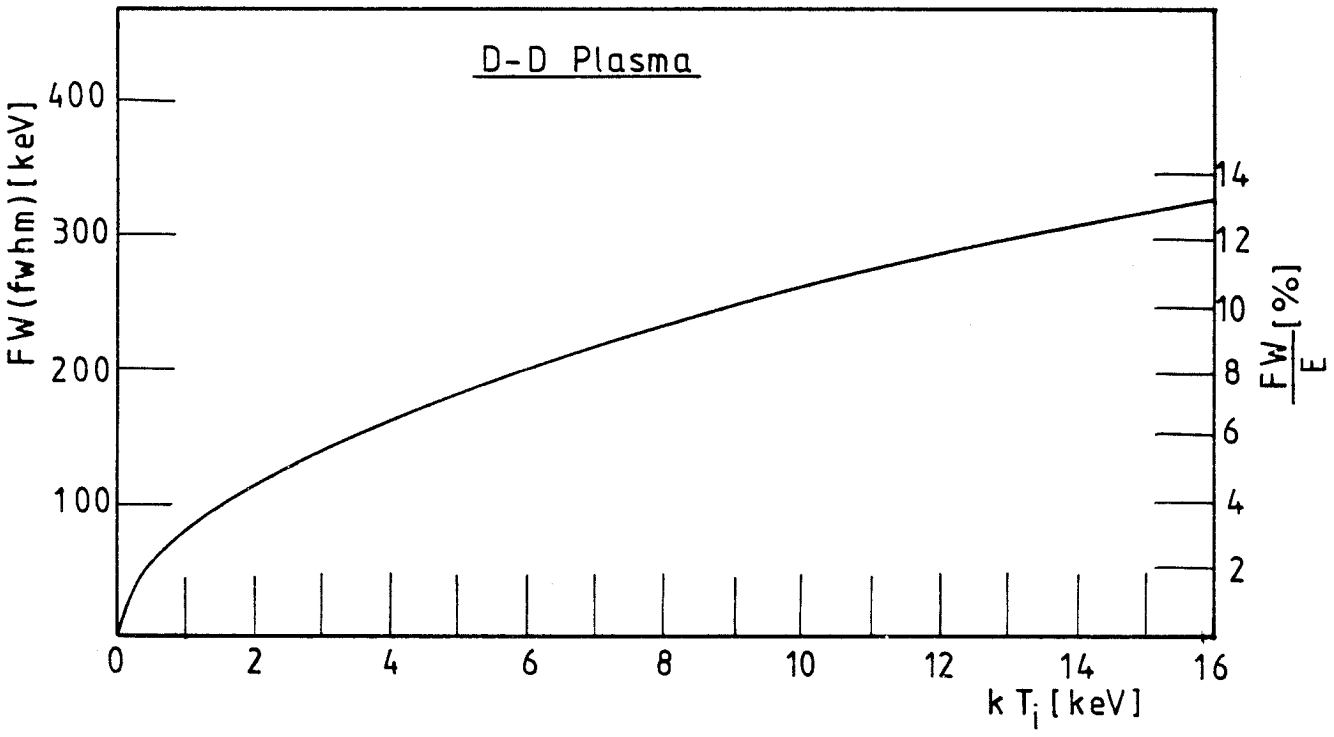

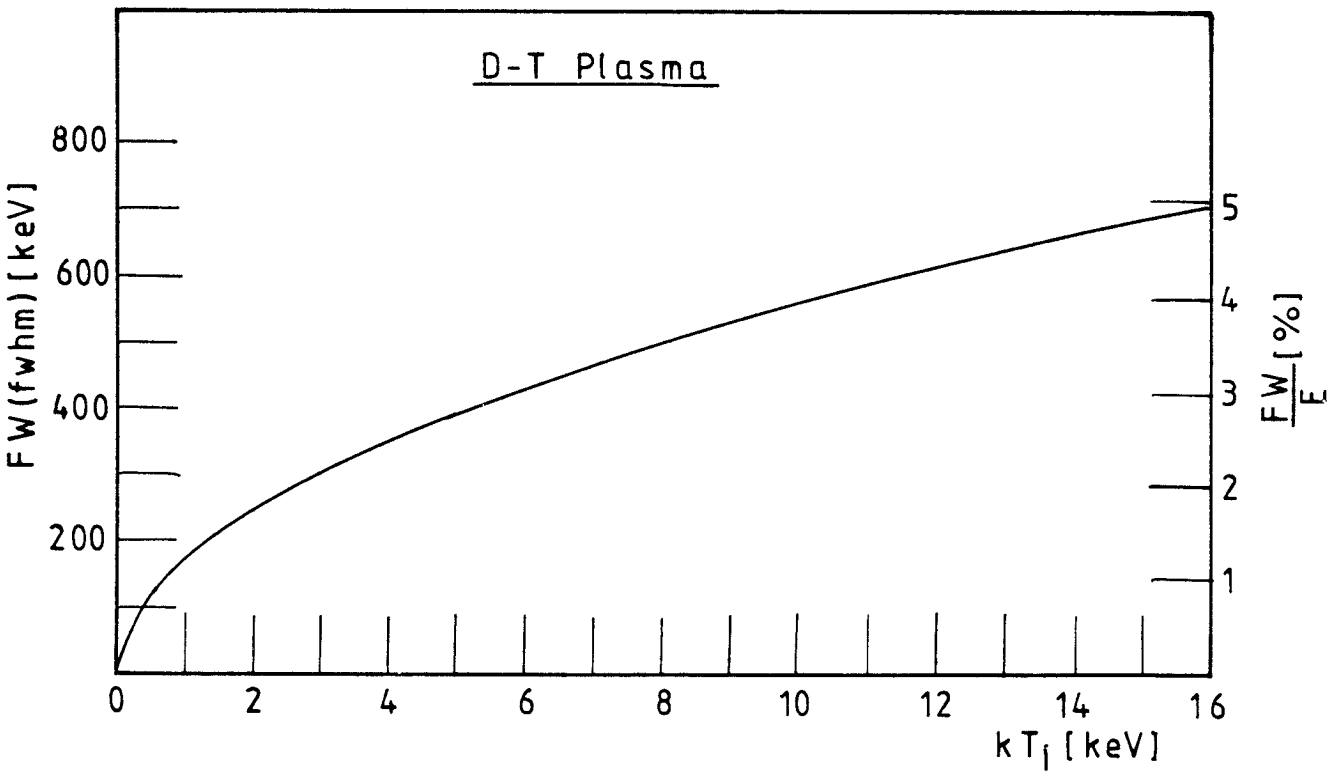

Fig. 1.1: Variation of width of neutron energy distribution with plasma temperature for thermonuclear plasmas

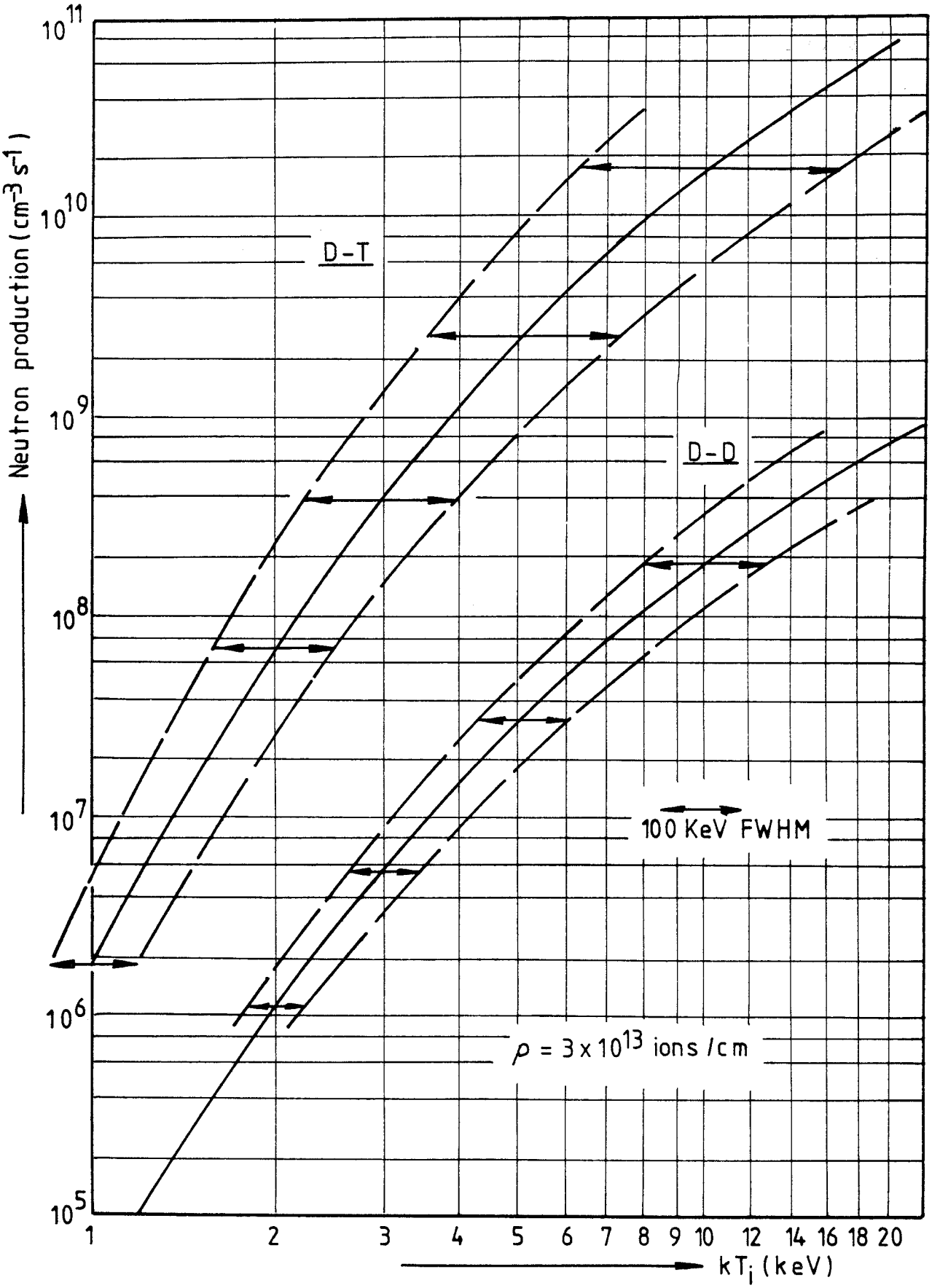

Fig. 1.2: Relationship between neutron production, energy distribution (FWHM) and ion temperature for $n = 3 \times 10^{13}$ n/cm^3

The connection between thermal broadening and neutron yield should be stressed: it is pointless to design a spectrometer for, say 3% resolution with D-D neutrons (implying a capability for determining temperatures down to 1 keV) if the instrumental efficiency proves to be such that a collimated 5 m neutron fluence in excess of, say, 10^7 n/cm^2 is needed (implying T > 15 keV). The correlation between resolution and yield is further illustrated in Fig. 1.2.

Another important result of a neutron spectrum measurement is that it is possible to identify the physical process which generated the neutron from its energy /5/. Five processes are known to be sources of neutrons in a Tokamak machine: photo-neutron reactions, electrodisintegration of deuterium, photo-disintegration of deuterium, thermonuclear fusion of deuterium, and fusion of deuterium and tritium. Photoneutron production, and photodisintegration of deuterium are processes which occur at the ring of molybdenum blocks used to define the plasma discharge (limiter). Electrodisintegration is a volume process but has a cross-section which is several orders of magnitude smaller than the D-D cross section for the particle energies expected in fusion plasmas. All the processes except the thermonuclear D-D and D-T reactions are result of supra-thermal electrons which are produced for some plasma conditions. It is possible to limit the production of these "run-away electrons" by controlling the plasma discharge conditions.

Table 1.1: Neutron production from JET plasmas*

	D-D			D-T		
Temp. (keV)	neutrons / cm^3 sec	Yield (n)	flux** (n/cm^2 s)	neutrons / cm^3 sec	Yield (n)	flux (n/cm^2 s)
1	3.73×10^4	6.1×10^{13}	3.5×10^6	1.81×10^6	3.0×10^{15}	1.7×10^8
2	1.13×10^6	1.8×10^{15}	1.1×10^8	6.98×10^7	1.2×10^{17}	6.5×10^9
3	5.65×10^6	9.2×10^{15}	5.3×10^8	3.94×10^8	6.4×10^{17}	3.7×10^{10}
4	1.53×10^7	2.5×10^{16}	1.4×10^9	1.15×10^9	1.9×10^{18}	1.1×10^{11}
5	3.08×10^7	5.2×10^{16}	2.9×10^9	2.44×10^9	4.0×10^{18}	2.3×10^{11}
6	5.21×10^7	8.4×10^{16}	4.9×10^9	4.30×10^9	7.2×10^{18}	4.0×10^{11}
7	7.89×10^7	1.3×10^{17}	7.4×10^9	6.72×10^9	1.1×10^{19}	6.3×10^{11}
8	1.11×10^8	1.8×10^{17}	1.0×10^{10}	9.68×10^9	1.6×10^{19}	9.1×10^{11}
9	1.47×10^8	2.4×10^{17}	1.4×10^{10}	1.31×10^{10}	2.2×10^{19}	1.2×10^{12}
10	1.87×10^8	3.1×10^{17}	1.8×10^{10}	1.71×10^{10}	2.8×10^{19}	1.6×10^{12}
15	4.28×10^8	7.2×10^{17}	4.0×10^{10}	4.19×10^{10}	6.8×10^{19}	3.9×10^{12}
20	7.09×10^8	1.2×10^{18}	6.6×10^{10}	7.25×10^{10}	1.2×10^{20}	6.5×10^{12}

* Assumptions made are: reacting volume = 1.64×10^8 cm^3,
vacuum chamber surface area = 1.75×10^6 cm^2
at r=1.5 m density n=3×10^{13} ions/cm^3
discharge duration

**"Flux" here refers to neutrons falling on 1 cm^2 area at 1.5 m without hindrance due to collimation; i.e. the whole plasma is viewed. Backscattering is ignored; actual (omnidirectional) flux will be 2 or 3 times greater than direct flux from plasma.

Table 1.2: Diagnostic Systems with Direction and Energy Resolution Capabilities

System	Best Resolution (%)	Efficiency per cm^2 of detector	Typical area (cm^2)	Fluence for good spectrum (n/cm^2)	Max.usable flux (n/cm^2 s)
		D-D neutrons			
^{3}He sandwich (5 atmos.)	2	10^{-6}	3	$3x10^8$	10^8
^{3}He ion chamber (side on)	2	$3x10^{-4}$	75	$4x10^4$	$4x10^5$
^{3}He prop.counter (end-on)	3	10^{-3}	20	$4x10^4$	$5x10^5$
CH_4 prop.counter	> 6 (unfolded)	10^{-4}	5	$2x10^8$	10^9
NE213 scintillator	8 (unfolded)	10^{-1}	5	$2x10^5$	10^6
Proton recoil[2] into detector (0.3mg foil)	2	$6x10^{-7}$	20	$8x10^7$	10^{11}
Neutron T. of F. (using proton recoil	2	$2x10^{-5}$	1-100	$5x10^5$-$5x10^7$	10^7
		D-T neutrons			
NE213 scintillator	4 (unfolded)	$3x10^{-2}$	5	10^6	10^6
Proton recoil telescope (7mg foil)	2	$4.0x10^{-6}$	20	$1.2x10^7$	10^{10}
Neutron T. of F. (using proton recoil)	2	$2x10^{-6}$	1-100	$5x10^6$-$5x10^8$	10^7

1.2 Previous Work

The fact that the fusion neutron spectrum could be used to study the ion energy distribution of a thermonuclear plasma has been known since the early days of fusion research. In 1967 Lehner and Pohl /1/ presented a paper in which most of the theory used today was detailed. Unfortunately, very little use has been made of this knowledge because of the difficulty in making high resolution measurements of fusion neutrons.

One of the earliest published measurements was that carried out at Oak Ridge where a system was developed for neutron flux measurements at the ORMAK Tokamak device /6/. A liquid scintillation counter (NE-213) with resolution of about 20% at 2.45 MeV (FWHM = 1 MeV) was not able to resolve the D-D fusion peak.

At Princeton /7/, an array of nine BF_3 long counters plus an U^{238} ionization chamber was capable of measuring the PLT neutron emission in the range 10^7 -> 10^{16} n/sec with 10 ms time resolution. Up to 10^{12} D-D neutrons per 0.1 s pulse have been obtained. Neutron intensities (up to $1x10^{13}$ n/s), the spatial origin of the neutron emission, and the neutron energy spectra was measured for PLT plasmas heated by deuterium neutral beams. Another measurements of the neutron spectra from the PLT Tokamak plasma were made using a ^3He ionization chamber, but were unable to resolve the D-D fusion peak for an ohmically heated plasma /8/.

A neutron spectrometer using a high pressure ^3He ionization chamber has been designed and used to measure the neutron spectrum from an ohmically heated deuterium plasma at Alcator C /9/. The resolution of the spectrometer at 2.45 MeV was determined to be 46 keV full width at half maximum (FWHM). The ratio for the number of counts in the 2.45 MeV peak to the total number

of detected neutron events was 1/67. A count rate as high as 44 counts per second has been achieved in the thermonuclear peak.

In Fontenay-aux-Roses /10/ a fast neutron spectrometer ($2x10^5$ events s^{-1}) was developed for the TFR Tokamak. A NE-213 scintillator coupled to a fast photomultiplier, a fast-γ-neutron discriminator and a fast data acquisition system were able to obtain a spectrum within 60 ms on the accelerator and within a single shot (500 ms) on the TFR.

Measurements of energy spectra of neutrons produced during high density ($n > 2x10^{14}$ cm^{-3}) deuterium discharges have been performed at Alcator C using a proton recoil (NE-213) spectrometer /11/. The results showed a well defined peak at 2.5 MeV which indicated that neutrons were of thermonuclear origin.

Neutron spectrometer (NE-213) was developed for diagnostic measurements on the Tandem Mirror Experiment (TMX) at the Lawrence Livermore National Laboratory (LLNL) /12/. Experimental determination of the performance parameters of the neutron diagnostic instrument reported indicated that simultaneous time-space-energy resolved measurements of plasma neutron emission were possible in a single instrument with respective resolutions: 50-100 ms, 10 cm at 6 m, and 160-200 keV at 2.5 MeV. The same spectrometer could be used for 14 MeV neutron measurements using different collimation.

A spherical ionization chamber was developed to measure the ion temperature (> 1 keV) in a D-D fusion plasma at the TEXTOR /13/. For this purpose an energy resolution of the detector of better than 3% was required.

A reference spectrometer was suggested for diagnostics of D-T plasmas in the JET Tokamak /14/. The technique is based on double interaction of the neutrons in two different scintillators and on time-of-flight measurement. For 14.1 MeV neutrons and for a flight path length of 2 m, energy resolution is about 2% and scales reciprocally to the flight path length. The spectrometer was capable of measuring ion temperatures above 2.5 keV under various plasma conditions and has an efficiency equal to $1x10^{-4}$.

1.3 Present Research

The variety of diagnostic systems which could be employed for neutron spectrum measurements at a Tokamak are listed in Table 1.2. Together with an indication of their expected resolution, efficiency, and required fluence for good spectrum /2/.

Two diagnostic systems were chosen for this research. The first was the NE-213 liquid scintillator with two different detector sizes, one was 2"x2" and the other 2"x5". The second diagnostic system was the 3He semiconductor sandwich neutron spectrometer.

A NE-213 proton-recoil spectrometry system has been assembled and tested for both D-D and D-T measurements. The detector efficiency and response functions (Response Matrix) were calculated with CECIl Monte Carlo code /29/. Several improvements have been made for the CECIL code to agree with the measurements of this spectrometer. Neutron energy spectra were obtained by unfolding pulse height spectra measured with the NE-213 scintillators. The FERDOR unfolding procedure /31/, after several improvements, have been used in unfolding the present measurements.

A neutron spectrometer using a 3He semiconductor sandwich detector was used to measure the neutron spectrum for D-D neutrons. The efficiency was calculated for this spectrometer, while the neutron energy spectra were measured to determine the resolution.

2. EXPERIMENTAL PROCEDURE FOR THE NE-213 SPECTROMETER

2.1 Neutron Detector

NE-213 proton recoil spectrometers have been used extensively as one of the various techniques developed to determine complex fast neutron spectra in association with gamma-ray fields. This is based on two important advantages: firstly they represent a good compromise of efficiency and resolution and secondly the scintillation process in NE-213 permits discrimination of gamma-rays based on the pulse rise time. The NE-213 scintillator detects fast neutrons through the process of charged particle induced reactions, primarily proton recoil, while γ-rays are detected primarily through the process of compton electron recoil. Because of the indirect detection process of neutrons, NE-213 pulse height data must be unfolded to obtain the neutron energy spectra.

Two neutron detectors were used in the measurements. Cylindrical organic liquid scintillators of dimensions 2"x2" and 2"x5" filled with NE-213. The density of NE-213 is 0.867 gm/cm^3 and the composition is $CH_{1.21}$ as given in the manufacturer's specifications. The scintillators were directly coupled to RCA-8575 photomultiplier (directly in the sense that there is no light guide in the system). The ORTEC 265 photomultiplier base provides two outputs: the negative anode signal for timing applications and the linear signal from the ninth dynode.

2.2 Electronics

A block diagram of the electronics used for data aquisition is shown in Fig. 2.1. The timing signal taken from the PM tube is used to define the beginning of each pulse. The pulse height

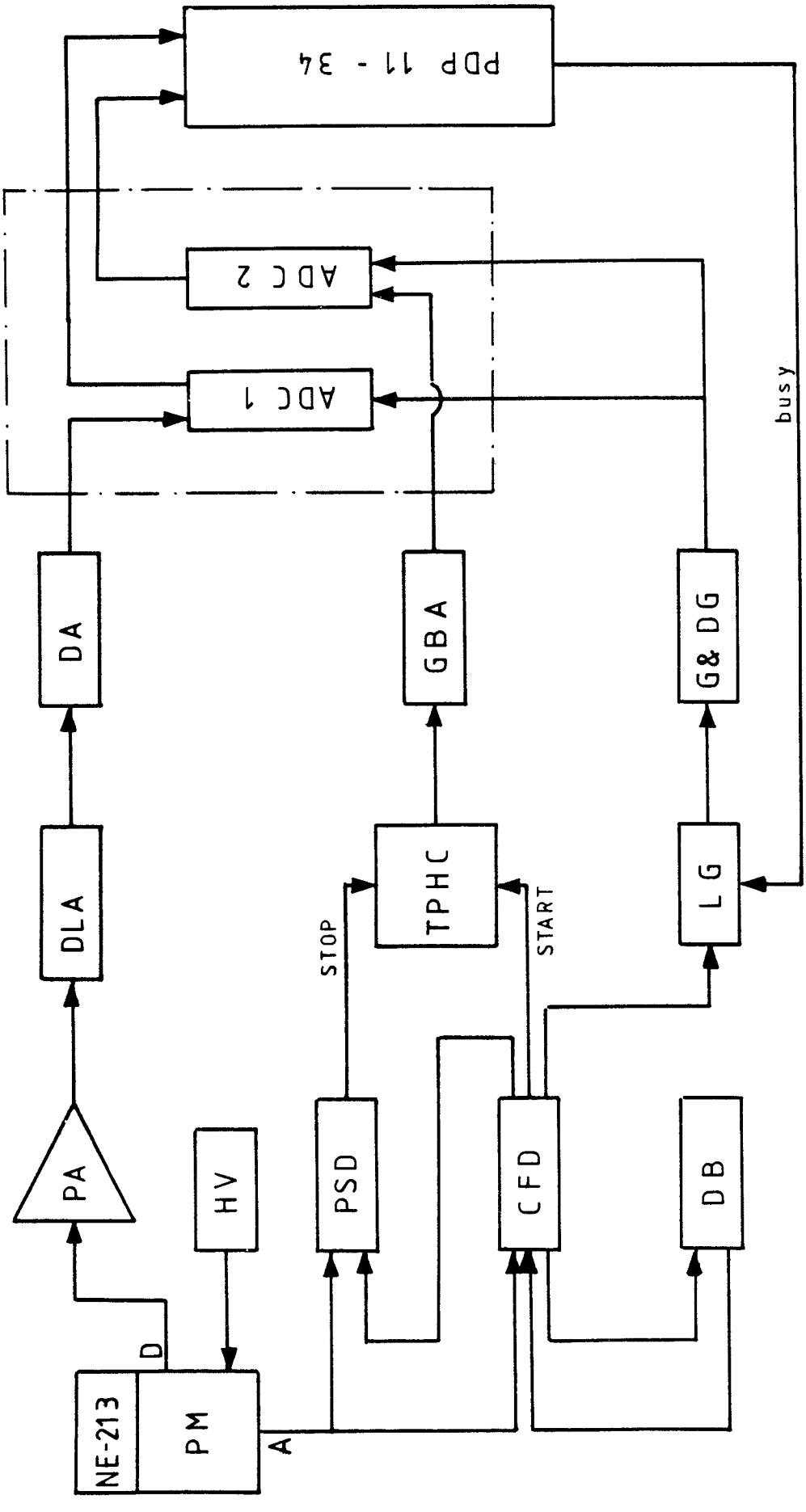

Fig. 2.1:

Block diagram of electronics for NE-213 spectrometer

of the energy signal taken from the PM defines the light output for an event. The pulse shape of the energy signal is used to determine whether the pulse is due to a neutron event or a gamma ray event.

The preamplifier (PA) (ORTEC 113), delay line amplifier (DLA) (ORTEC 460) and delay amplifier (CANBERRA 1457) shape and amplify the energy signal. The pulse shape discriminator (PSD) (CANBERRA 2160A), quad constant fraction discriminator (CFD) (ORTEC 934), delay box (DB) (ORTEC DB463), time to pulse height converter and single channel analyser (TPHC) (ORTEC467) and gated biased amplifier (GBA) (ORTEC 444) compromise the pulse shape discrimination circuitry. The constant fraction discriminator signal is routed to a linear gate (LG) (ORTEC 426) then to gate and delay generator (G&DG) (ORTEC 416A) and is used to gate the two ADC's for neutron events.

2.3 Pulse Shape Discrimination

A neutron gamma discrimination method by using a pulse shape discriminator (PSD) (CANBERRA 2160) is a simple and convenient method to suppress gamma rays in a neutron detection system since only an anode output of a photomultiplier is required by the PSD /15,16/. In our neutron spectrometer system anode output pulses of the photomultiplier is fed directly into the PSD. When only the neutron event information is required, output pulses of the PSD in n mode can be used as neutron event pulses after adjusting the strobe delay. In practice, however, the pulse shape information of each event is required for the later analysis, since the quality of the n-γ-discrimination depends on the pulse height of the detector output. In this case, output pulses of the PSD in n+γ mode are used as stop pulses of time to pulse height converter (TPHC). The detection system becomes complicated because output pulses of the constant frac-

tion discriminator (CFD) are used as a start pulses of TPHC, and thus the CFD output must be delayed in such a way that output pulses of the PSD and the CFD are accepted within a time interval of the TPHC. If the strobe signal is placed between the crossing points of gamma and neutron pulses only pulses caused by neutrons will produce an output pulse. In our setup the strobe signal is triggered by the output pulse of the CFD, which is delayed and stretched.

The constant fraction timing technique is used in this discriminator to provide excellent timing when used with PM tubes. This instrument accepts negative input pulses and generates NIM-standard fast negative logic pulses for each input pulse that exceeds the adjusted threshold level. Each input signal is split so that a portion of the signal is delayed and substracted from a fraction of the undelayed signal. The resulting bipolar constant-fraction signal has a base line cross over that is virtually independent of the input signal amplitude. The zero crossing point is detected and used to provide precisely timed logic pulses.

The TPHC measures the time-interval between the leading edge of the logic pulses furnished to its start and stop inputs and generates an analog output pulse that is proportional to the measured time through the TPHC output. Each TPHC output pulse has a peak amplitude that is proportional to the ratio of measured time interval to the selected full-scale interval. Start-to-stop time conversion is accomplished only after a valid start has been identified and after a stop pulse has arrived within the selected time range.

The output signal of the TPHC identifies the fall time of the original hight pulses and hence the particle type. The output of the DA is used as the pulse height identifier signal. This and the TPHC output (after amplification in GBA) are fed to two

separate analogue to digital converters (ADC) which are gated with the signal from CFD. These data are accumulated through the PDP11 computer.

The pulse shape spectra for the NE-213 spectrometer with this pulse shape discrimination system are shown in Fig. 2.2 through Fig. 2.6.

What is shown in Figs. 2.2 to 2.4 is a simple relation between the channel number and the counts per channel for different neutron sources. But Figs. 2.5 and 2.6 are two dimensional plots of the pulse height against time which are used to discriminate neutrons from gammas with suitable "separate function".

Another pulse shape discrimination is used in these measurements using the electronic system shown in Fig. 2.7. In this system the fast negative anode pulse is routed to the CFD which generates as its output a NIM standard fast logic signal. The output of the dual gate generator (DGG) (Le Croy) will act as a time marker "START" signal for the timing analyser (TA) (ORTEC 455). The anode signal is saturated, thus its pulse height is not linearly dependent on the original light intensity from the scintillator. A second signal is therefore extracted from an earlier dynode stage (dynode 9) where the pulse height is still linear with light intensity (except for very large light pulses produced by protons of energy greater than 12 MeV, where some saturation is observed). This signal, which carries both timing and pulse height information from the scintillator decay mode, is routed to DLA. The central zero crossing of the bipolar output from the DLA depends on the decay time of the input pulse. The zero crossing detector is a timing single channel analyser (Timing SCA) (ORTEC 455) operating in the bipolar mode. The zero crossing point of the input pulse triggers a NIM standard fast timing signal from this unit. This

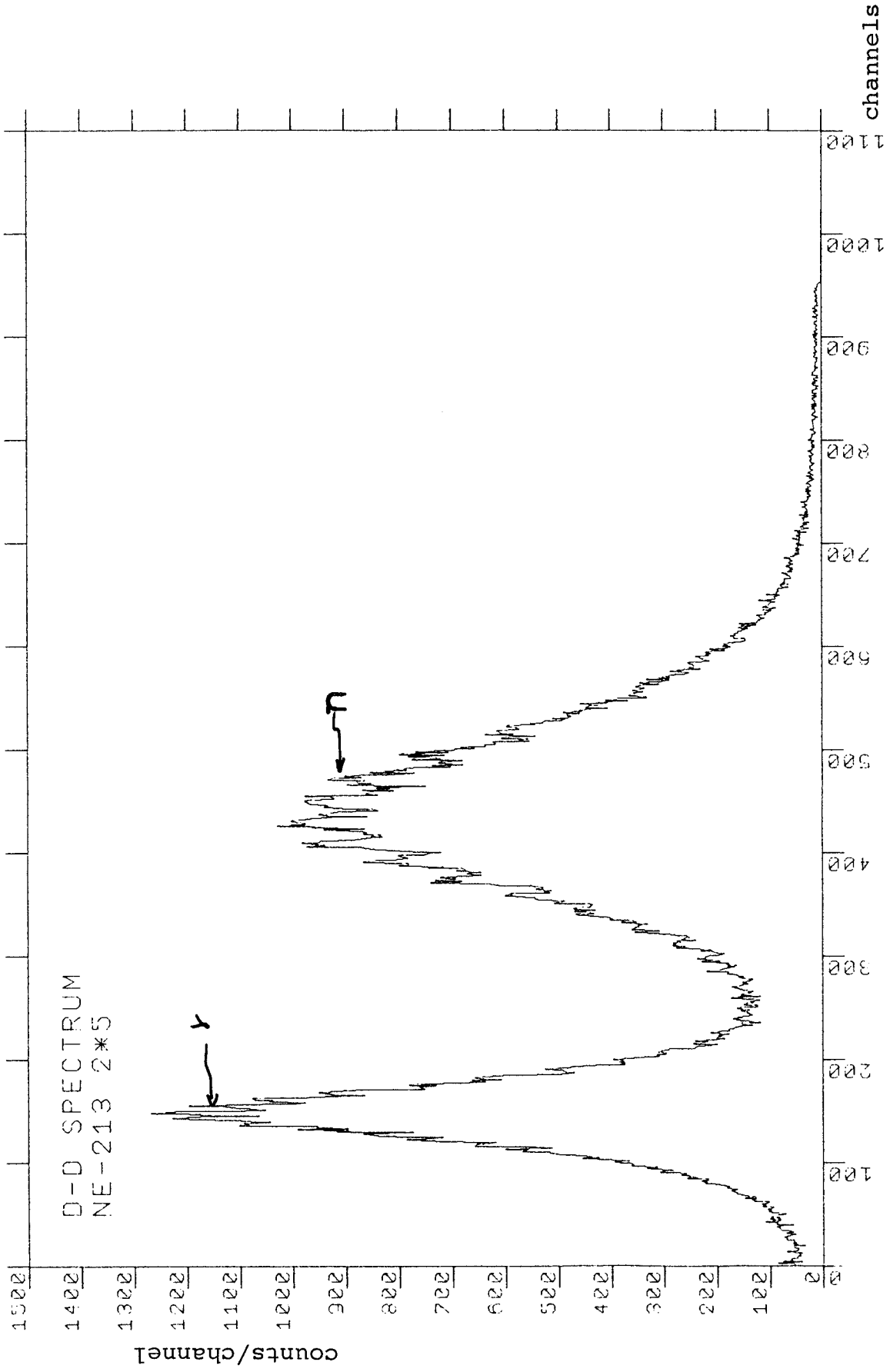

Fig. 2.2: Pulse shape spectrum for D-D neutrons with 2"x5" NE-213 detector

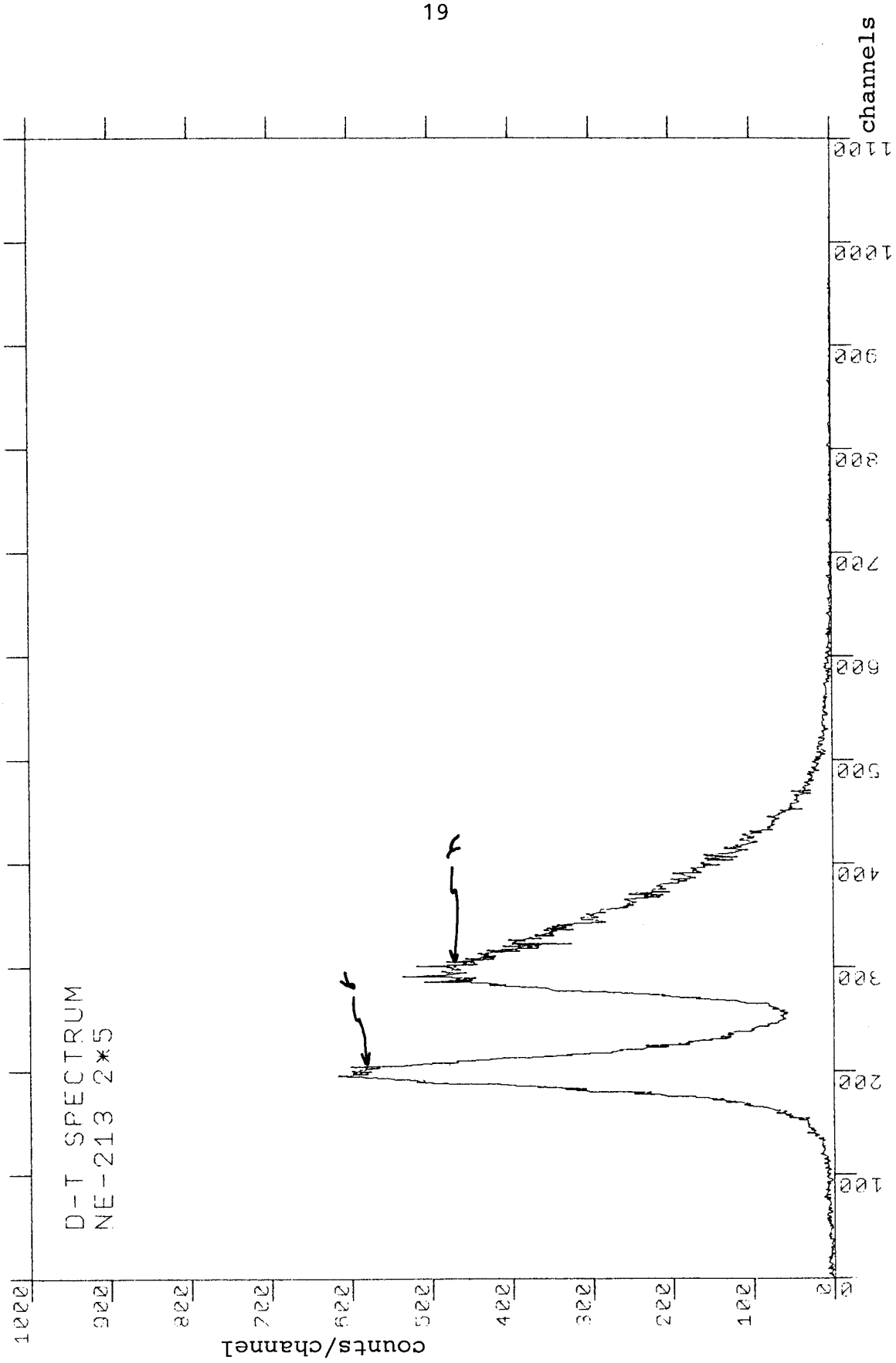

Fig. 2.3: Pulse shape spectrum for D-T neutrons with 2"x5" NE-213 detector (without shielding)

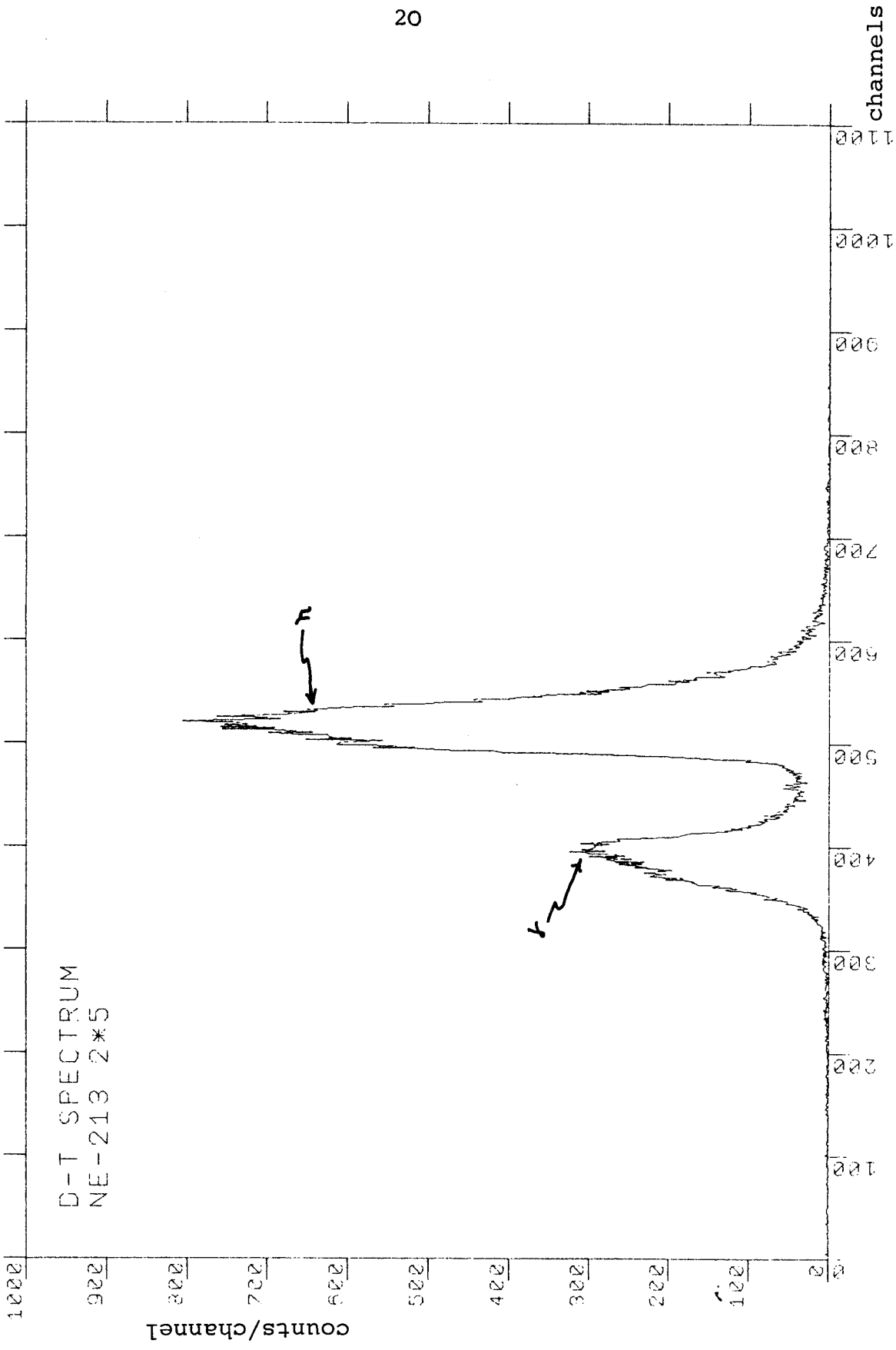

Fig. 2.4: Pulse shape spectrum for D-T neutrons with 2"x5" NE-213 detector

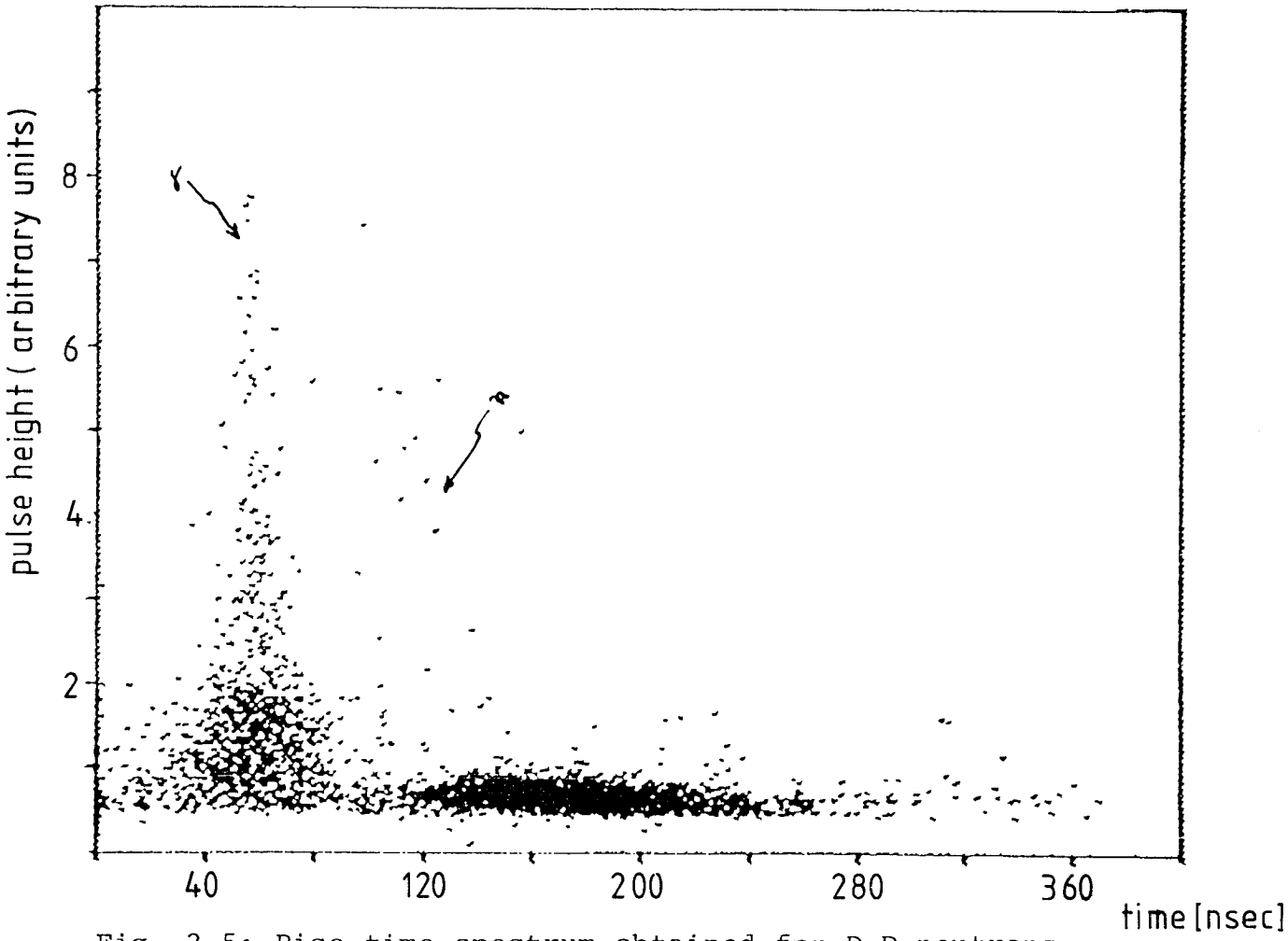

Fig. 2.5: Rise time spectrum obtained for D-D neutrons with 2"x5" NE-213 detector

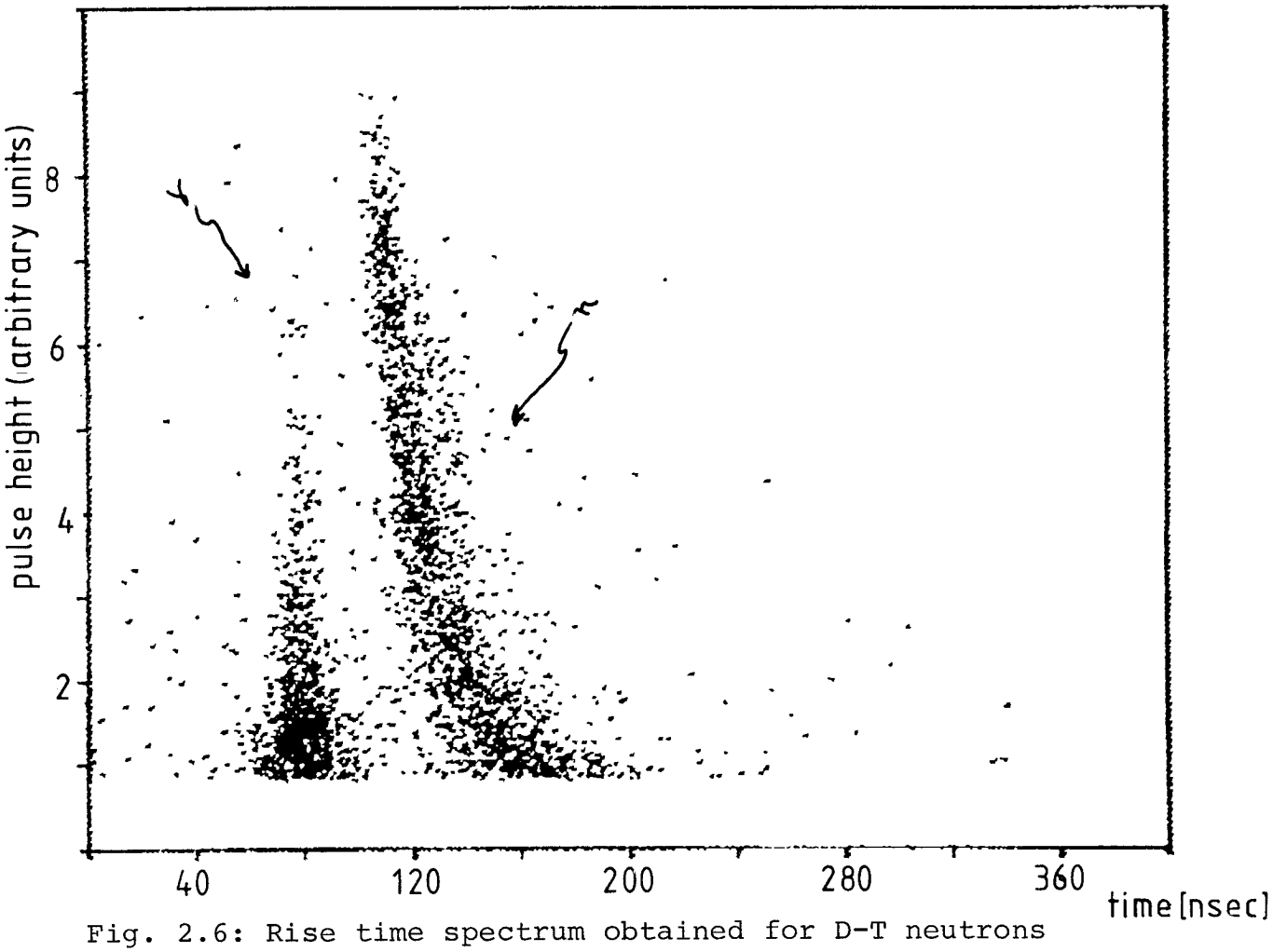

Fig. 2.6: Rise time spectrum obtained for D-T neutrons with 2"x5" NE-213 detector

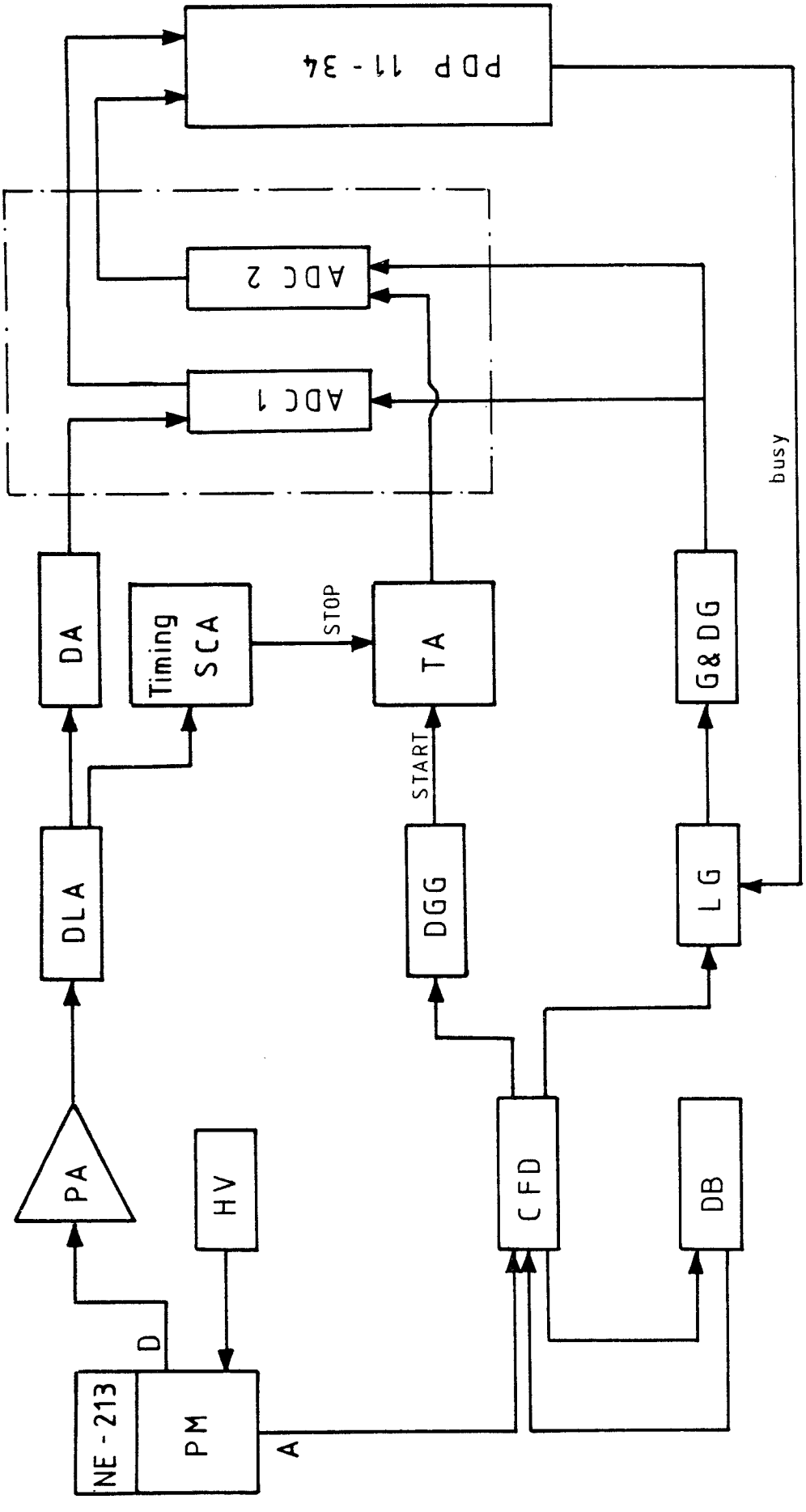

Fig. 2.7:
The second electronic circuit of the NE-213 spectrometer

signal is used to provide a "STOP" signal for the TA. The pulse height of the output of this unit depends on the time between the START and STOP signals. This output signal corresponds to the zero crossing pulses and thus identifies the fall time of the original light pulses and hence the particle type. The unipolar output of the DA is used as the pulse height identifier signal. This and the TA output are fed to two separate analogue to digital converters (ADC) which are gated with the signal from CFD. These data are accumulated through the PDP11 computer.

The pulse shape spectra for the NE-213 spectrometer with this pulse shape discriminator system are shown in Fig. 2.8 through Fig. 2.12.

2.4 Calibration Procedure

The scintillation efficiency of NE-213, that is the fraction of ionization energy converted to light, depends on the type of charged particle producing the ionization. Electrons have a reasonably uniform, low specific ionization except at the very end of their track. For electron energies above 100 keV, the relation of light pulse height to electron energy is considered linear and maybe expressed as $P=c(E-b)$, where P is the relative pulse height, E the electron energy, b the energy intercept and c the slope, which is characteristic of the system used /17/. Therefore, the different species produced along their track are usually at low concentration and the probability of interactions between them is low. On the other hand, heavier charged particles, such as alpha particles, protons, etc. have a non-uniform high specific ionization, and at the very end of their range there is very high ionization. The concentration of various species along their track is much higher, compared to the electron track, and the probability of reactions is greater. The excited molecules that undergo certain

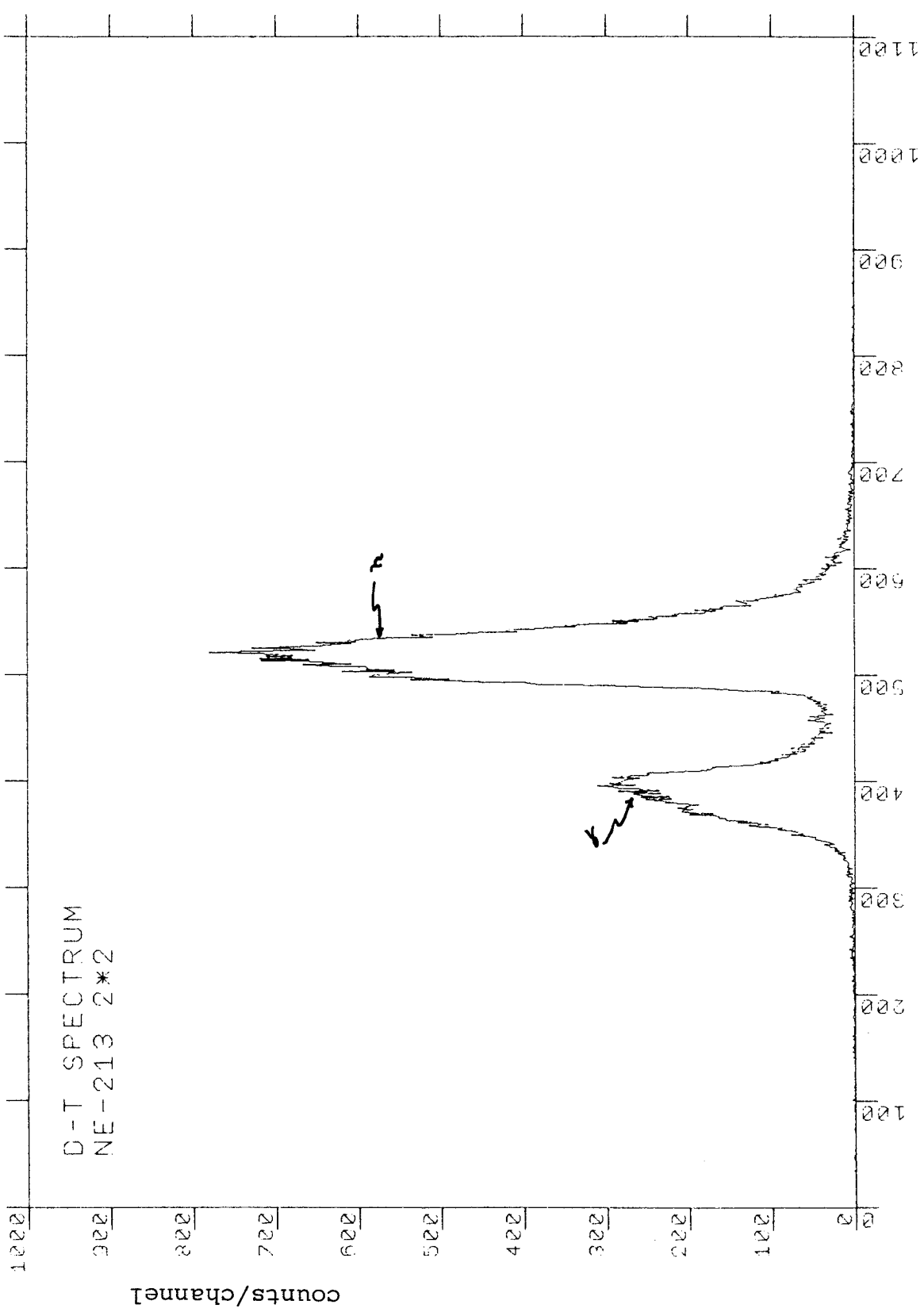

Fig. 2.8: Pulse shape spectrum for D-T neutrons with 2"x2" NE-213 detector

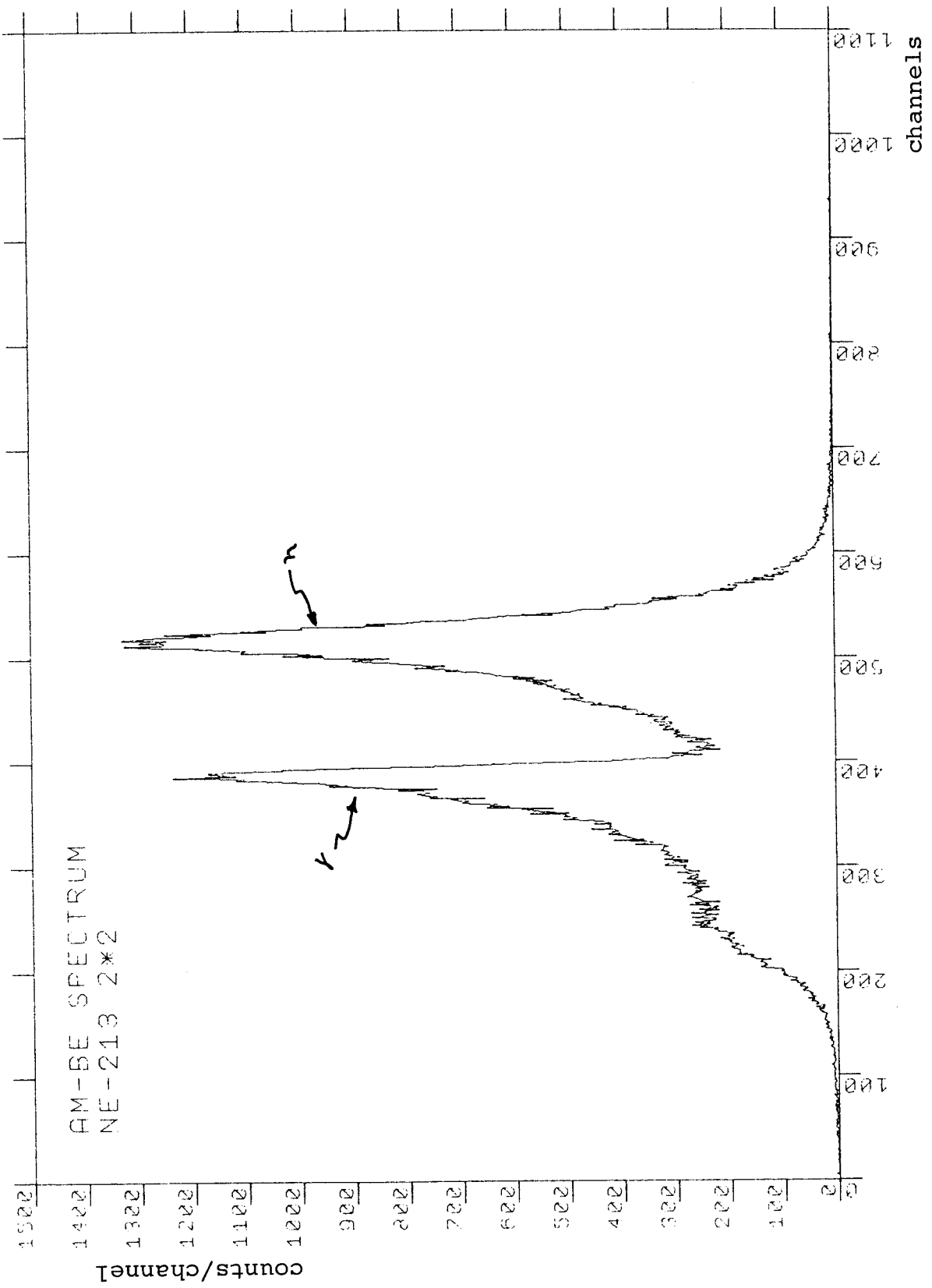

Fig. 2.9: Pulse shape spectrum for Am-Be neutron source with 2"x2" NE-213 detector

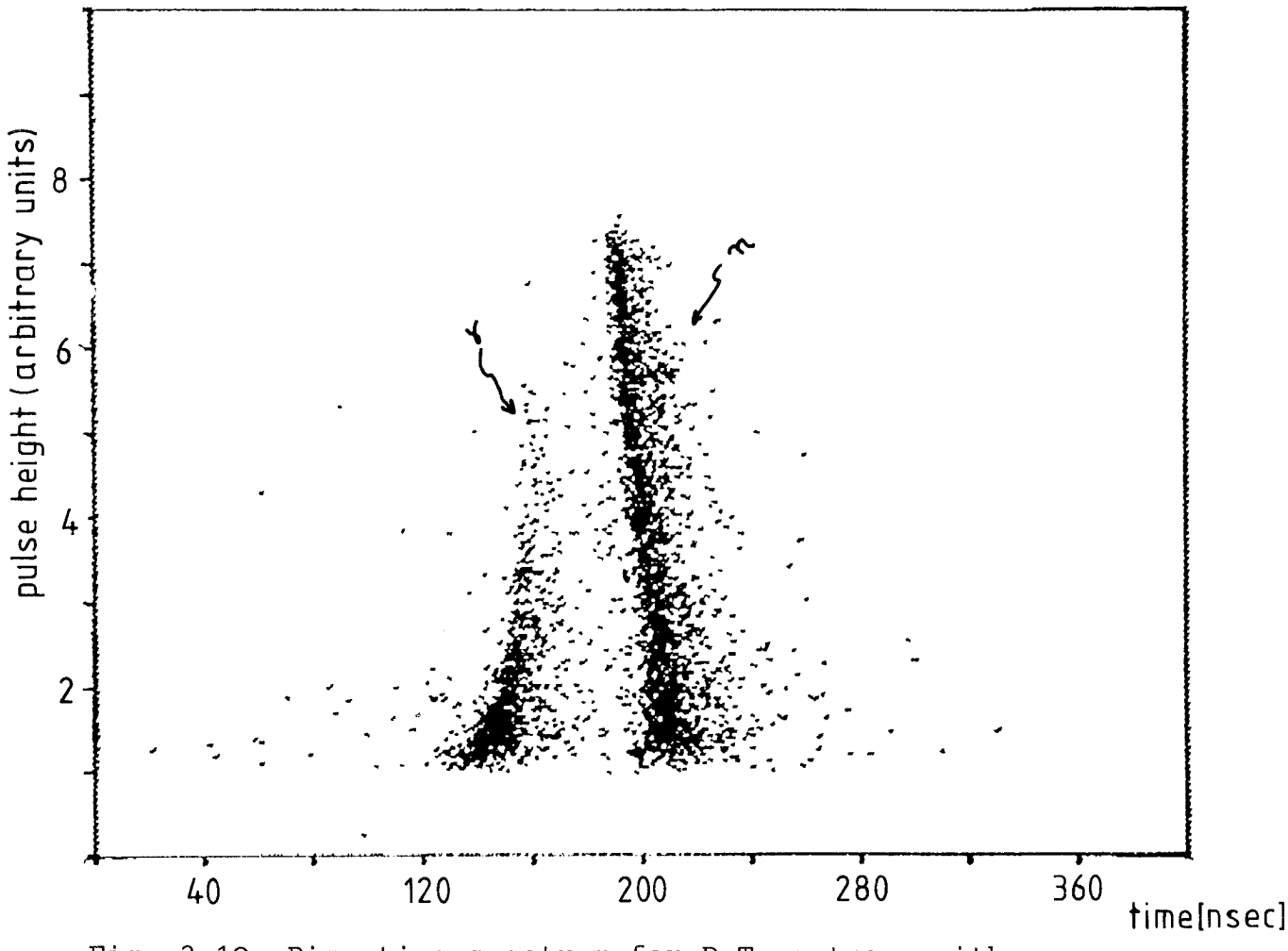

Fig. 2.10: Rise time spectrum for D-T neutrons with 2"x2" NE-213 detector

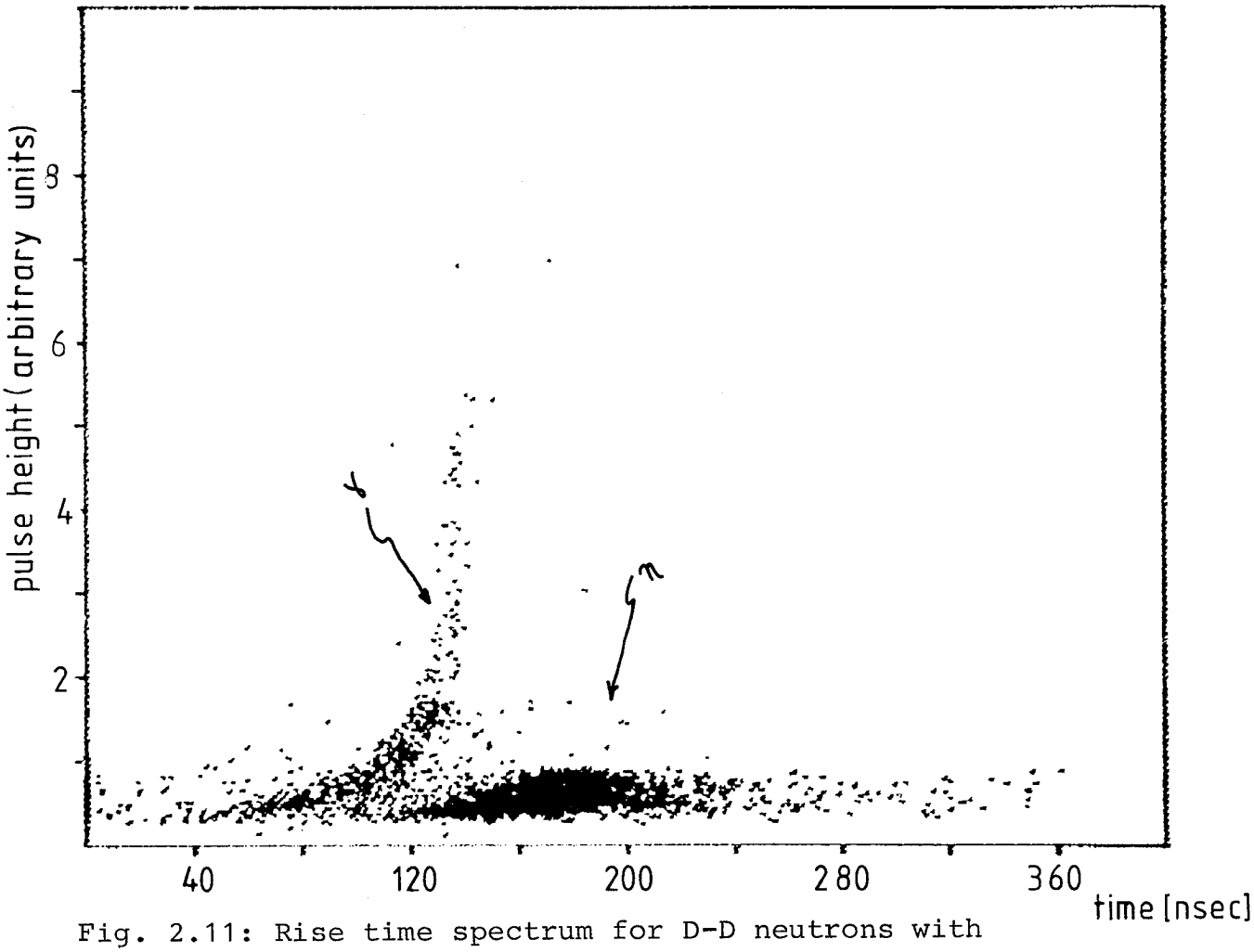

Fig. 2.11: Rise time spectrum for D-D neutrons with 2"x2" NE-213 detector

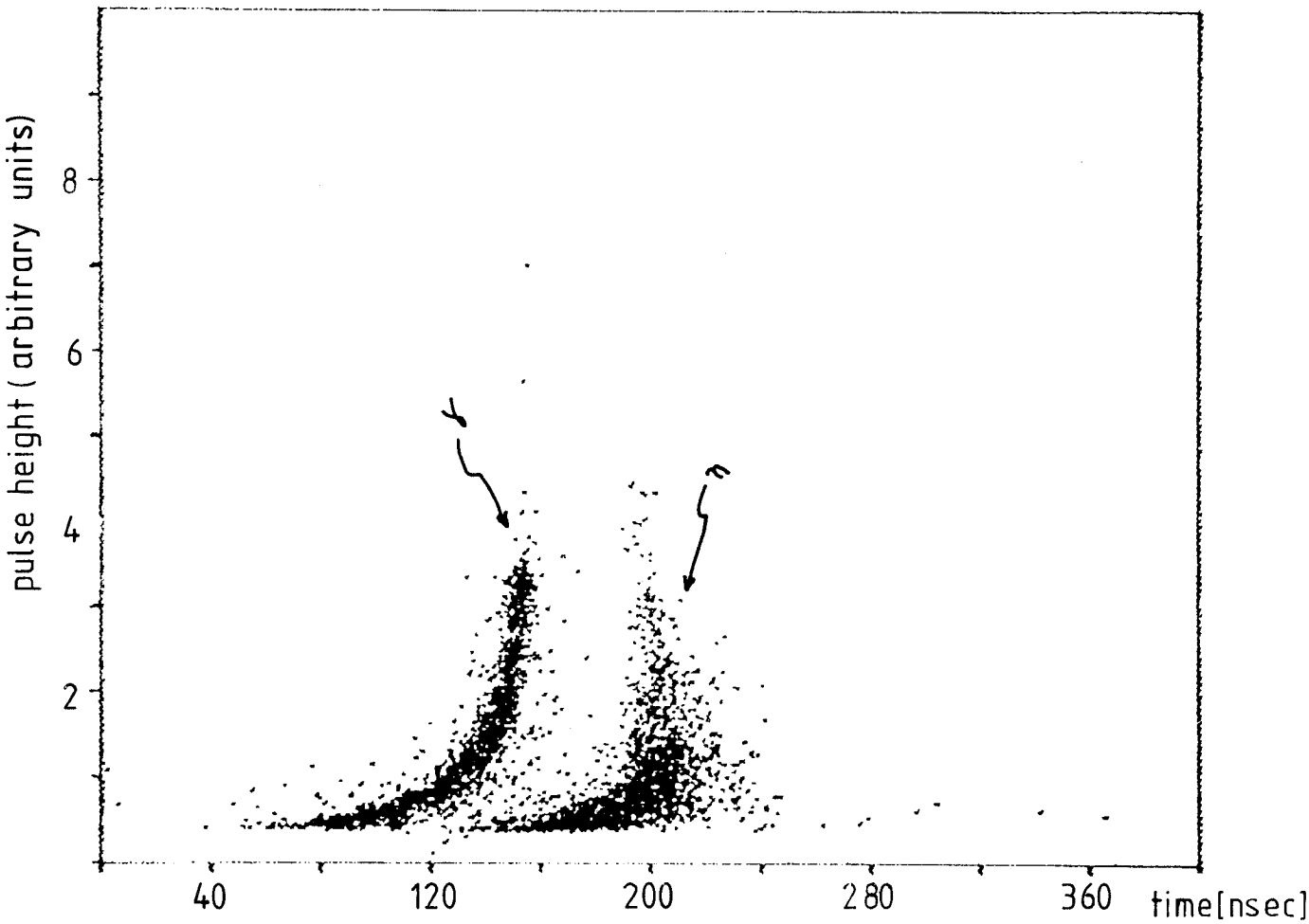

Fig. 2.12: Rise time spectrum for Am-Be neutron source with 2"x2" NE-213 detector

type of reactions will not be able to lead to the emission of photons. It is therefore, necessary to calibrate the amplitude pulse of the spectrometer in order to be able to relate the structure of the response functions to the nuclear events in the cell.

Because of the low atomic number of organic scintillators, there is a low probability of photoelectric absorption, therefore, light pulses arising from incident gamma rays are produced by the recoil electrons in compton scattering.

The maximum energy in MeV of the compton recoil electron is given by

$$E_e = \frac{2\,E^2_\gamma}{0.511+2E_\gamma}$$

where E_γ is the incident photon energy in MeV.

In the case of a detector with perfect resolution the edge of the compton distribution is vertical and the exact position of the compton edge in the pulse height spectrum could be obtained and assigned to the electron energy E_e. But the finite resolution of the system, the relatively greater range of electrons in NE-213 (e.g. 1 MeV electron has an effective range of 5 mm in NE-213, NUCLEAR ENTERPRISES 1974) and the photomultiplier statistics complicate the location of the compton edge on the measured pulse height distribution. It is decided to use the compton edge as a pulse height marker, where the half height of the compton distribution is 4(+/-1)% above the compton edge /18,19/.

Gamma-ray sources of ^{22}Na, ^{137}Cs, ^{60}Co, ^{88}Y and ^{228}Th (^{208}Tl) are used to calibrate the spectrometer system. Pulse height spectra for these sources are illustrated in Fig. 2.13 through

Fig. 2.17. The electron response of the NE-213 scintillator is shown in Fig. 2.18. The electronic systems were adjusted so that these calibration curves are used for both 2"x2" and 2"x5" detectors.

2.5 Pulse Height Measurements

The measurement of a neutron energy spectrum required several pulse height spectrum measurements. Unfortunately, the zero intercept was found to drift with time. It was therefore necessary to not only adjust the zero intercept setting at the beginning of a spectrum measurement, but also to monitor the zero intercept setting during the course of measurement to insure that unacceptably large zero-intercept drifts did not occur.

The pulse height distribution for both Am, Be nd ^{252}Cf neutron sources were measured using the NE-213 spectrometry system. As mentioned earlier two neutron producing reactions were to be considered, namely D-D and D-T reactions. The pulse height measurements for monoenergetic neutron sources were made with a particle accelerator (SAMES T400). The accelerator has been specially designed for intense neutron production by D-D or D-T reactions. This accelerator is capable of accelerating deuterons to 400 keV with a beam current of 2 mA. Under these conditions over $0.5x10^{12}$ neutrons are produced per second with D-T reaction and 10^{10} neutrons per second with D-D reaction. A cross sectional view of the spectrometer is shown in Fig. 2.19 consists of the NE-213 detector mounted in a shielding enclosure designed for the accelerator measurements.

The measured pulse height distributions for the different neutron sources with both detectors are shown in Fig. 2.20 through 2.25.

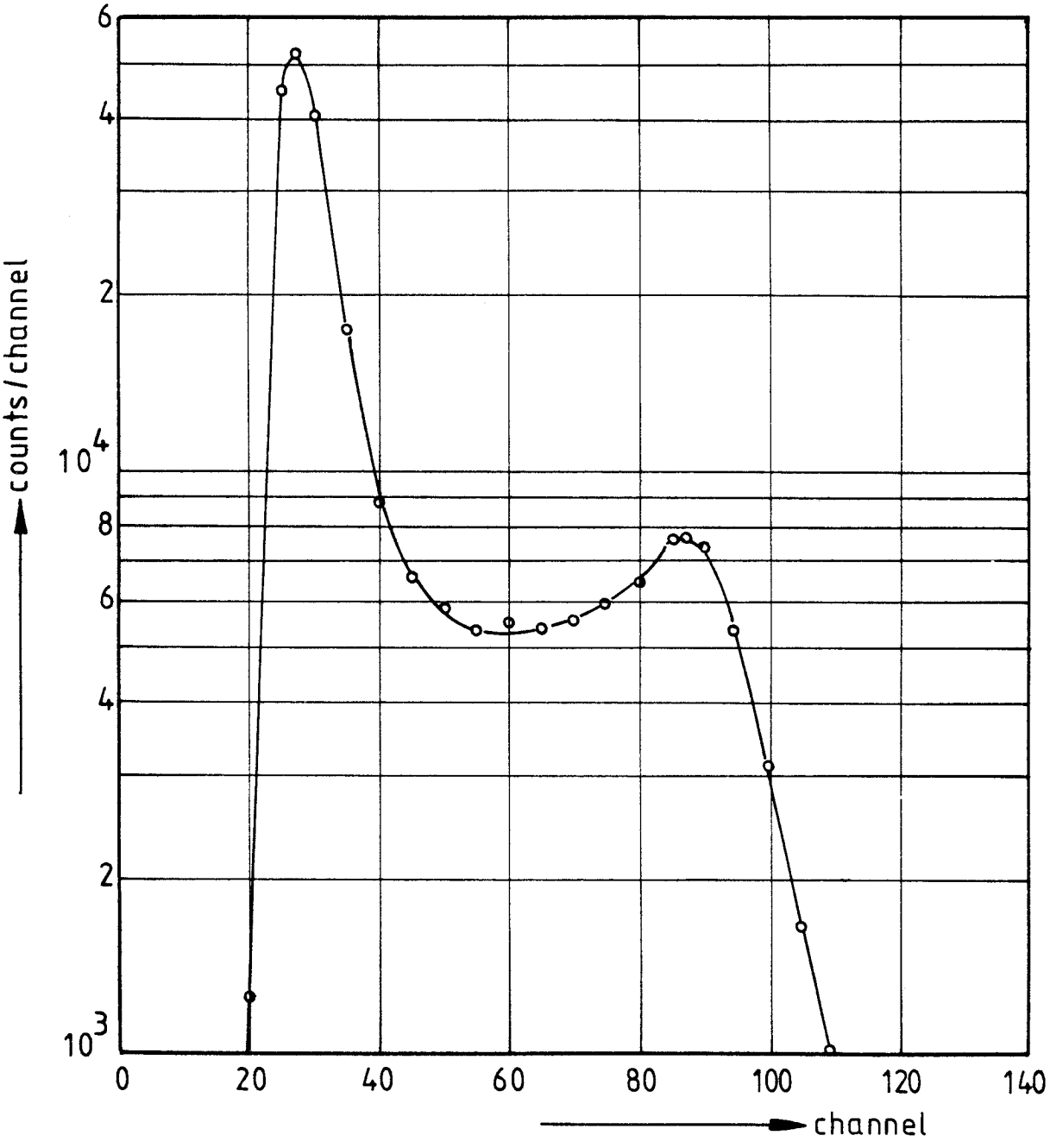

Fig. 2.13: Pulse height distribution for calibration use using ^{22}Na

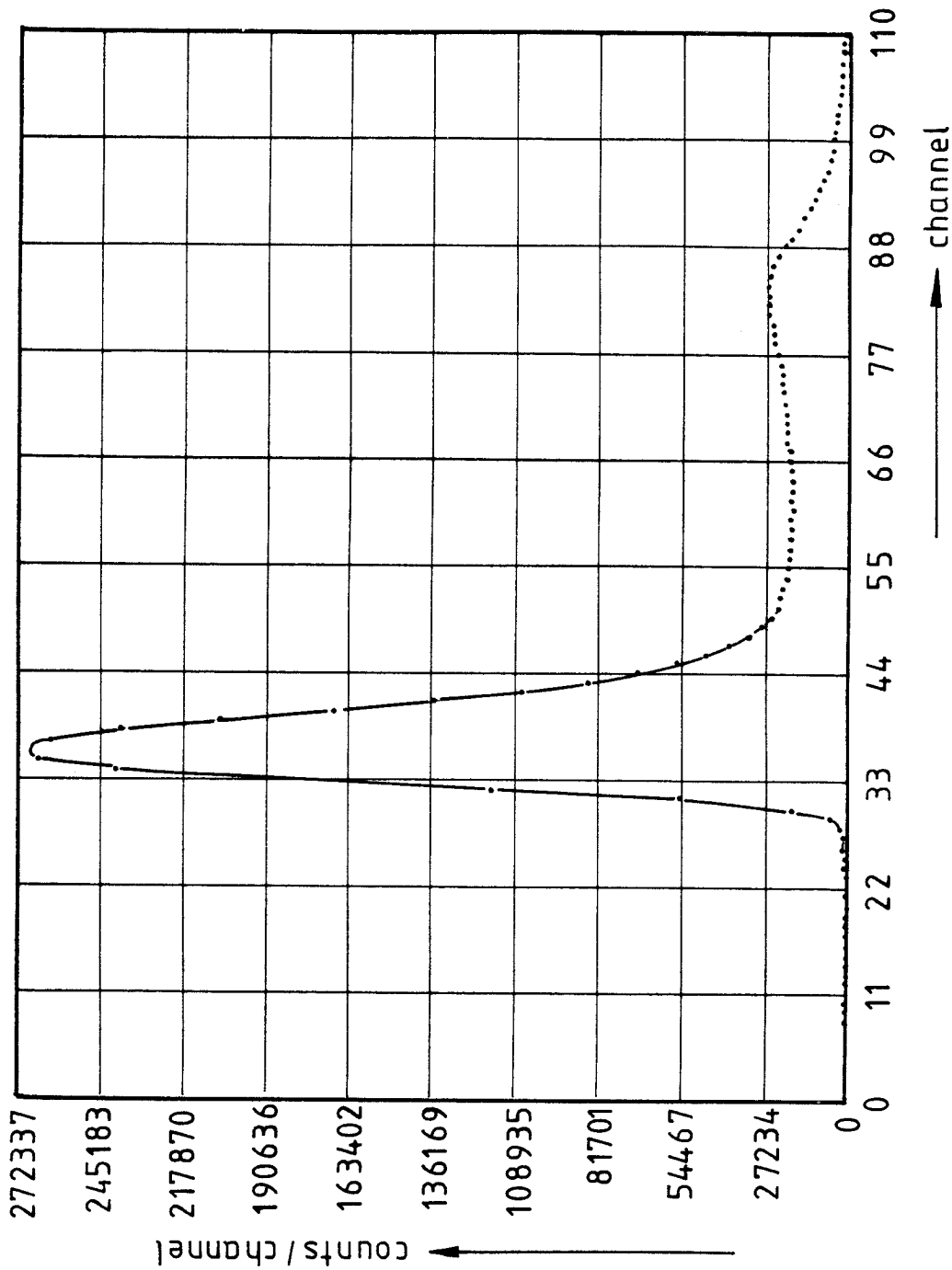

Fig. 2.14: Pulse height distribution of ^{137}Cs showing Compton distribution and maximum Compton recoil

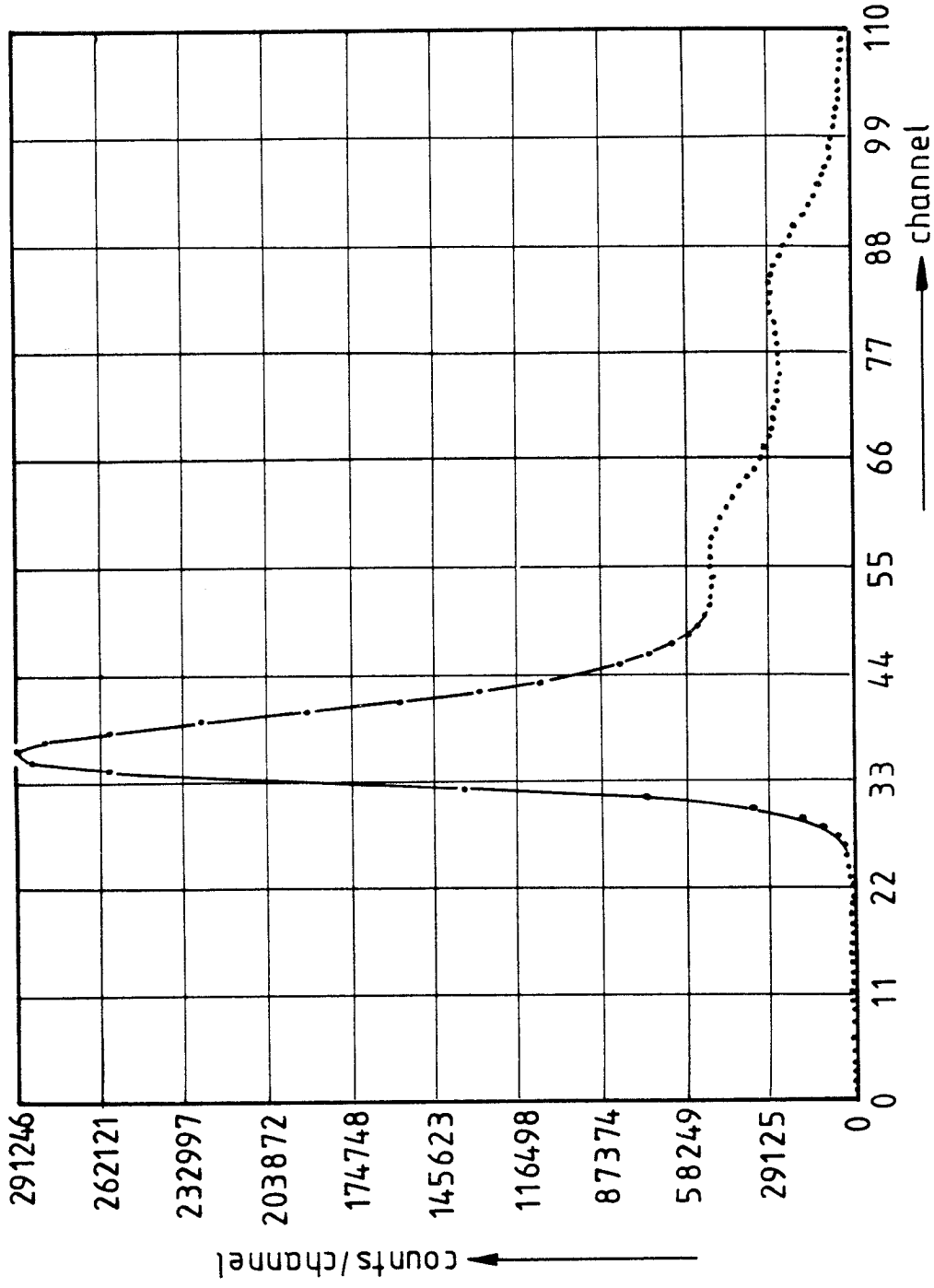

Fig. 2.15: Pulse height distribution for ^{60}Co

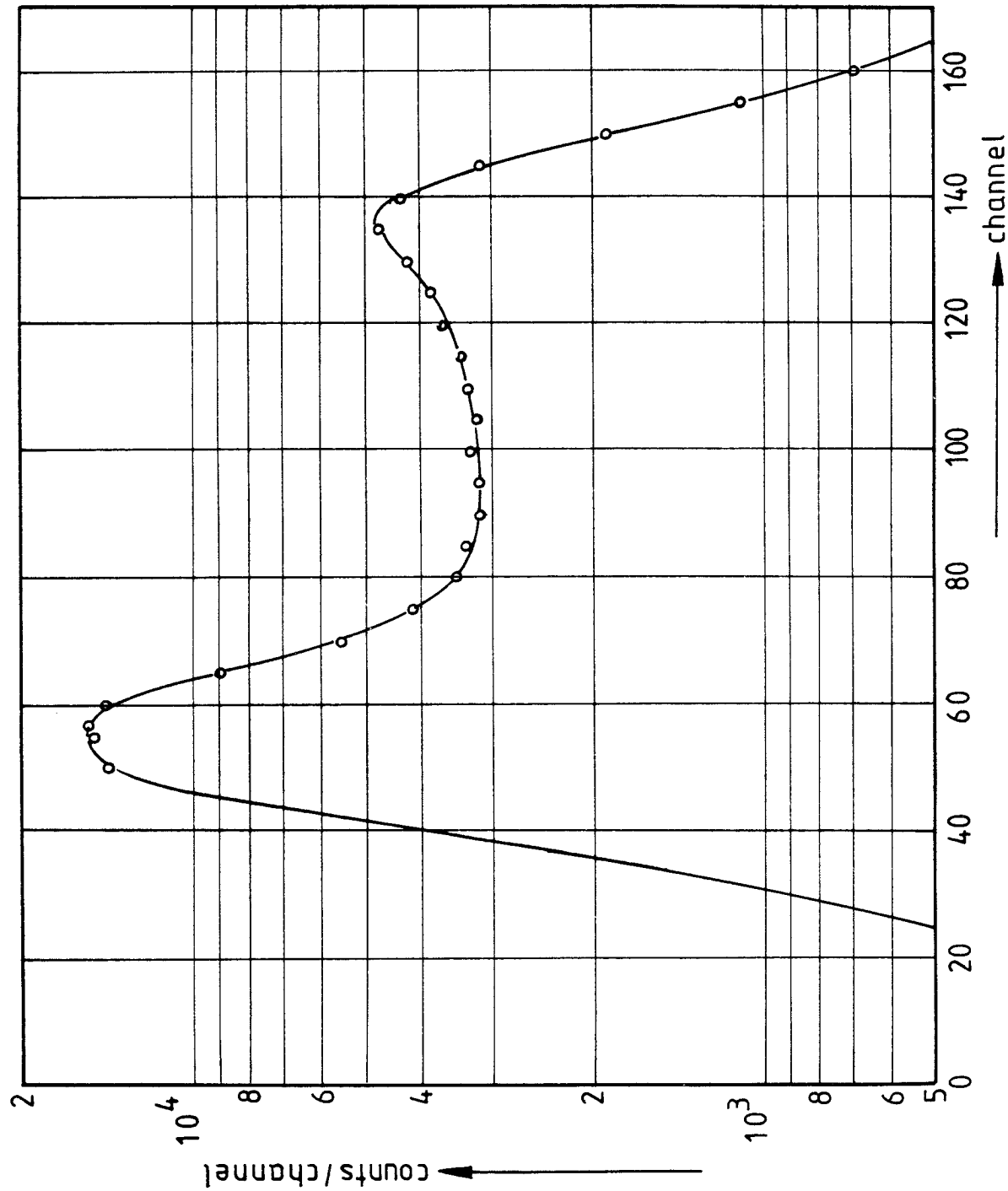

Fig. 2.16: Pulse height distribution for ^{88}Y

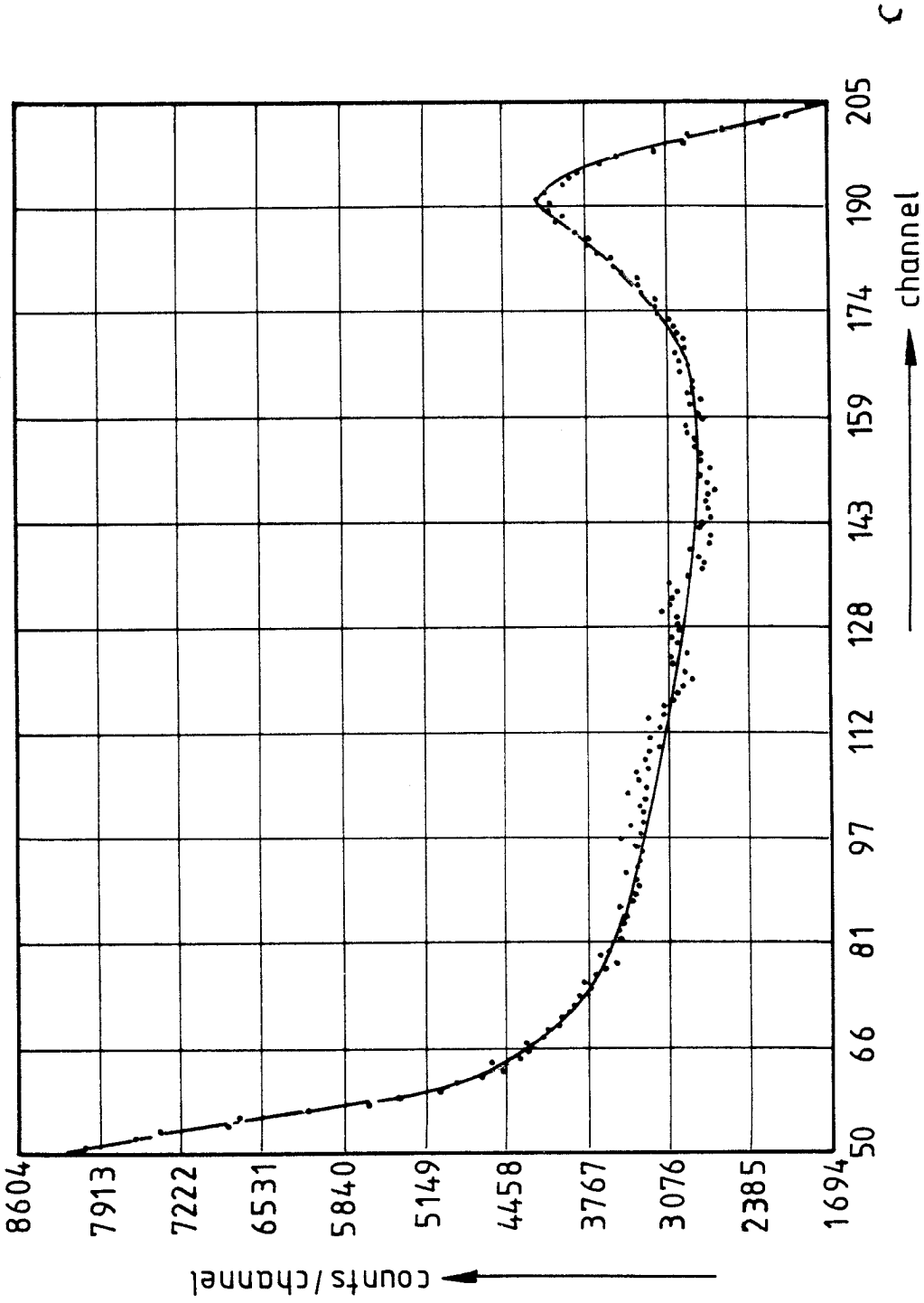

Fig. 2.17: Pulse height distribution of ^{228}Th

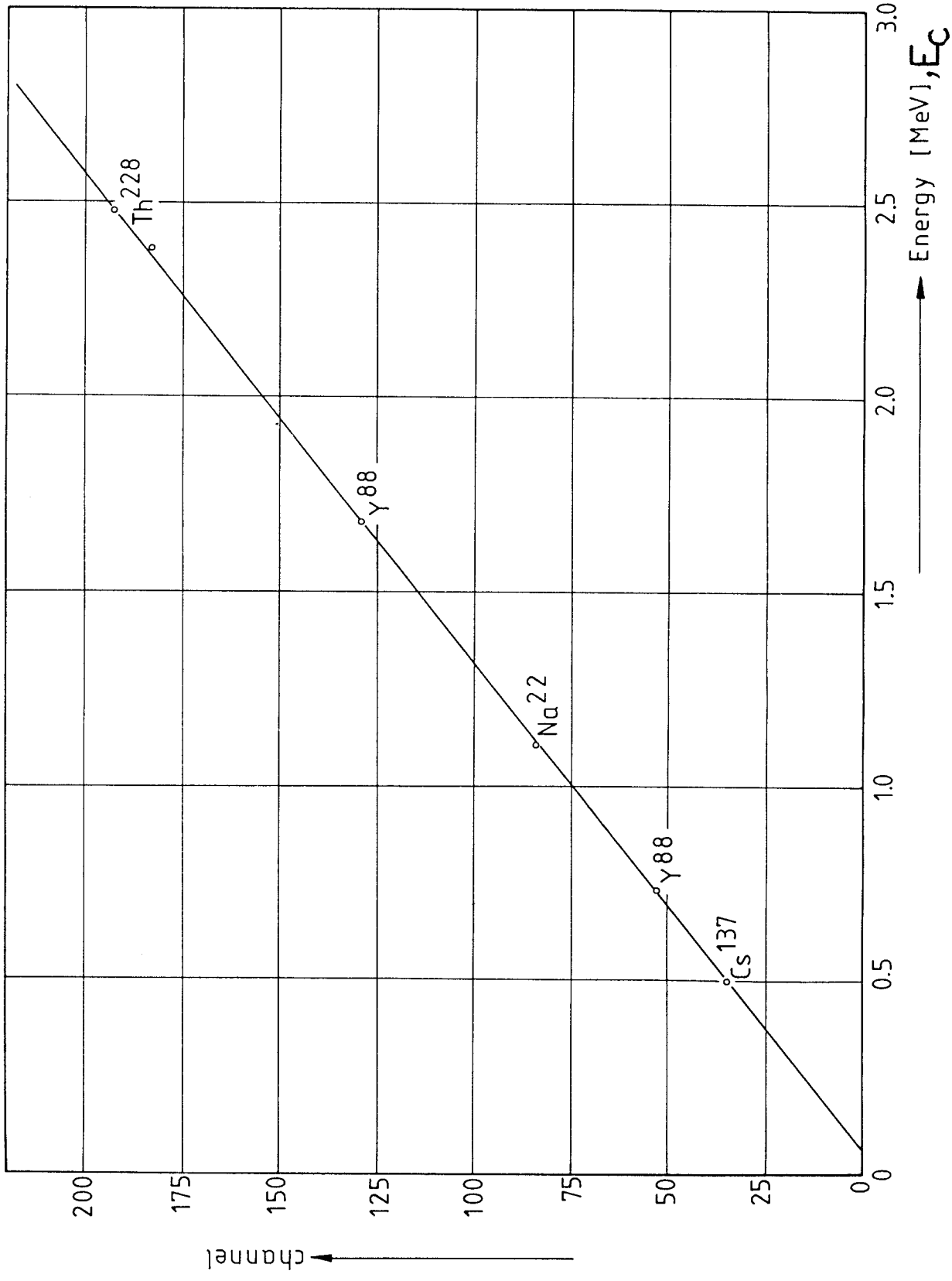

Fig. 2.18: Electron response of both 2"x2" and 2"x5" NE-213 scintillators

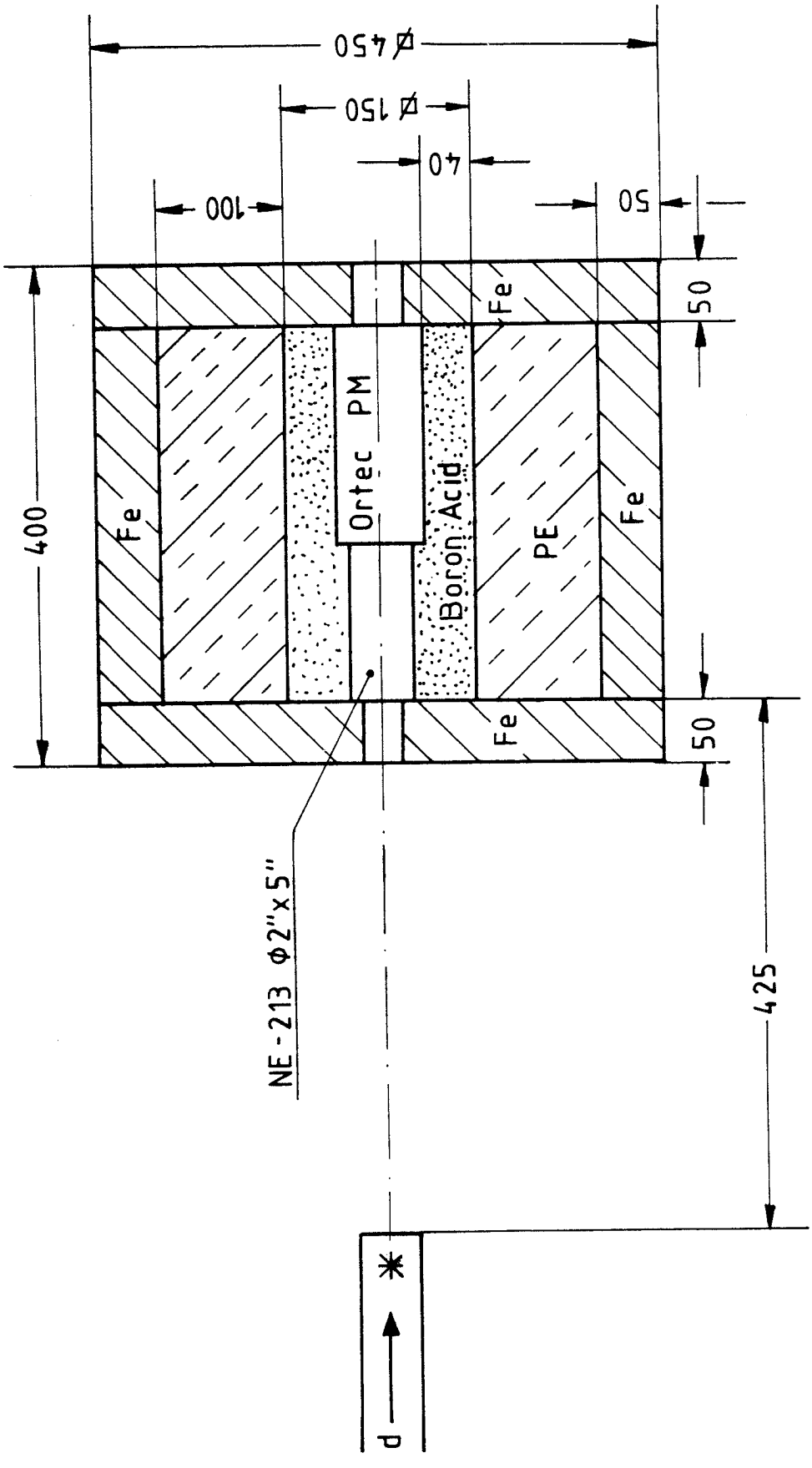

Fig. 2.19: Cross sectional view of the spectrometer

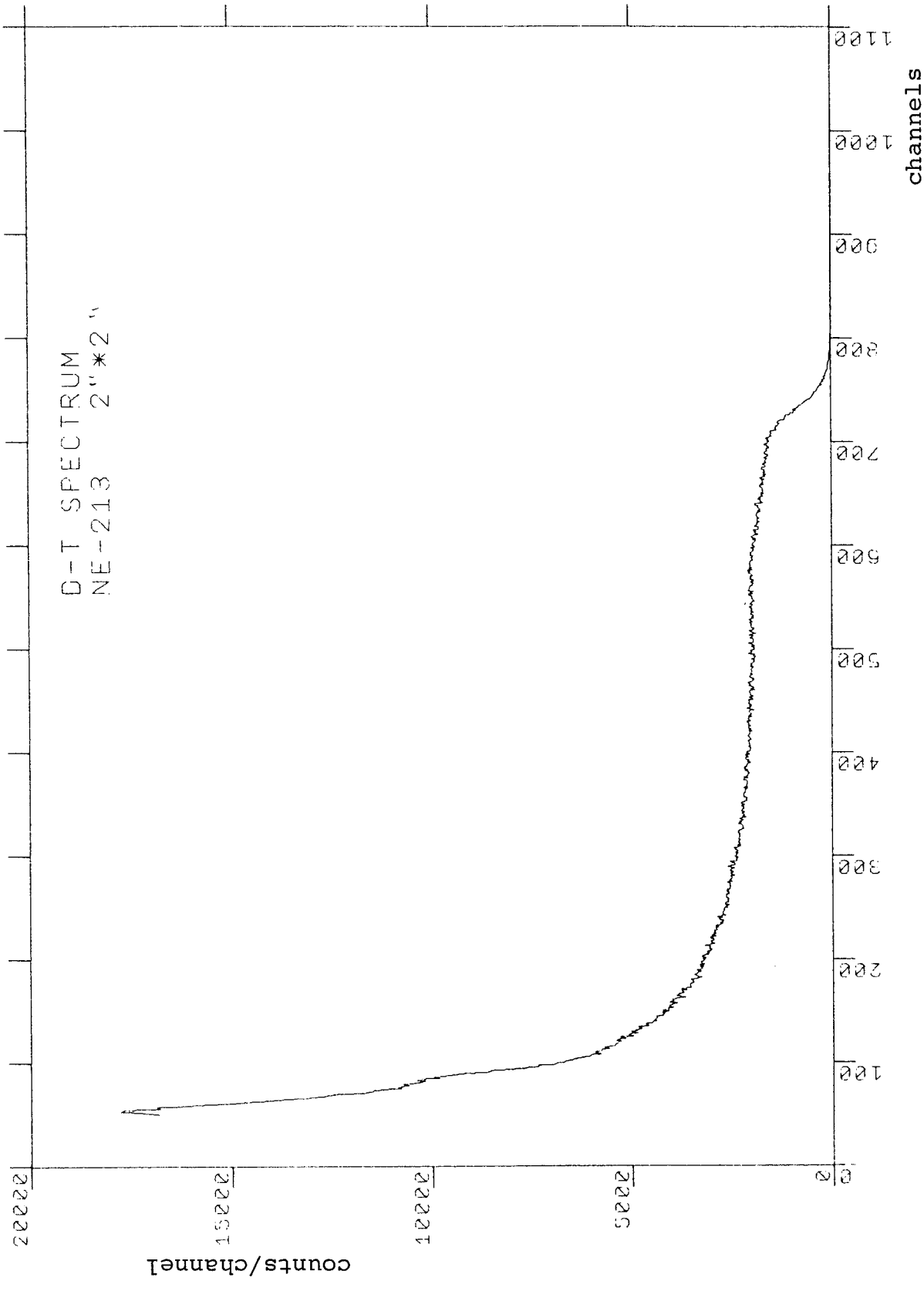

Fig.: 2.20: Pulse height spectrum measured with 2"x2" NE-213 detector of D-T neutrons

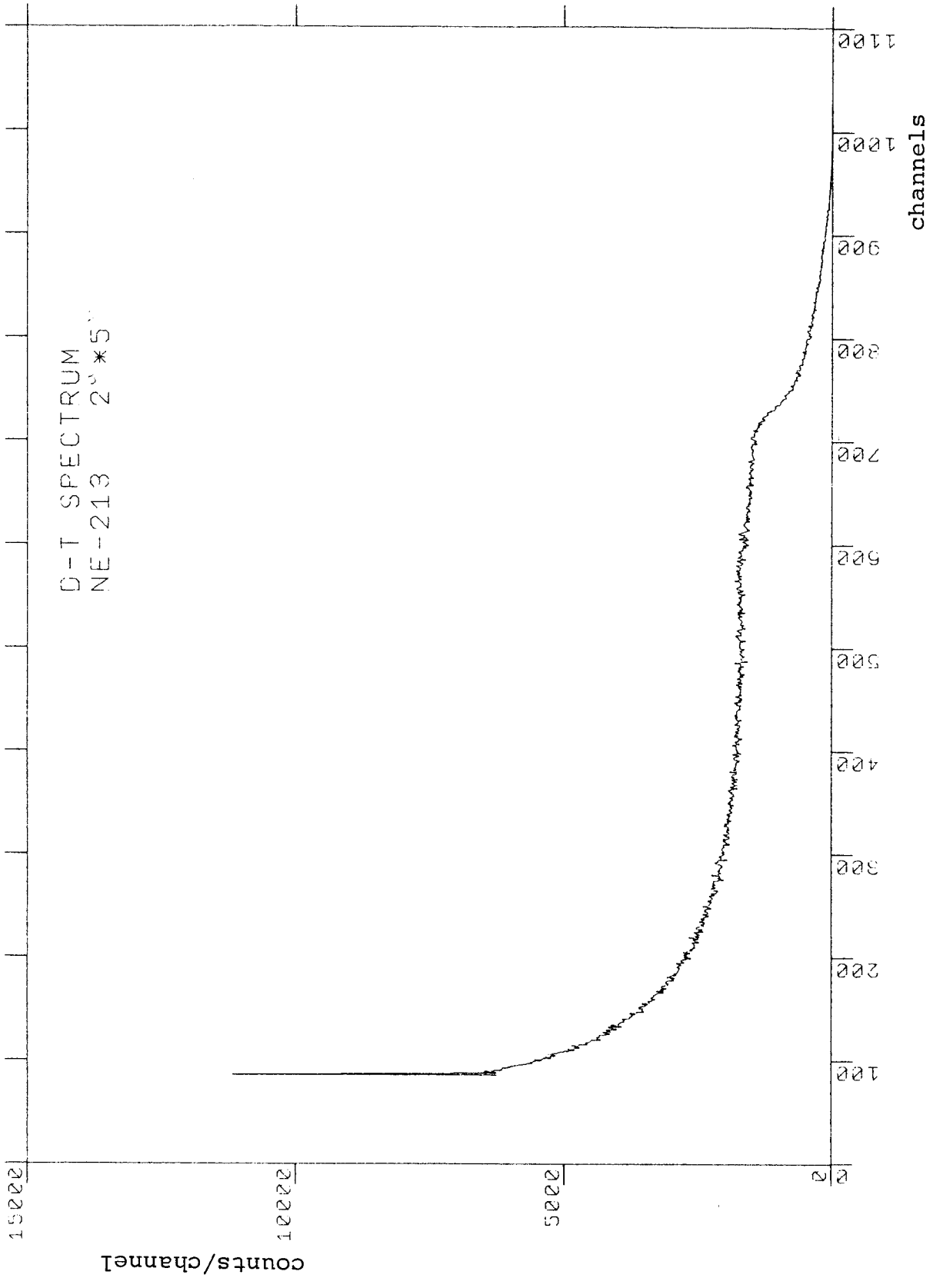

Fig. 2.21: The measured pulse height distribution of D-T neutrons with 2"x5" NE-213 detector

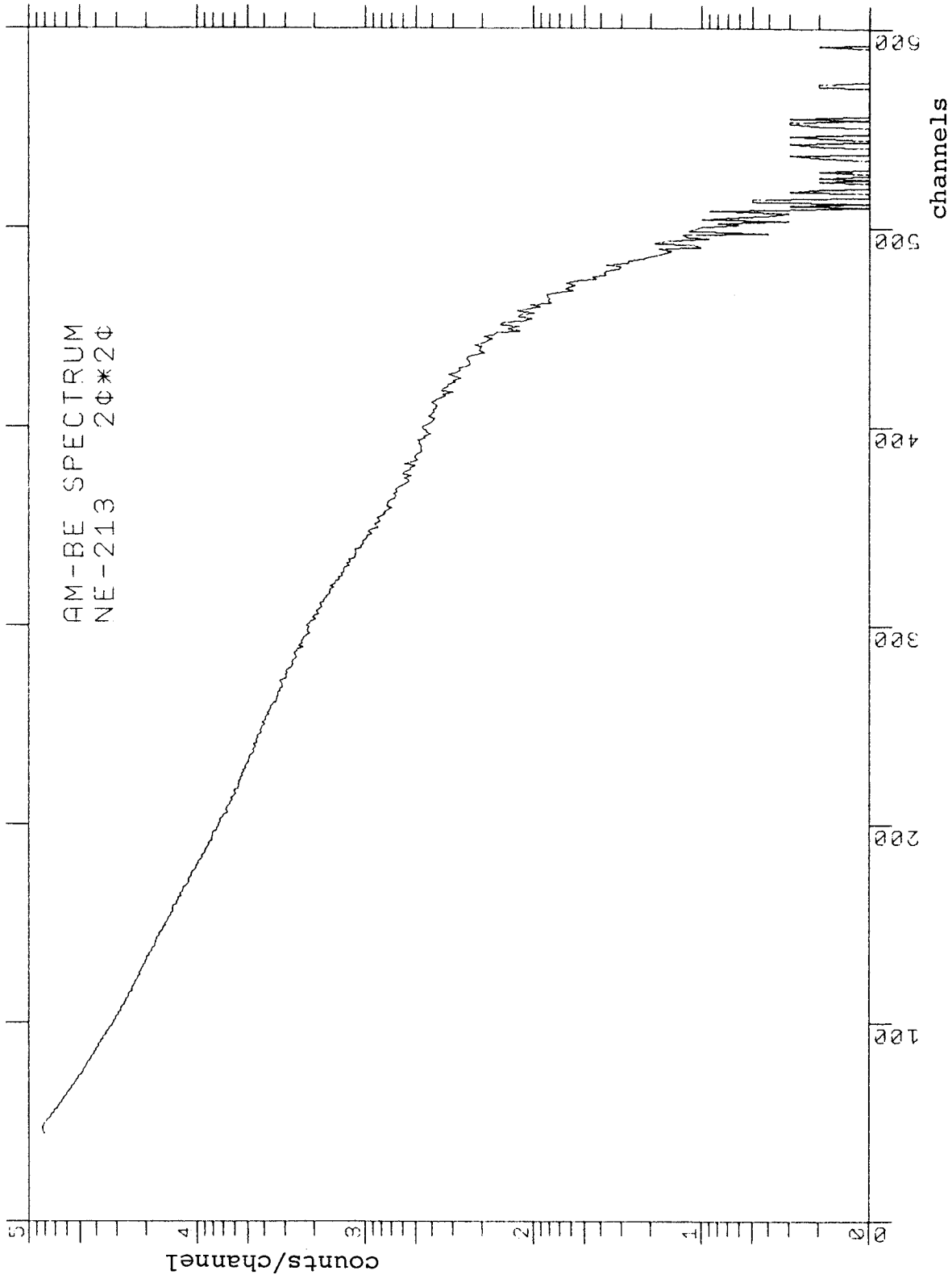

Fig. 2.22: Pulse height distribution of Am-Be neutron source measured with 2"x2" NE-213 detector

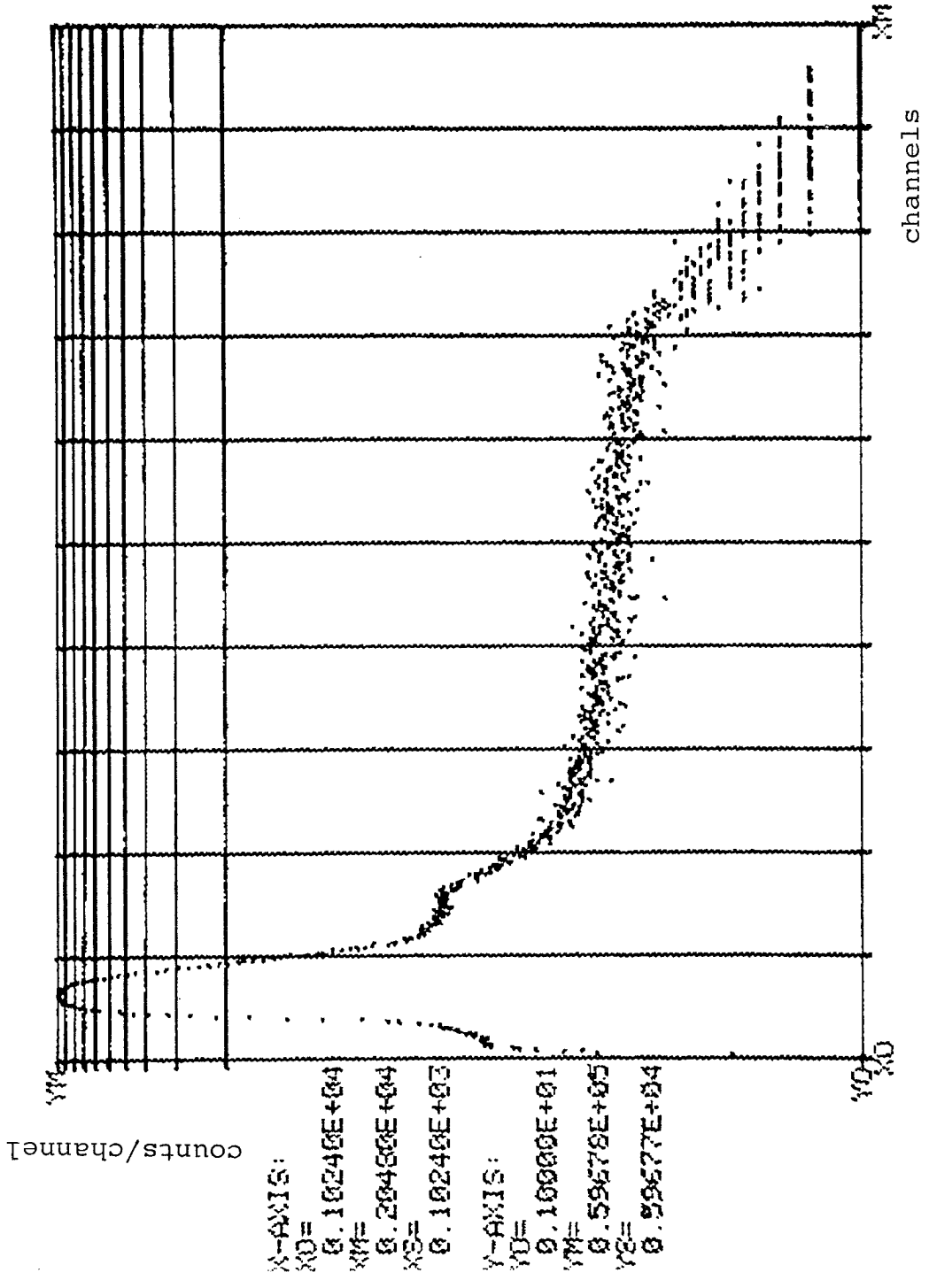

Fig. 2.23: Pulse height distribution of D-D neutrons measured with 2"x5" NE-213 detector

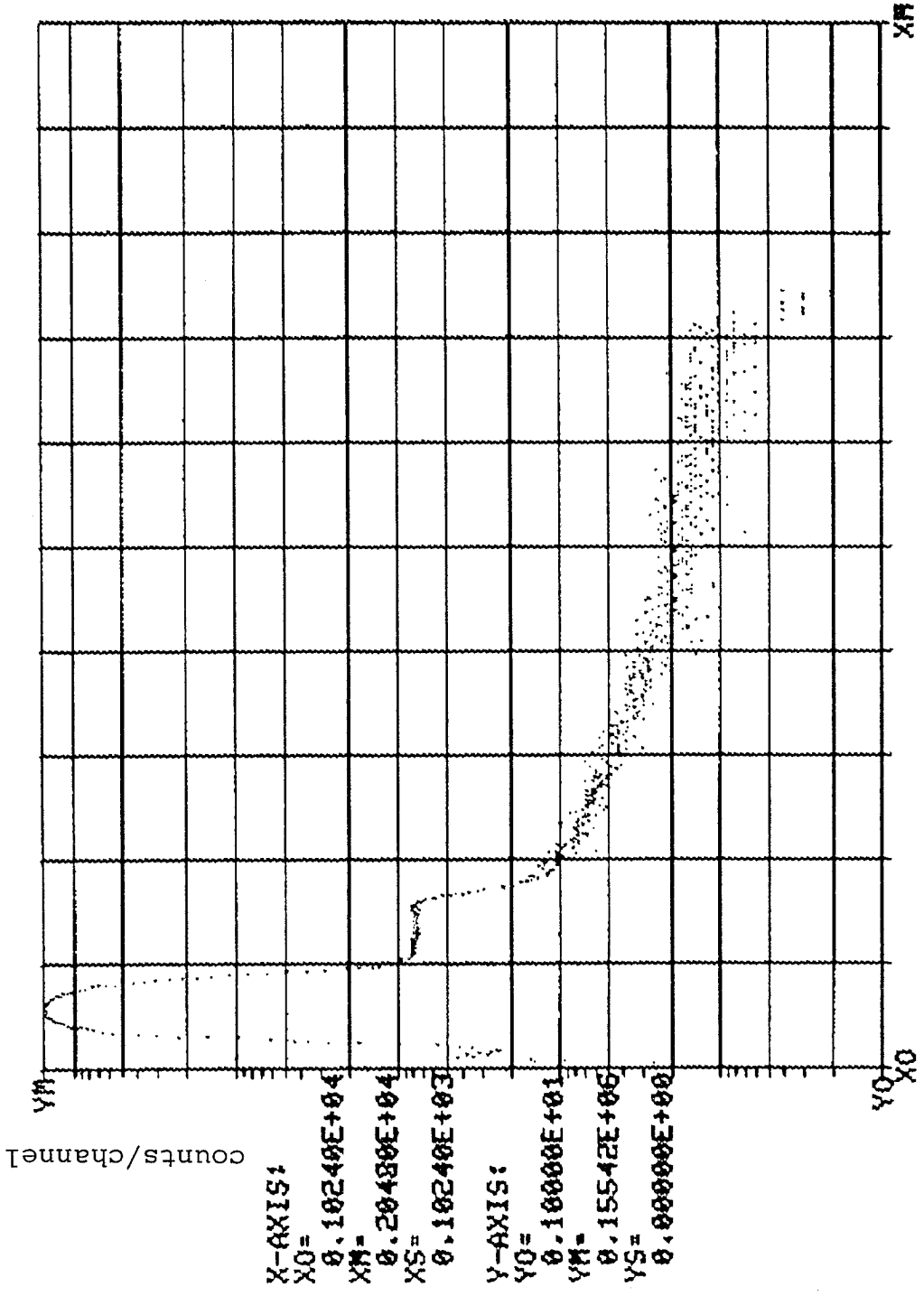

Fig. 2.24: Pulse height distribution of D-D neutrons measured with 2"x2" NE-213 detector

3. RESPONSE FUNCTION CALCULATION

3.1 Definition and General Form of a Response Function

The process of detection of fast neutrons by means of organic liquid scintillators is reasonably well understood /20/. The incident fast neutrons undergo elastic or inelastic scattering from, or induced reactions with, the scintillator nuclei - the only ones present in sufficient quantities are H and 12C - and the energies of the emerging charged particles are dissipated during the formation of ion pairs along the tracks of the recoiling particles. Ultimately, after recombination the ionization energy is released partly as heat and partly as fluorescence light, the latter subsequently being brought into photo sensitive device, e.g. photomultiplier (PM) tube, the output of which is handled by electronic methods. A response function is defined here as the probability (per unit pulse height) that a neutron of energy E_n produces an output pulse of height in the pulse height increment dL at pulse height L.

The response function of a certain detector has to be either measured experimentally of calculated via Monte Carlo calculations. Since there are difficulties in measuring a complete set of response functions the latter method is utilized.

3.2 Neutron Interactions in NE-213 Scintillator

As mentioned above, the principal interaction of fast neutrons with NE-213 is (n-p) scattering. The fact that the hydrogen to carbon ratio of NE-213 is 1.211 and that microscopic cross section of neutron-carbon (n-c) reaction has, broadly speaking the same value of n-p scattering cross section in our energy range of interest (1-18 MeV) would imply that (n-c) reactions play an

important role in fast neutron detection by NE-213. The possible neutron interactions in NE-213 below 18 MeV neutron energy are tabulated in Table 3.1 together with their reaction Q-value.

Table 3.1: Neutron Interactions in NE-213 Below 18 MeV

Reaction	Q-value (MeV)	Threshold (MeV)
H(n,n)H (elastic scattering)	0	0
$^{12}C(n,n)^{12}C$ (elastic scattering)	0	0
$^{12}C(n,n'\gamma)^{12}C$ (inelastic scattering)	-4.43	4.8
$^{12}C(n,\alpha)^{9}Be$	-5.71	6.18
$^{12}C(n,n'3\alpha)$	-7.65	8.3
$^{12}C(n,np)^{11}B$	-12.61	13.69

3.3 Monte Carlo Calculations

Many response function codes have been developed purely for detector efficiency calculations. Consequently only the accuracy of the integral efficiencies which these codes produce have been experimentally verified. One of these codes is STANTON N /21/, which is decided to use (after several improvements /22/) for the calculation of the response functions of our spectrometer. Some experimental check has to be carried out on the calculated response functions to assess their compatibility with the measurements and their sensitivity to the uncertainties in the data used.

3.3.1 Outline of the Calculation

The following outline provides an overall view of what is being done in this code.

1. Choose the kinetic energy E, direction cosines c(1) and position coordinates x(1) of the incident neutron.

2. Look up the total cross-sections for all interactions of a neutron of energy E with hydrogen and carbon by linear interpolation in the data table; find the nuclear mean free path in scintillator.

3. Choose, by Monte Carlo (MC) the distance D the neutron travels before interacting.

4. Propagate the neutron a distance D along directions c(1) to new position x(1).

5. Check whether x(1) is still inside the scintillator. If not, go to step 9.

6. Decide (by MC) whether the interaction occured in hydrogen or carbon, and if in carbon, through which channel it proceeded.

7. Call the subroutine corresponding to the chosen interaction channel. Each such subroutine has access to information on angular distribution, so that the energy and lab scattering angle of the outgoing neutron (if any) are found by subroutine SCATTR. The lab energies of all charged secondaries are similarly found, and their light output is calculated by the appropriate saturation function. The light output in each channel is added to the previous total for this history. Note: no charged prongs are followed: all are assumed to stop in the scintillator.

8. If the outgoing neutron has remaining energy E above some specified cutoff (e.g. 0.001 MeV) the program returns to step 2 and continues to follow the neutron

9. Resolution and Binning: Nine separate "differential pulse height analyzer" arrays are maintained, one for the light from each reaction channel (6 analyzers), three for the total light output subjected to different amounts of resolution broadening. Simulate by MC the jitter in light output due to finite resolution, and increment the two analyzers containing smeared spectra. Return to step 1 if more histories are to be run.

3.3.2 Physics Input

A. Processes contributing to neutron detection.

The following interaction channels have been simulated.

1. Elastic scattering from protons, np -> np. Below 5 MeV this is the significant channel producing a detectable recoiling charged particle, and it is the dominant detection mechanism for neutron less energetic than about 25 MeV.

2. Elastic scattering of neutrons from carbon, n+C -> n+C. Separate total cross-sections for diffractive and non-diffractive elastic scattering are available, and the two processes are treated differently. The light output (MeV electron equivalent) of the carbon recoil of lab energy E_C is taken to be $0.017\ E_C$.

3. Inelastic scattering from carbon, n+c -> n+c+γ (threshold, 4.7 MeV). This process contributes to the efficiency in two ways: a) As a source of neutrons of different direction and lower energy. b) The emitted 4.4 MeV γ-ray may be detected by Compton scattering in the scintillator. The contribution to the efficiency is typically small compared to the dominant np contribution in the range of our interest.

4. The inelastic reaction n+c -> α + 9Be (threshold 6.2 MeV). This channel makes a small contribution to the efficiency between 6 and 20 MeV through detection of the recoil alphas.

5. The inelastic reaction n+c -> n+3α (threshold 7.9 MeV). This channel and channel 6 below dominate the detection efficiency above 40 MeV.

6. The inelastic reaction n+c -> p+^{12}B (threshold 13.6 MeV). It is assumed a CM distribution for the proton which is identical to that for the neutron in channel 5.

7. Omissions not included in this program are the channels n+c -> n+p+^{11}B, n+c -> 3n+^{11}C, and the meson production channel at high energy. It is felt that the effects of the former can be adequately described by channels 5 and 6.

B. Light Output from Liquid Scintillator

It is necessary to take account of saturation effects in the light output of massive charged particles moving slowly. Light outputs in this program are expressed in MeV electron equivalent, which is the energy L of a stopping electron yielding the same amount of light as a heavy particle of energy E. For protons the conversion used is /22/

$$L_p = 0.83\ E_p - 2.82\ (1.0 - \exp(-0.25\ E_p^{0.93}))$$

while for alphas

$$L_\alpha = 0.41\ E_\alpha - 5.9\ (1.0 - \exp(-0.065\ E_\alpha^{1.01}))$$

C. Simulation of Finite Resolution

Because of the finite pulse height resolution of a real counter the measured pulse height spectrum is not identical to the intensity spectrum of light output from the scintillator, but has a resolution function folded in. The resolution is parameterized in this program by the one photoelectron level L_0, defined as that light output (in MeV) which is needed (on the average) to create one photoelectron in the photomultiplier looking at the scintillator. Differential and integral pulse height distributions are found for three values of L_0.

Simulation proceeds as follows. To the light output L for each history is added a "jitter" ΔL, chosen randomly from a Gaussian distribution. The standard deviation of the distribution is $\sigma_L = L_0 \, (L/L_0+0.5)^{1/2}$. Two values of ΔL are found, one for each non zero value of L_0. The smeared light output is then $L' = L + \Delta L$, except L' is set to zero if it is found negative.

D. Charged Particle Escape

For each charged particle produced by a simulated neutron interaction in the detector, the computer code has been extended to calculate the range of the charged particle in the scintillator. Each charged particle is propagated through the scintillator until it deposits all of its energy or until it leaves the scintillator. An empirical relation is used to determine the energy lost in the scintillator by particles which leave the scintillator. Only the energy deposited in the scintillator is used to determine the amount of light produced by a charged particle. The empirical range-energy expressions for protons are

$$\begin{aligned} \ln R &= 3.8103 + 1.6171 \ln T + 0.08193 \ln^2 T - \\ &\quad - 0.020363 \ln^3 T + 0.003147 \ln^4 T - \\ &\quad - 0.0002321 \ln^5 T, \\ \ln T &= 2.1964 + 0.56148 \ln R + 0.0010055 \ln^2 R - \\ &\quad - 0.00008885 \ln^3 R - 0.0001821 \ln^4 R + \\ &\quad + 0.00002742 \ln^5 R, \end{aligned}$$

and for alphas

$$R_\alpha = R_p \, (T_\alpha/4), \quad T_\alpha = 4T_p(R_\alpha).$$

The range R is expressed in millimeters and the energy T is in MeV.

E. Relativistic Kinematics

Stanton's original code treated all kinematics except that of the compton scatters nonrelativistically. The need to calculate detector efficiencies for high energy neutrons necessitate the modification of the code to include relativistic reaction kinematics for all channels.

3.4 Comparisons of Calculations with Available Published Results

Since the purpose of the Monte Carlo code is to provide reliable calculations of neutron counter efficiencies and response functions for different detector geometries, neutron energies, and detector thresholds, the best test of the code is comparison with a wide variety of published calculations and experimental measurements.

We present here comparisons of calculations with the improved code against many different experimental measurements of neutron counter efficiencies. The efficiencies near threshold are especially sensitive to various experimental parameters and are expected to be more difficult to reproduce accurately. As presently written, the efficiency code translates the energy deposited in the scintillator by a monoenergetic charged particle into a Gaussian pulse-height distribution. This Gaussian distribution function determines the shape of the calculated efficiency as a function of energy near threshold. For small pulse heights, the Gaussian approximation becomes invalid. The statistics of the Gaussian distribution function are determined in the computer code by the amount of energy deposited in the scintillator and by an input parameter specifying the amount of energy required to produce one photoelectron at the photocathode. As indicated in the report by Stanton, one may try to

reproduce the shape of a measured set of efficiencies near threshold by varying the energy per photoelectron parameter. We have not attempted to perform such adjustments; but instead we take the statistics to be determined by assuming an energy per photoelectron of 2 keV /23/. Because the Monte Carlo code needs to be modified to use a more accurate distribution function for small pulse heights, and because efficiencies near threshold are very sensitive to small errors in the assumed threshold value, the calculations should not be relied upon below about two times the threshold settings.

There are some measurements of the neutron detection efficiency of liquid scintillators available in the literature. Figs. 3.1 show the calculations of the code compared with the efficiency measurements. The low threshold measurements /24/ compare well with the calculations of the code in Fig. 3.1(a). These measurements were made with a NE-213 ($CH_{1.21}$) scintillator 3.8 cm thick and 12.7 cm diameter. In Fig. 3.1(b) we compare the calculations with the measurements /25/ for an NE-213 scintillator 5.6 cm thick and 12 cm diameter. The measurements extend from 1 MeV up to 25 MeV for three different thresholds. The agreement with the calculations is exceptionally good even for the low threshold of 0.256 MeV equivalent-electron energy. The calculated total (zero bias) efficiencies for our 2"x2" NE-213 detector are shown in Fig. 3.2 compared to these calculated for the same detector with the O5S Monte Carlo code /26/. The agree ment between the two codes is especially good above 1 MeV neutron energy. The discrepancy between the two curves below 1 MeV seemes to be due to a threshold in the modified Stanton Monte Carlo code. Because the proton recoil energy distribution extends all the way to zero, some recoil events will inevitably be eliminated in the threshold setting. Therefore, the efficiency assuming that all pulses are counted is sometimes called the "zero-bias" efficiency, and a real detector with a finite discrimination level will always have a somewhat lower efficiency particularly at low neutron energies.

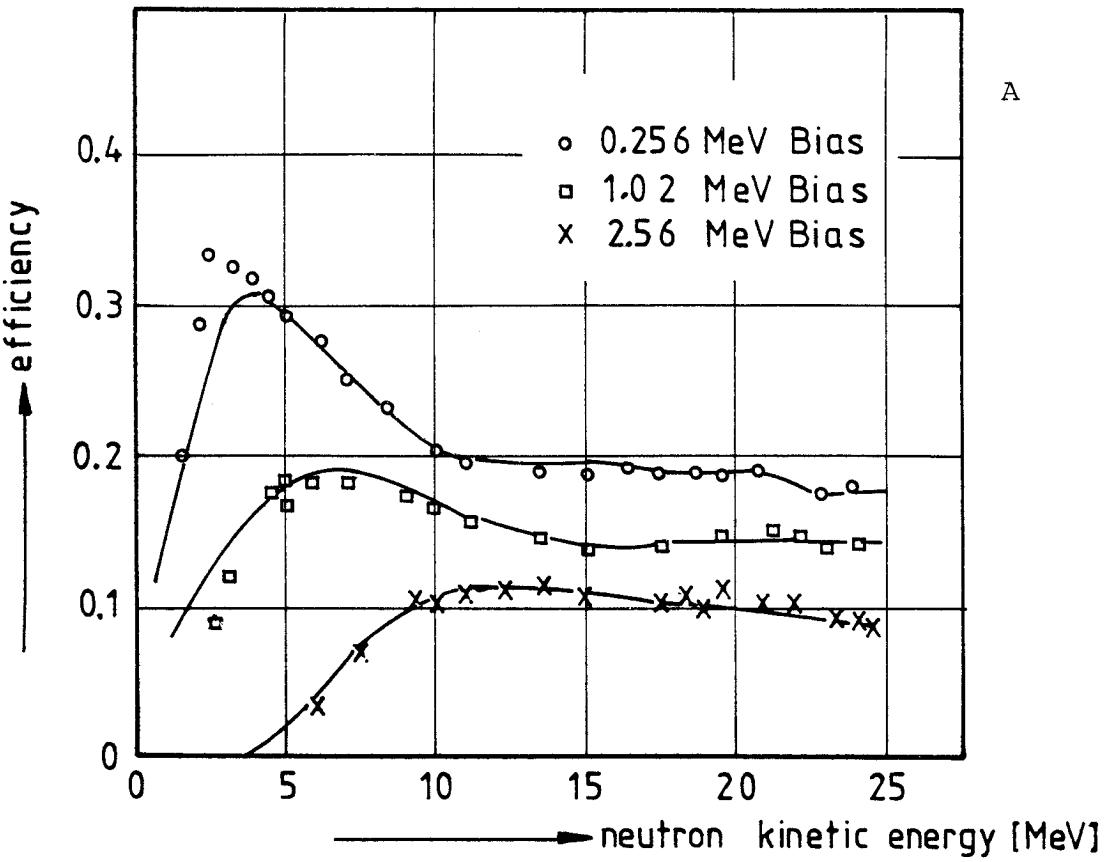

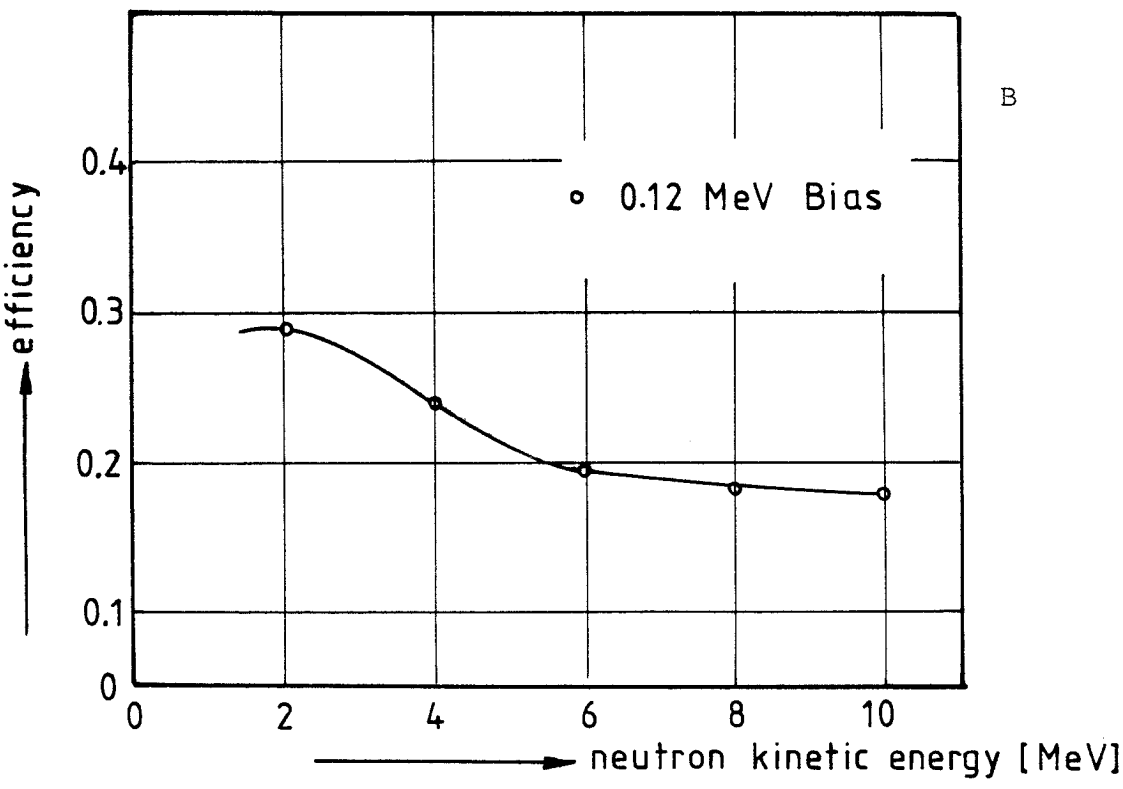

Fig. 3.1: Comparison of efficiency measurements with calculations of the Monte Carlo computer code for NE-213 liquid scintillator

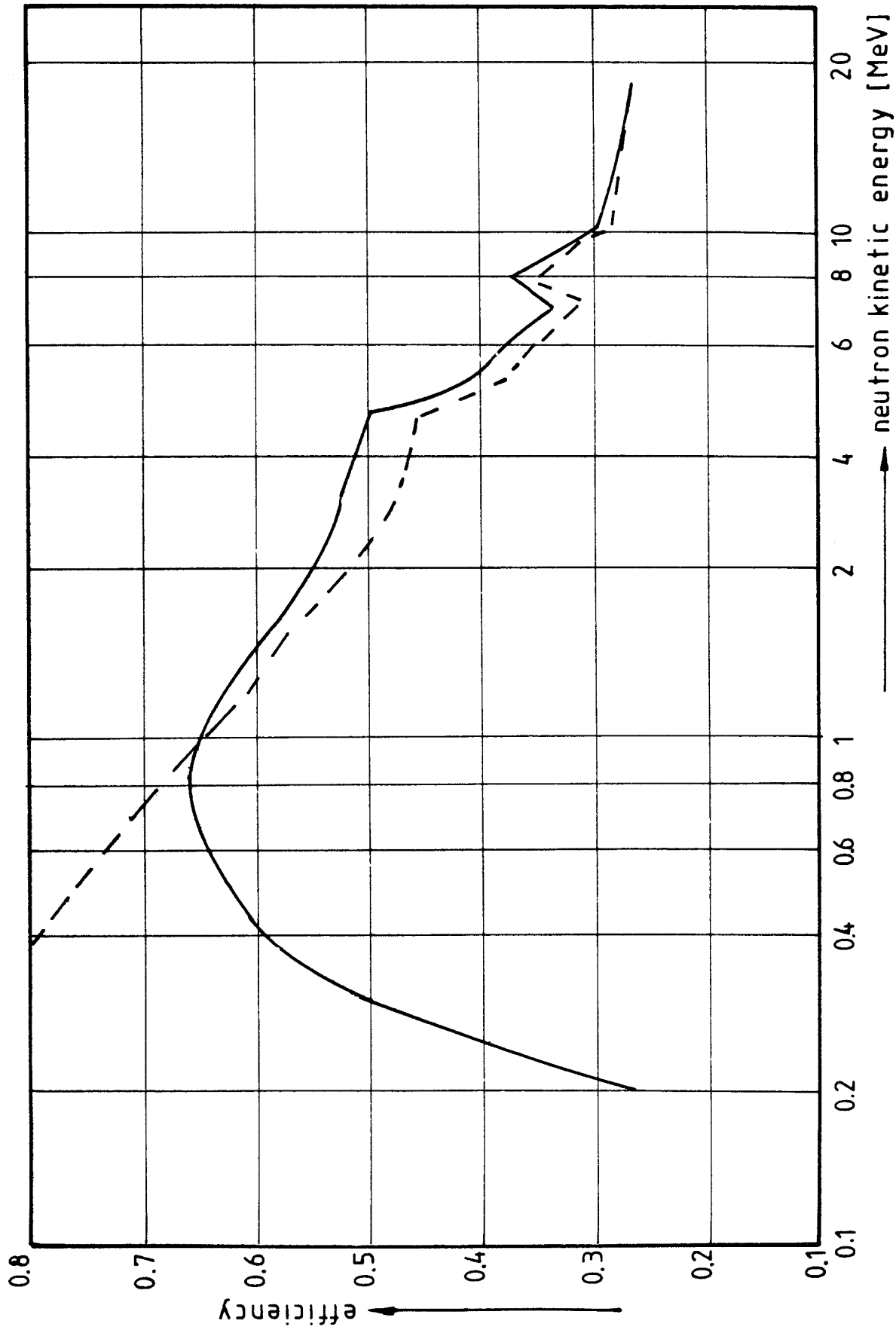

Fig. 3.2: Comparison of the calculated efficiencies of 2"x2" NE-213 scintillator. The dashed line calculated with the O5S Monte Carlo code and the solid line with the modified Monte Carlo code

The calculated efficiency for the 2"x5" NE-213 detector is shown in Fig. 3.3.

The pulse height distributions for neutrons from 1 MeV up to 18 MeV were calculated for both detectors, 2"x2" and 2"x5". Unfortunately, no other response functions calculated with this Monte Carlo code were found in the available literature. These response functions were compared with those measured and shown in chapter 2. The calculated pulse height distributions were convoluted with a Gaussian smearing function and integrated over the width of each pulse height bin, so that they matched the measured pulse height distributions. After fitting the experimental data, the Monte Carlo calculations and Gaussian smearing were finally carried out at the midband energy of each monoenergetic neutron group. The flat region, the recoil proton plateau, of each measured pulse height distribution was then normalized to the corresponding region of the Monte Carlo calculated pulse height distribution for the same neutron energy. This normalization is equivalent to equating the area of the experimental curve that lies above the lowest point on the proton recoil plateau to the area of the calculation above the same pulse height. Such normalization produces accurate absolute measured results. In this region the hydrogen recoil events predominate and the cross section uncertainties tend to effect calculated response functions least in this pulse height region. Thus the best features of both the calculations and the measurements were combined.

Fig. 3.4 through Fig. 3.7 illustrate these comparisons between the measured and calculated response functions for monoenergetic neutrons of 2.5 MeV and 14 MeV for both detectors 2"x2" and 2"x5". These curves show good agreement between measurements and calculations which will be further tested after unfolding these pulse height spectra.

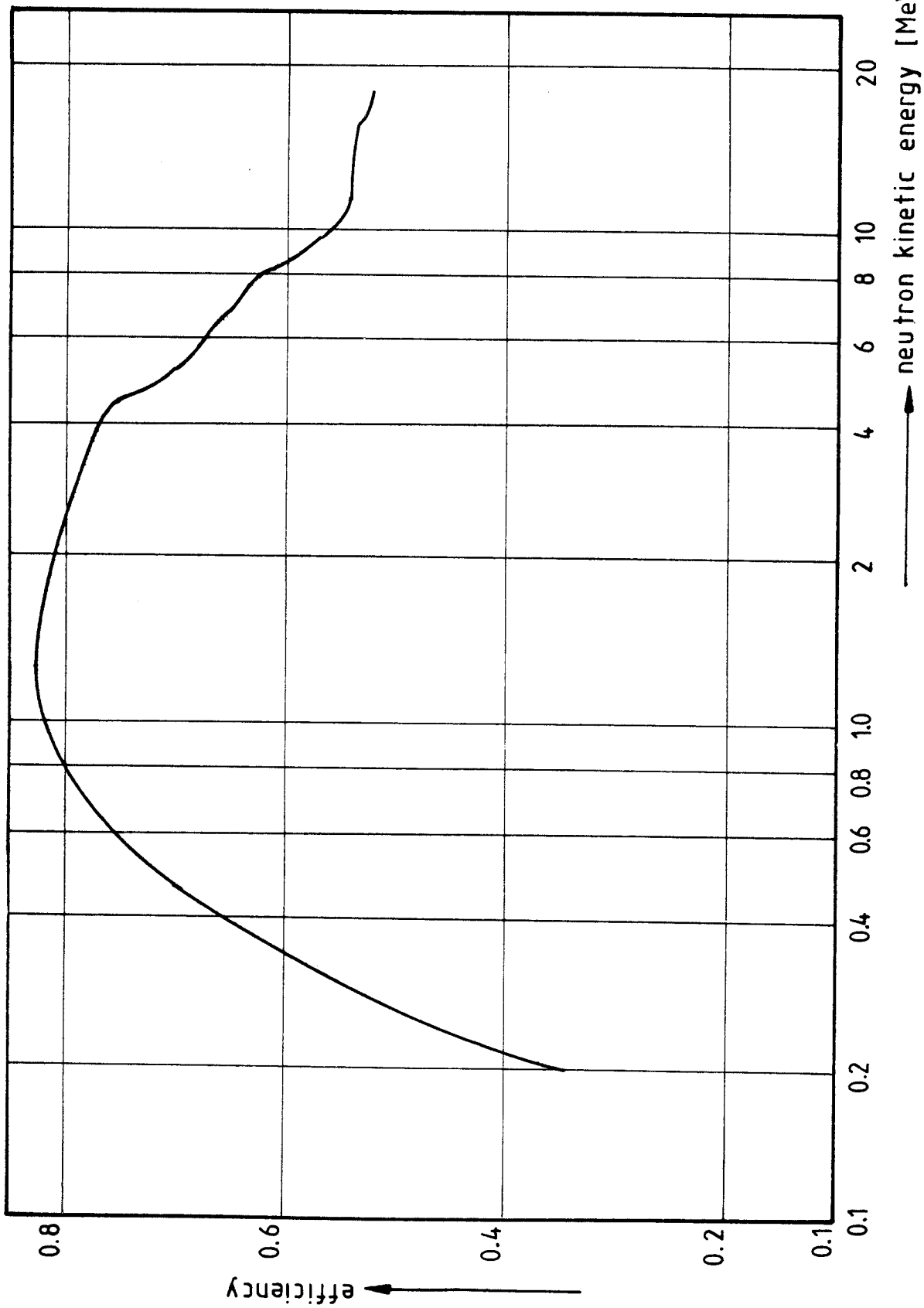

Fig. 3.3: The calculated effciency of the 2"x5" detector

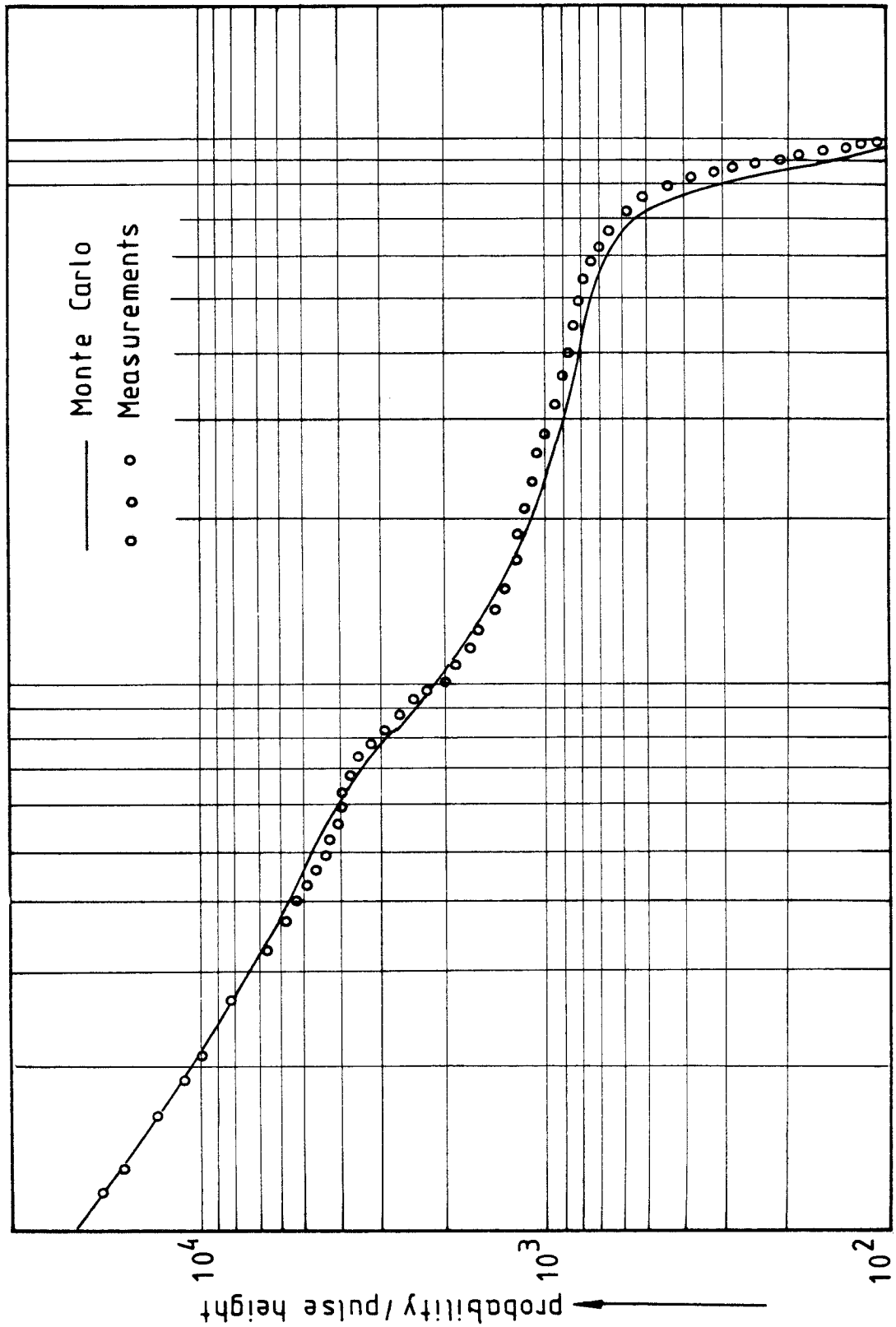

Fig. 3.4: Comparison of prediction (via modified Monte Carlo) and measurement of a 2.5 MeV response function with 2"x2" NE-213 detector

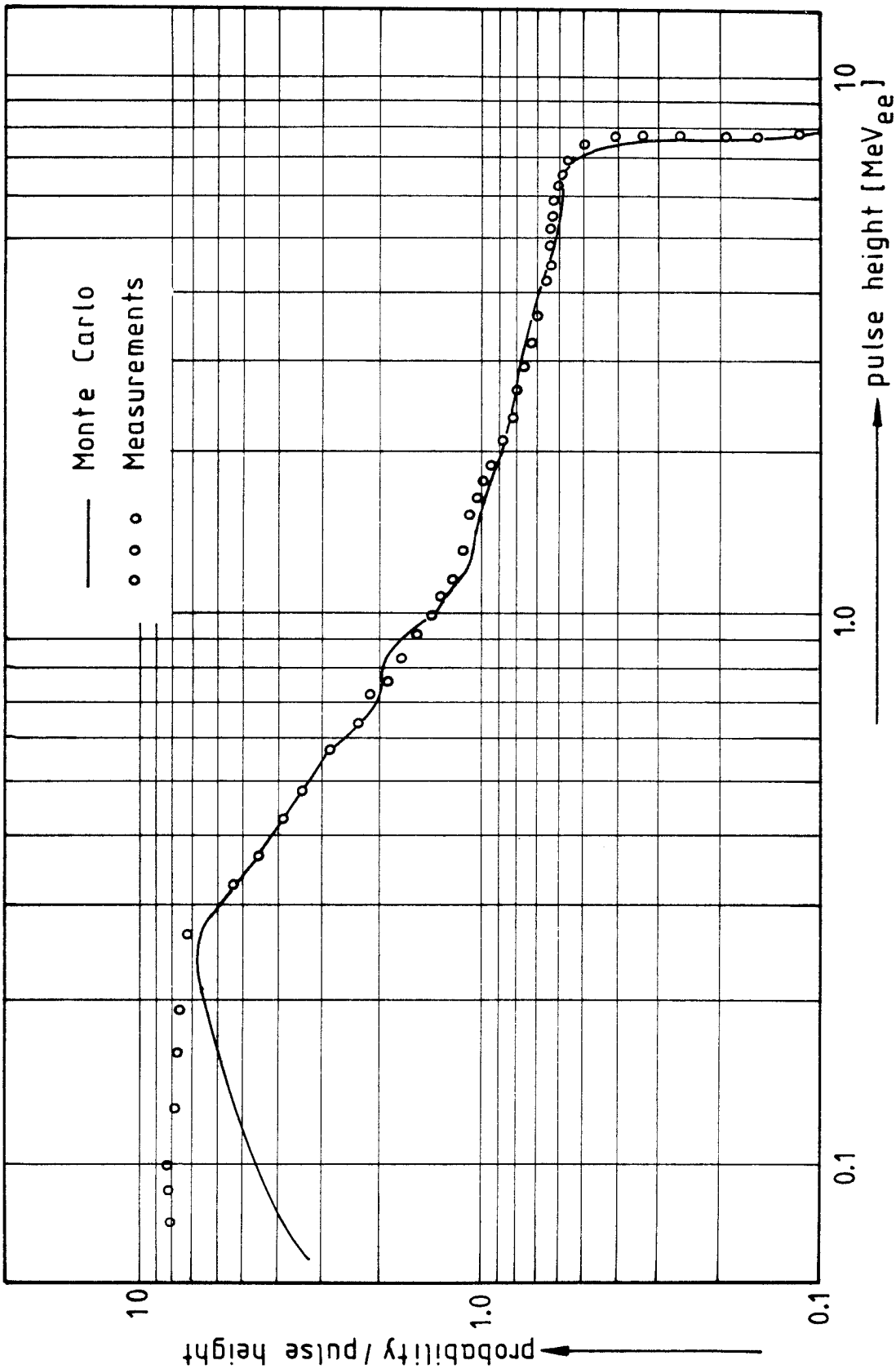

Fig. 3.5: The measured and calculated response functions of 14 MeV with the 2"x2" NE-213 scintillator

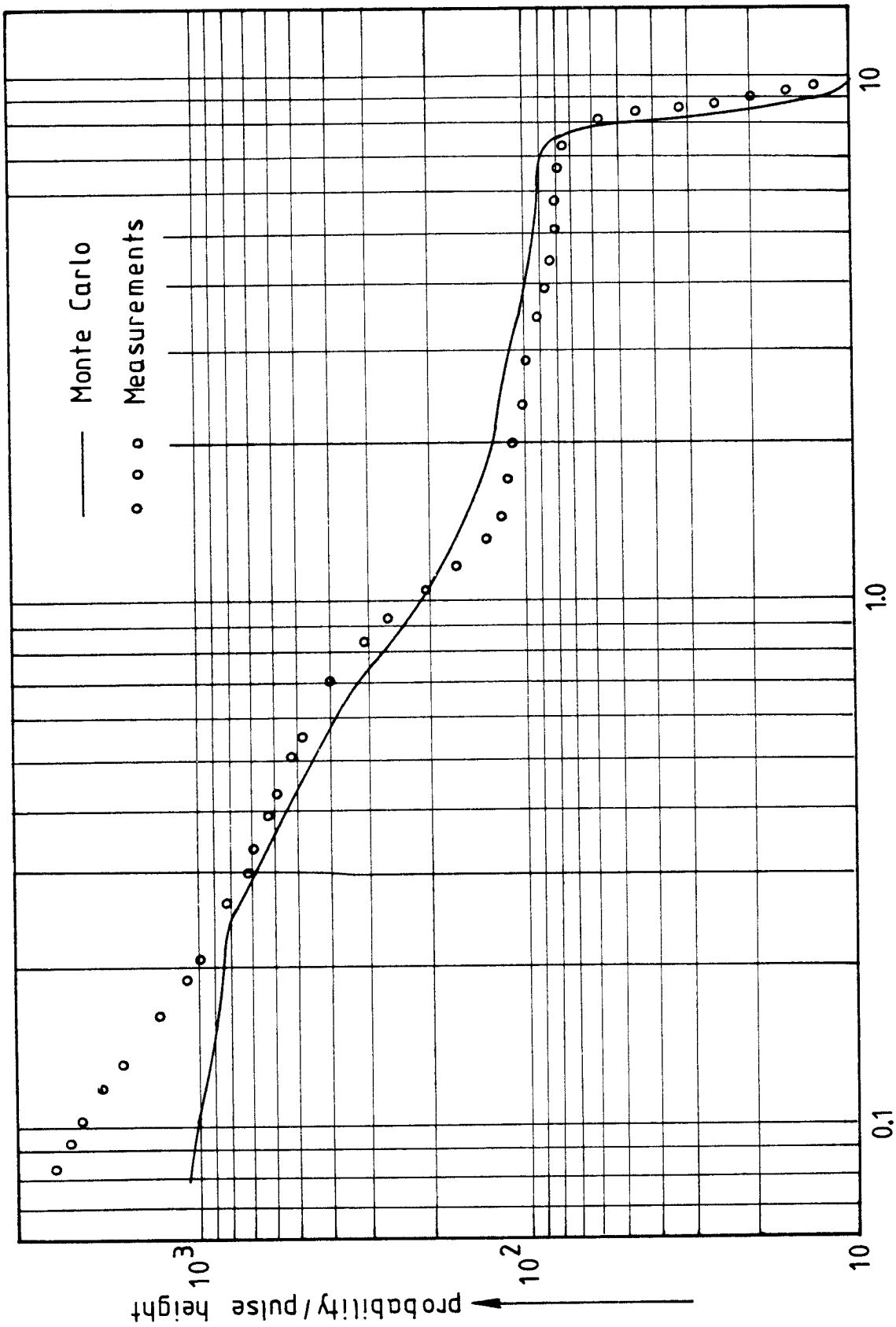

Fig. 3.6: Comparison of measured and calculated response functions of 14 MeV with 2"x5" NE-213 detector

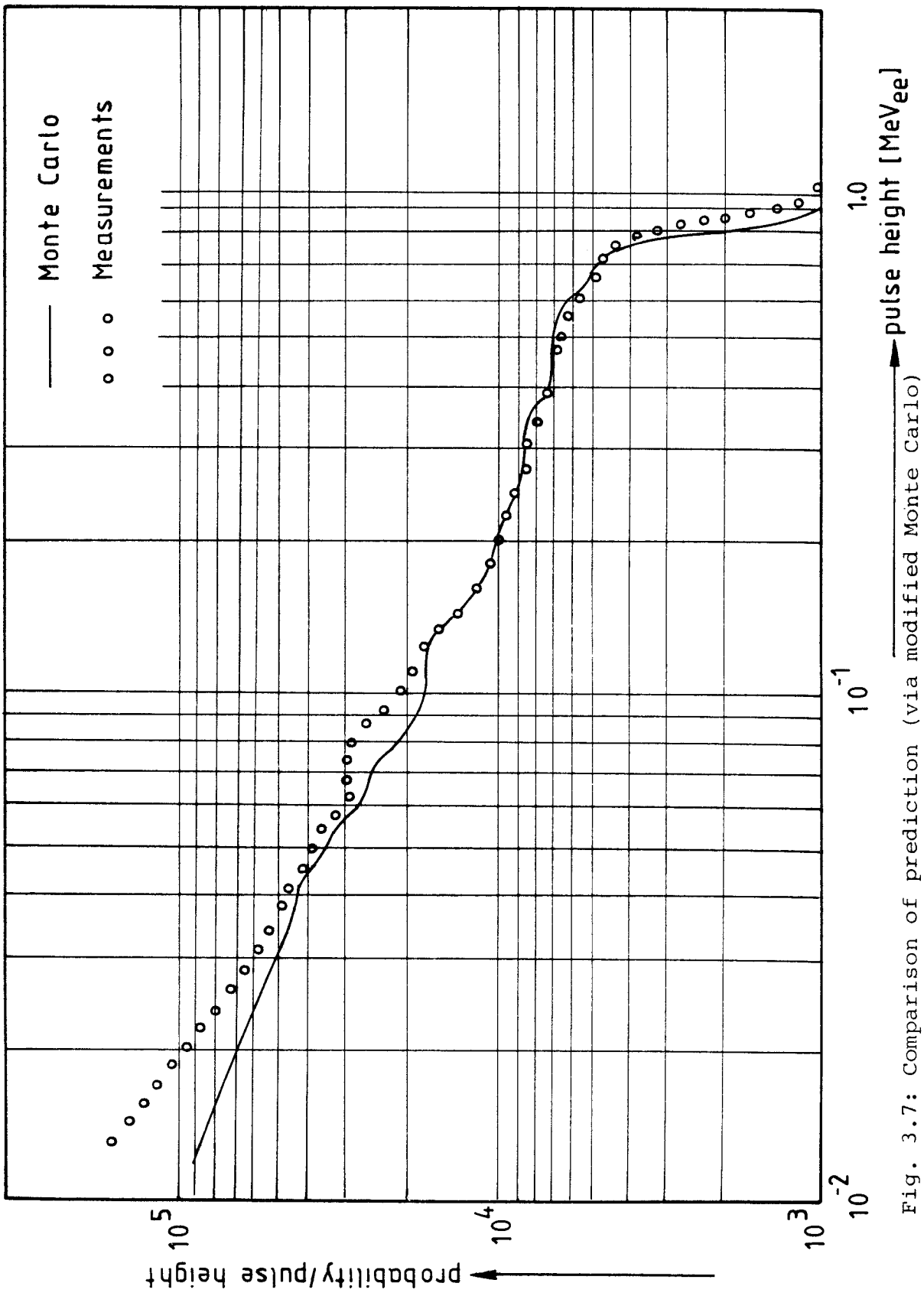

Fig. 3.7: Comparison of prediction (via modified Monte Carlo) and measurement of 2.5 MeV response function with the 2"x5" NE-213 scintillator

3.5 The Response Matrix Generation

Vital to the FERDOR unfolding code is the existance of an accurate and detailed family of monoenergetic response functions, that is, a numerical matrix which accurately describes the pulse height response of a unique organic scintillator (unique in terms of atomic composition, shape and physical dimension) to monoenergetic neutrons, closely spaced in energy over the entire energy range of interest. It was noted that a complete set of absolute response functions could not be obtained experimentally for our spectrometer. It was therefore necessary to resort the calculation methods. The Monte Carlo code predicts the response function of our spectrometer with both detectors to 2.5 MeV and 14 MeV neutrons reasonably well, as shown in Figs. 3.4 - 3.7, and hence this was assumed to be the case at other energies. A total of 20 response functions were then calculated using the Monte Carlo code, spanning the energy range 1 to 18 MeV.

Since the ADC's used in collecting the measured pulse height distributions almost inevitably has better resolution than the scintillator itself, it is logical, before treating the data, to collect it into groups, or bins. It is most convenient to do this in terms of light units (MeV electron equivalent), or "V" space. The output of the Monte Carlo response generation code, on the other hand, is most conveniently treated and binned as a function of the resolution width of the detector. This space is called "Rho-space". Thus pulse-height data is treated as a function of V-space equal width bins in terms of MeV, while Monte Carlo data is treated within the frame work of Rho-space, bins having approximately equal widths in terms of resolution width. The mapping from one space to the other is related simply by $Rho=\sqrt{V}$.

Since the pulse height distribution consists of several hundred channels, and it is desired to compact the data to a smaller number of bins to minimize the computational time, and to reduce statistical variance (at the expense of broader bins) and to put the data in a more compact form. Because it is generally not necessary to employ more than 2 1/2 or 3 pulse-height channels per resolution width, FWHM (full width at half maximum), of the pulse height distribution, the use of uniformly spaced channels provides more information than can be effectively utilized by any analysis method. (The resolution of the pulse height distribution is determined by multiple neutron scattering combined with scintillation nonlinearity and by statistical fluctuations in the light collection and photomultiplier conversion. In order to reduce the amount of data, the measured pulse height distribution is sorted into 113 bins (NR, number of rows of the response matrix), such that there are at least two bins per FWHM.

The set of energies, which are used as points at which pulse height response functions are specified, are generated nonuniformly so that there are approximately 2 or 3 points per energy resolution width. For this purpose, the algorithm also considers the sequence of pulse height values which correspond to the selected energy. These points are made to vary in proportion to the pulse height resolution. Then the pulse height points are translated back to energy points.

A "rubber sheet" interpolation /27/ is performed between the Monte Carlo response functions to calculate a point on the final response function for a given energy and pulse height interval to generate the response matrix, element by element. The rubber sheet interpolation technique is diagramed in Fig. 3.8. Curve A (response function at energy E_{lo}) has its edge at L_{lo} and curve B (response function at energy E_{up}) has its edge at L_{up}. It is desired to interpolate a curve (response func-

tion) at energy E between E_{lo} and E_{up}. The edge of the desired response function would be at L (from the energy/light curve). Curve A is stretched so that its edge shifts to L and curve B is shrunk until its edge is also at L. Stretching and shrinking are done by replacing the abscissa, R, of the curves by RxSTRTCH, where STRTCH is a factor greater than 1.0 for a stretch, or by RxSHRINK, where SHRINK is a factor less than 1.0 for shrink. The interpolated curve is then obtained by simple linear interpolation is carried out by multiplying the ordinates of A by F and those of B by 1-F, where

$$F = (E-E_{lo}) \; / \; (E_{up} - E_{lo}).$$

It is important to note that the most difficult part of this study was to generate two accurate matrices for the two detectors used in our measurements.

The response matrices used in this study are composed of 113 rows (pulse height mesh) and 70 columns (neutron energy mesh). The pulse height of the matrix covers the region of 0.01 MeVee to 12 MeVee and the energy ranges from 1 MeV to 18 MeV.

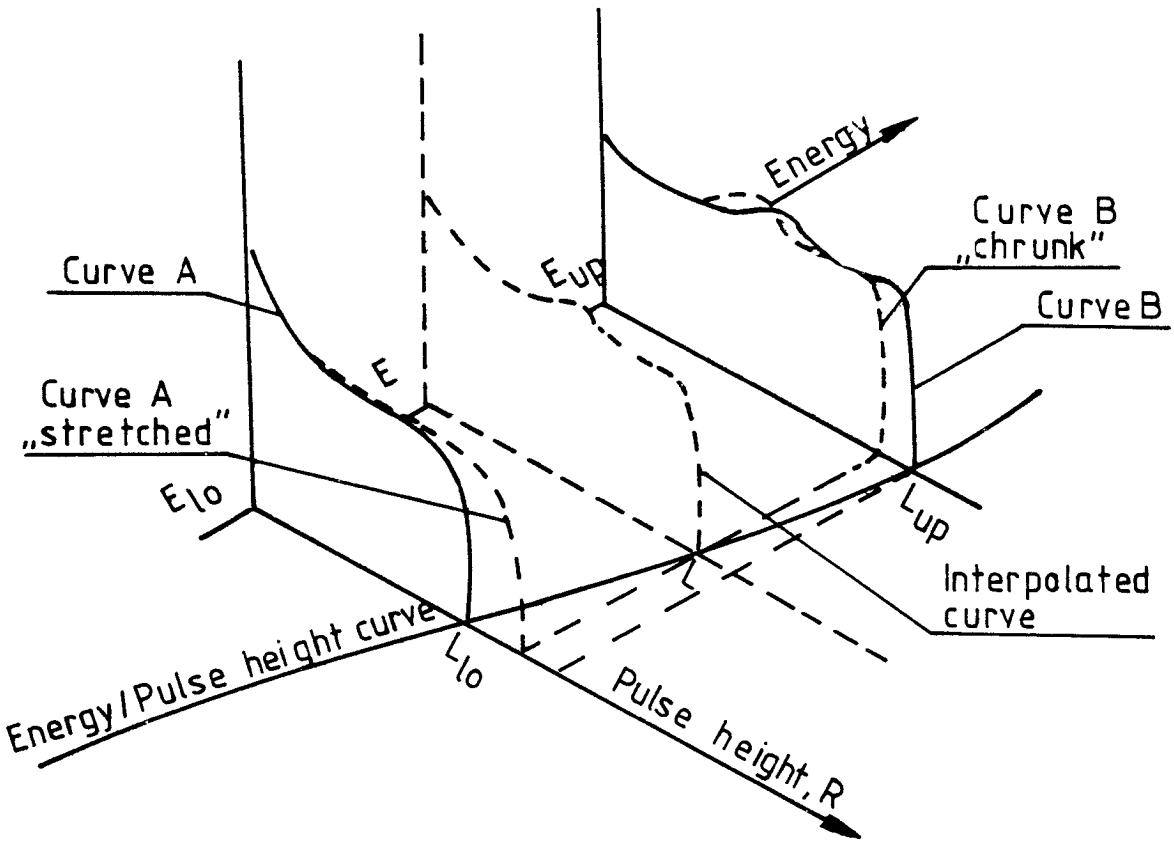

Fig. 3.8: Ruber sheet interpolation technique

4. NEUTRON SPECTRUM UNFOLDING

4.1 Derivation of the Matrix Unfolding Problem

NE-213 spectrometry systems can be used to measure neutron spectra accurately if the neutron and gamma-ray counting rates are not excessively high. The response of NE-213 spectrometry systems will be nonlinear if the counting rates are too high. For reasonable counting rates, though, the neutron unfolding problem may be represented as a linear integral equation

$$M(E) = \int_0^{\infty} R(E,E')\, T(E')\, dE' \qquad (4.1)$$

where T(E') is true neutron energy spectrum, M(E) is the measured spectrum, and R(E,E') is the response function of the spectrometry system. The measured spectrum must be due to neutron events only. Hence pulse shape discrimination techniques must be used to discriminate against gamma-ray events.

The integral unfolding problem given in Eq. (4.1) must be reduced to a matrix unfolding problem which can be solved numerically. The approximation that is made in obtaining the matrix unfolding problem is that the true spectrum is approximated by

$$T(E') \approx \sum_{J=1}^{NC} \chi_J\, \sigma(E' - E'_J) \qquad (4.2)$$

where NC is the number of energy points used in the approximate representation of the true spectrum. Different approximations will also lead to a matrix unfolding problem, but the approximation given in Eq. (4.2) has the advantage that it is both simple and easily interpreted. Substituting Eq. (4.2) into Eq. (4.1) yields

$$M(E) = \sum_{J=1}^{NC} R(E,E'_J)\, x_J \qquad (4.3)$$

In practice. the measured spectrum is determined using ADC and the counts are binned according the pulse height. The number of binned counts in the i^{th} pulse height bin is obtained by integrating the measured spectrum over the bin width. Let the average number of binned counts per unit pulse height for the i^{th} channel be y_i, then the average number of binned counts per unit pulse height y_i is obtained simply by dividing the number of binned counts for the i^{th} pulse height bin by the bin width. Thus, by integrating Eq. (4.3) over the i^{th} pulse height bin, the matrix unfolding equation is found to be given by

$$y_i = \sum_{J=1}^{NC} Ai_J\, x_J \qquad i=1...NR \qquad (4.4)$$

where NR is the number of pulse height bins and the matrix element Ai_J is given by

$$Ai_J = (E_i - E_{i-1})^{-1} \int_{E_{i-1}}^{E_i} R(E,E'_J)\, dE \qquad (4.5)$$

where E_i is the upper limit of the i^{th} pulse height bin. In Eq. (4.4) y is the measured vector. A is the response matrix and x is the solution vector.

4.2 The FERDOR Unfolding Method

The FERDOR /28-31/ unfolding method is widely used to unfold neutron energy spectra from pulse height spectra measured with NE-213 spectrometry systems /32-38/

FERDOR does not solve the unfolding problem exactly. It can and usually will give results that fluctuate between negative and positive, particularly before smoothing, but it will tend to confine the range of these fluctuations to some vicinity of zero.

$$-q_j < x_j < q_j \tag{4.6}$$

by solving a modification of the original matrix equation, while effectively ignoring the exact constraint

$$0 < x_j \tag{4.7}$$

It substitutes the tendency "x will probably be in the vicinity of zero" for the constraint "x will certainly be nonzero", because the tendency problem can be treated using the long-established method of least squares. The methods of calculus break down for strict constraint problems and their solution requires the newer and still less understood methods of dynamic programming.

4.2.1 Least Squares Problem and its Solution by Gram-Schmidt Orthogonalization

The problem of solving

$$y_i = \sum_{j=1}^{NC} A_{ij}x_j, \quad i=1.....NR \tag{4.8}$$

may be restated as the problem of minimizing the distance ϵ between the folded spectrum

$$\sum_{J=1}^{NC} A_{ij}x_j$$

and the data vector y. This distance is defined by the weighted sum-of-squares

$$\epsilon^2 = \sum_{i=1}^{NC} \omega \left(y_i - \sum_{j=1}^{NC} A_{ij}x_j\right)^2 \qquad (4.9)$$

where the weight vector ω is usually taken to be the set of inverse meansquare errors in y, so accurate components are weighted proportionately more than inaccurate ones. When A is not a square invertible matrix, for example when the problem is overdetermined by y having more components than x, there is no unique solution to the matrix equation but there is a unique solution to the problem

$$\text{minimize } \epsilon^2 \qquad (4.10)$$

This is the least squares problem.

Calculus may be applied to the solution of the least squares problem. Set

$$\frac{\delta\epsilon^2}{\delta x_k} = 0 \text{ for all } k = 1.....NC \qquad (4.11)$$

and you obtain

$$0 = -2 \sum_{i=1}^{NC} \omega_i A_{ik} \left(y_i - \sum_{j=1}^{NC} A_{ij}x_j\right)$$

or by rearranging and dropping indices

$$x = (\tilde{A}WA)^{-1}\,\tilde{A}Wy \qquad (4.12)$$

where

$$\tilde{A}_{ij} = A_{ji} \text{ or } \tilde{A} = A \text{ (transpose)}$$

$$W_{ij} = \begin{cases} \omega_i & \text{if } i=j \\ 0 & \text{if } i \neq j. \end{cases}$$

This formal solution consists of NC equations known as the "normal equations" of least squares.

Solution by the Gram-Schmidt orthogonalization is motivated by the observation that the normal equations can be simplified by finding a square matrix U that orthogonalizes A, meaning that Q = AU has the weighted orthogonality property

$$\tilde{Q}WQ = \text{unit matrix } I \qquad \tilde{Q} = \text{transpose } Q \qquad (4.13)$$

Then if $A=QU^{-1}$ and $A=U^{-1}Q$ are substituted into the normal equations, the result simplifies to

$$x = U(\tilde{Q}WQ)^{-1}\,\tilde{Q}Wy \qquad (4.14)$$

Because of the orthogonality property this further simplifies to

$$x = U\tilde{Q}Wy. \qquad (4.15)$$

Orthogonalization of A makes it unnecessary to invert $(\tilde{A}WA)$. The weight matrix may be eliminated from the orthogonality condition by defining

$$B_{ij} = A_{ij}/\sqrt{\omega_i} \qquad (4.16)$$

If U orthogonalizes A with weight W it orthogonalizes B without weights so that R=BU obeys

$$\tilde{R}R = \tilde{Q}WQ = I \qquad \tilde{R} = \text{transpose } R \tag{4.17}$$

and conversely if U orthogonalizes B without weights it orthogonalizes A with weight W. Once R is found, QW is just

$$(\tilde{Q}W)_{ij} = \tilde{R}_{ij}/\sqrt{\omega_i} \tag{4.18}$$

The Gram-Schmidt process is a technique for changing a set of skew vectors into a set of mutually orthogonal vectors of unit length by taking linear combinations. The columns of the matrix B are the skew vectors

$$\left(\vec{b}^{(j)}\right)_i = B_{ij} \tag{4.19}$$

Start with the first vector and normalize it to unit length

$$\vec{r}^{(1)} = \frac{\vec{b}^{(1)}}{\sqrt{\vec{b}^{(1)}\ \vec{b}^{(1)}}} = \vec{b}^{(1)}U_{11} \tag{4.20}$$

From the second vector $b^{(2)}$ subtract the part parallel to $r^{(1)}$:

$$\vec{b}^{(2)'} = b^{(2)} - \vec{r}^{(1)}\ (\vec{r}^{(1)}\ \vec{b}^{(2)}) \tag{4.21}$$

Normalize to obtain $\vec{r}^{(2)}$

$$\vec{r}^{(2)} = \frac{\vec{b}^{(2)'}}{\sqrt{\vec{b}^{(2)'}\ \vec{b}^{(2)'}}} = \vec{b}^{(1)}\ U_{12} + \vec{b}^{(2)}\ U_{22} \tag{4.22}$$

To get $\vec{r}^{(3)}$ take $\vec{b}^{(3)}$, subtract parts parallel to either $\vec{r}^{(1)}$ or $\vec{r}^{(2)}$

$$\vec{b}^{(3)'} = b^{(3)} - \vec{r}^{(1)}\ (\vec{r}^{(1)}\ \vec{b}^{(3)}) - \vec{r}^{(2)}\ (\vec{r}^{(2)}\ \vec{b}^{(3)}) \tag{4.23}$$

and normalize

$$\vec{r}(3) = \frac{\vec{b}(3)'}{\sqrt{\vec{b}(3)' \cdot \vec{b}(3)'}} = \vec{b}(1)U_{13} + \vec{b}(2)U_{23} + \vec{b}(3)U_{33} \qquad (4.24)$$

Continue in this manner until the r's are all mutually orthogonal and of unit length. They will obey the equation

$$\vec{r}(i) \cdot \vec{r}(j) = \delta_{ij} = \begin{cases} 1 & \text{if } i = j \\ 0 & \text{if } i \neq j \end{cases} \qquad (4.25)$$

The r vectors are the columns of the matrix R

$$(\vec{r}(j))_i = R_{ij} \qquad (4.26)$$

The orthonormality statement, Eq. (4.25), is equivalent to the orthogonality statement, Eq. (4.17). The elements of the matrix U appear in Eqs. (4.20), (4.22) and (4.24) as the superposition coefficients calculated by the Gram-Schmidt process. The process determines U and R, which when substituted in Eqs (4.18) and (4.15) solve the least squares problem.

4.2.2 The modified least Squares Problem

It the minimization principle

$$\text{minimize} \quad \epsilon^2 \qquad (4.10)$$

is replaced by the modified principle

$$\text{minimize} \quad (\epsilon^2 + \tau^2 \sum_j (\frac{x_j}{q_j})^2) \qquad q_j > 0 \qquad (4.27)$$

the the optimum x_j's will be forced toward values that are small with respect to the q_j's. Parameter τ determines how strongly this occurs. As τ approaches zero the optimum x approaches the ordinary least squares solution, and as τ approaches infinity the optimum approaches zero. For an intermediate value in the neighborhood of the FERDOR value

$$\tau = \frac{\sqrt{NC}}{4} \tag{4.28}$$

There is a tendency for

$$-q_j < x_j < q_j$$

In FERDOR q_j is an estimate of the maximum value x_j could assume. It is calculated by combining the observations that: (1) the folded spectrum tends to be less than the data vector plus its root-mean-square error

$$\sum_{j=1}^{NC} A_{ij}x_j < y_i + \sigma_i \tag{4.29}$$

and (2) the folding consists of a sum of positive terms, so that any one term is less than the total

$$A_{ik}x_k < \sum_{j=1}^{NC} A_{ij}x_j \tag{4.30}$$

Therefore

$$A_{ik}x_k < y_i + \sigma_i \quad \text{for any } i, k. \tag{4.31}$$

Dividing through by A_{ik}

$$x_k < \frac{y_i + \sigma_i}{A_{ik}} \tag{4.32}$$

so that a lowest estimate of the maximum value x_k could assume is

$$q_k = \underset{\text{over } i}{\text{minimum}} \left(\frac{y_i + \sigma_i}{A_{ik}} \right) \tag{4.33}$$

It the matrix A is replaced by the matrix

$$A' = \begin{bmatrix} A & \\ \hline \tau\tau & o \\ o & \tau \end{bmatrix} \begin{matrix} NR \\ NC \end{matrix} \qquad \begin{matrix} \\ \\ NC \end{matrix} \tag{4.34}$$

the data vector y replaced by the vector

$$y' = \begin{bmatrix} y_1 \\ \vdots \\ y_{NR} \\ o \\ \vdots \\ o \end{bmatrix} \begin{matrix} NR \\ \\ \\ NC \\ \\ \end{matrix} \tag{4.35}$$

and the weight vector ω replaced by the vector

$$\omega' = \begin{bmatrix} \sigma_1^{-1} \\ \vdots \\ \sigma_{NR}^{-1} \\ q_1^{-1} \\ \vdots \\ q_{NC}^{-1} \end{bmatrix} \begin{matrix} NR \\ \\ \\ NC \\ \\ \end{matrix}$$

then the ordinary least squares principle

$$\text{minimize} \quad (\epsilon')^2$$

becomes identical to the modified principle.

4.2.3 Smoothing and Error Estimate

At the conclusion of the Gram-Schmidt process one has an inverse equation

$$x_j = \sum_{i=1}^{NR} H_{ji} y_i$$

where x, H, and y are known. However, the elements of the solution vector x have large statistical errors because the response matrix includes the resolution of the spectrometer. Hence, the solution vector is smoothed. The smoothing function is referred to as the window function. Folding the solution vector with a window function provides a smooth solution and reduces the statistical errors in the output neutron energy spectrum.

The smoothing equation used in the FERDOR method is

$$\Phi_k = \sum_{j=1}^{NC} G_{kj} x_j, \qquad k=1,\ldots,NW$$

where the smoothing matrix G is defined, so that Φ_k is the flux at energy $_kE$. Here NW is the number of energies at which the smoothed flux is calculated. In FERDOR the matrix elements of G are defined as

$$G_{kj} = (\sqrt{2\pi}\ \sigma_k)^{-1} \exp\left(-1/2\left(\frac{E_k - E'_j}{\sigma_k}\right)^2\right) \qquad (4.36)$$

where the resolution parameter σ_k is given by

$$\sigma_k = \frac{W_k\ E_k}{235.5}$$

Here W_k is read into the computer program and is called the window width at energy E_k. The window width is simply the full-width at half maximum of the Gaussian smoothing function percent. The definition of the smoothing matrix G given by Eq. (4.36), however, does not preserve normalization of the unfolded spectrum as it should if the output of the unfolding code is to be interpreted as smoothed neutron flux. Another smoothing matrix was suggested /40/,

$$G_{Kj} = (\sqrt{2\pi}\ \sigma_j)^{-1} \exp(-1/2\ (\frac{E_k - E'_j}{\sigma_j})^2) \qquad (4.37$$

where

$$\sigma_j = \frac{W_j\ E'_j}{235.5}$$

where W_j is the window width at energy E'_j. With this definition the normalization of the unfolded spectrum is preserved. This definition, however, results is more computational effort being expended in the smoothing process. When the window widths do not vary rapidly, the error which results from the use of Eq. (4.36) rather than Eq. (4.36) is small. This is due to the fact that the exponential factor in G_{kj} is small except when E_k is close to E'_j (hence, except when σ_k is almost equal to σ_j). However, when the widths do vary rapidly with energy, σ_j can be substantially different from σ_k when E_k is close to E'_j (and the exponential factor is near unity).

4.2.3 Determination of Window Widths

The suitability of a set of window widths depends upon both the shape of the neutron spectrum being measured and the statistical error of the measured spectrum. The method presented below determines an optimum set-of window functions for each spectrum unfolded /41/.

Because small changes in the window widths cause large changes in the statistical errors, the desired statistical error of the smoothed neutron spectrum has been chosen as the criterion for determining the optimum set of window widths. A simple relationship between the statistical errors obtained with two different sets of window widths is suggested by information theory /42/

$$C = \frac{\ln\left(\epsilon^{(1)}/\epsilon^{(0)}\right)}{\left(1/w^{(1)} - 1/w^{(0)}\right)} \qquad (4.38)$$

Here ϵ is one standard deviation of statistical error (the error actually includes a small non-statistical contribution, but that contribution is not significant) given in percent and W is the window width in percent. In Eq. (4.38) the statistical error, the window width, and the quantity C are all functions of energy. To determine values for C, a measured Am-Be source spectrum was unfolded using two sets of window widths. The quantity C was calculated using the two sets of windo widths and the resulting errors in the smoothed neutron spectrum. A simple empirical expression for C which fit the data reasonably well (within 25%) was, for the 2"x2" NE-213 detector

$$C_k = 40\ \exp(-0.08\ E_k) + 50\ \exp(-0.7\ E_k,\ k=1,\ldots,NW \qquad (4.39)$$

and that for the 2"x5" NE-213 detector

$$C_k = 107.8 - 44\ E_K + 8.5\ E_K^2 - 0.656\ E_K^3 + 0.0174\ E_K^4 \qquad (4.40)$$

where E_k is the neutron energy in MeV.

These empirical realationships between the errors and the window widths are used in a modified version of FERDOR in an iterative procedure. The computer program performs the unfolding process (zeroth iteration) using the sample set of window width $W^{(0)}$. The statistical errors $\varepsilon^{(0)}$ are thus obtained. The user supplies the desired statistical errors, ε. Then, a new set of window widths, $W^{(1)}$, are calculated. For the 2"x2" NE-213 detector the new set of window widths are

$$W_k^{(n)} = \frac{1}{W_k^{(n-1)}} + \frac{\ln\left(\varepsilon_k/\varepsilon_k^{(n-1)}\right)}{40\exp(-0.08\ E_k) + 50\exp(-0.7\ E_k)} \qquad 4.41$$

$k = 1,\ldots,NW$

and those for the 2"x5" NE-213 detector are

$$W_k^{(n)} = \frac{1}{W_k^{(n-1)}} + \frac{\ln\left(\varepsilon_k/\varepsilon_k^{(n-1)}\right)}{107.8-44E_k+8.5E_k^2-0.656E_k^3+0.0174E_k^4}$$

$k = 1,\ldots,NW.$

The new set of window widths is then used in Eq. (4.36) to repeat the smoothing process and to calculate the new set of statistical errors (first iteration). Equations (4.41) are used to calculate the n^{th} set of window widths with the constraint that they are < 1.5 times the sample set of window widths. One or two iterations have been found to suffice in all cases studied so far.

The empirical functions used in the iterative smoothing technique and the experimental values for C for both detectors are shown in Figs. (4.1) and (4.2). The modified version of FERDOR was used in unfolding all neutron spectra measured for the current research.

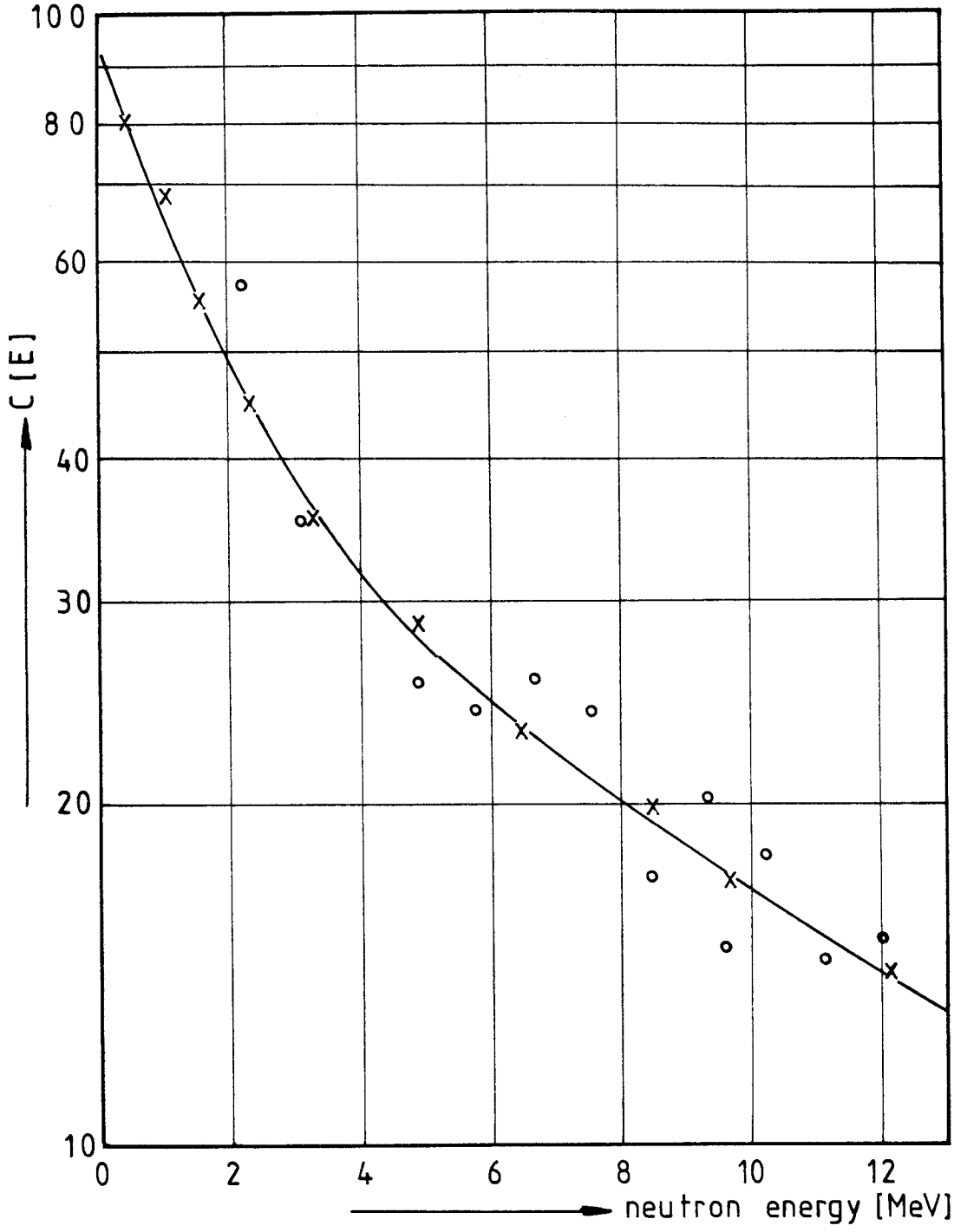

Fig. 4.1: Empirical function used in iterative smoothing technique for the 2"x2" NE-213 detector. The open circles are data points obtained from an Am-Be neutron spectrum measurement smoothed with two different sets of window widths. The solid line represents Eq. (4.39)

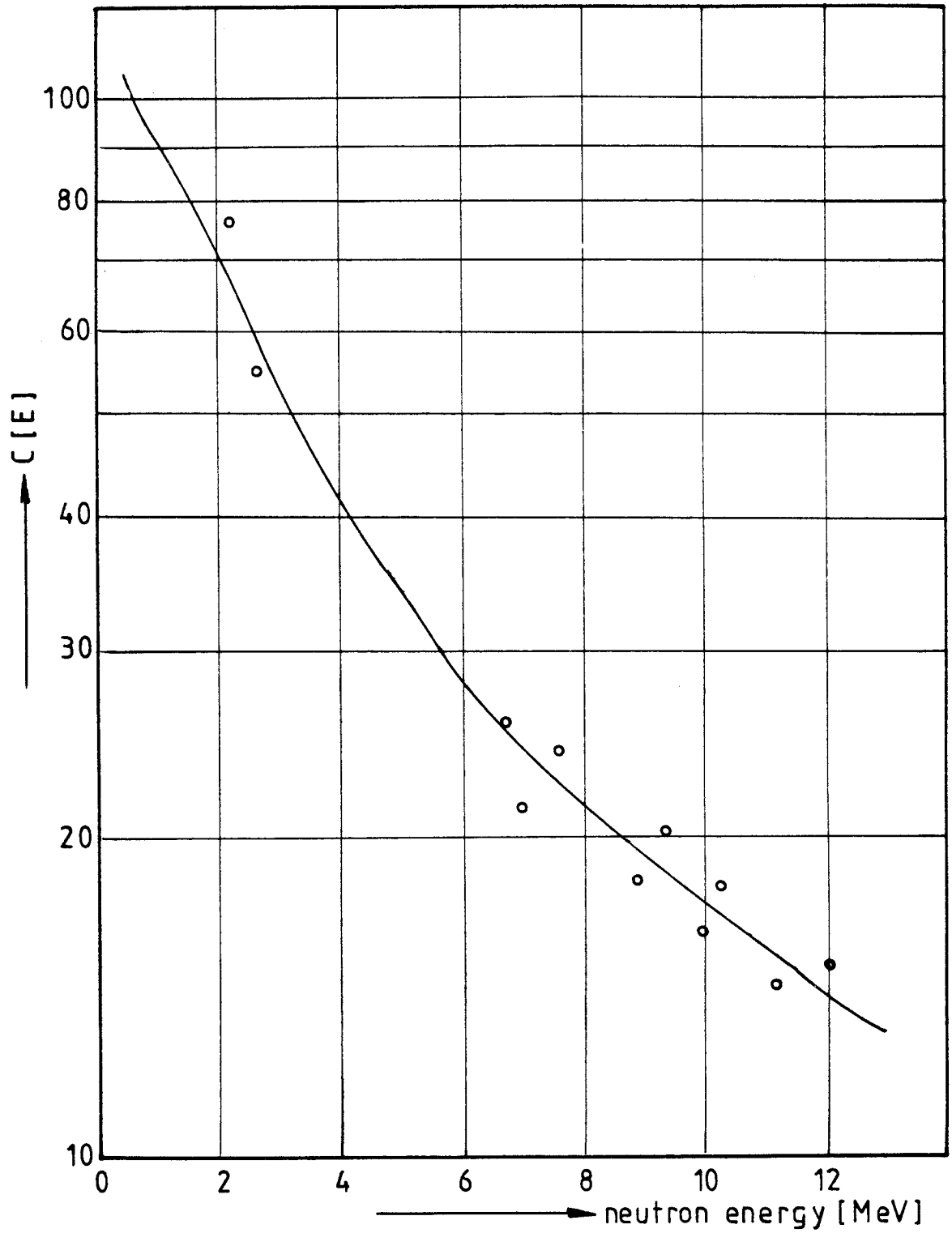

Fig. 4.2: Empirical function used in interative smoothing technique for the 2"x5" NE-213 scintillator. The open circles are data points obtained from an Am-Be neutron spectrum measurement smoothed with two different sets of window widths. The solid line represents Eq. (4.40)

5. TESTS OF THE NE-213 SPECTROMETRY SYSTEM

5.1 241-Americium-Beryllium Neutron Spectrum

The mechanism of neutron emission in an Am-Be-source is well understood. The 5.48 MeV alpha particles emitted by ^{241}Am slow down in AmO_2-Be mixture and interact with the ^{9}Be via the $^{9}Be(\alpha,n)^{12}C$ reaction

$$^{9}Be + \alpha \longrightarrow {}^{12}C + n + 5.71 \text{ MeV}.$$

The pulse height distributions measured for the Am-Be neutron source were unfolded using the modified version of FERDOR with the desired statistical error set at +3%. The zeroth iteration neutron spectrum shown in Fig. (5.1) measured with the 2"x2" NE-213 detector was obtained using a logarithmically divided window widths. The first iteration spectrum shown in Fig. (5.2) shows noticeable improvements over the spectrum shown in Fig. (5.1). In Fig. (5.2) statistical error in the 9.5 shoulder has been reduced, and the 6.8 MeV peak has been better resolved. The logarithmic set of window widths and the window widths obtained in the first iteration of modified FERDOR are shown in Fig. (5.3). It can be seen from Fig. (5.3) that the improvements in the Am-Be spectrum were obtained by increasing the window width below 3 MeV and by decreasing the window widths between 3 and 11,5 MeV. The first iteration neutron spectrum measured with the 2"x5" NE-213 detector is shown in Fig. (5.4). It is noticeable that the peaks are better resolved by the smaller detector rather than the larger.

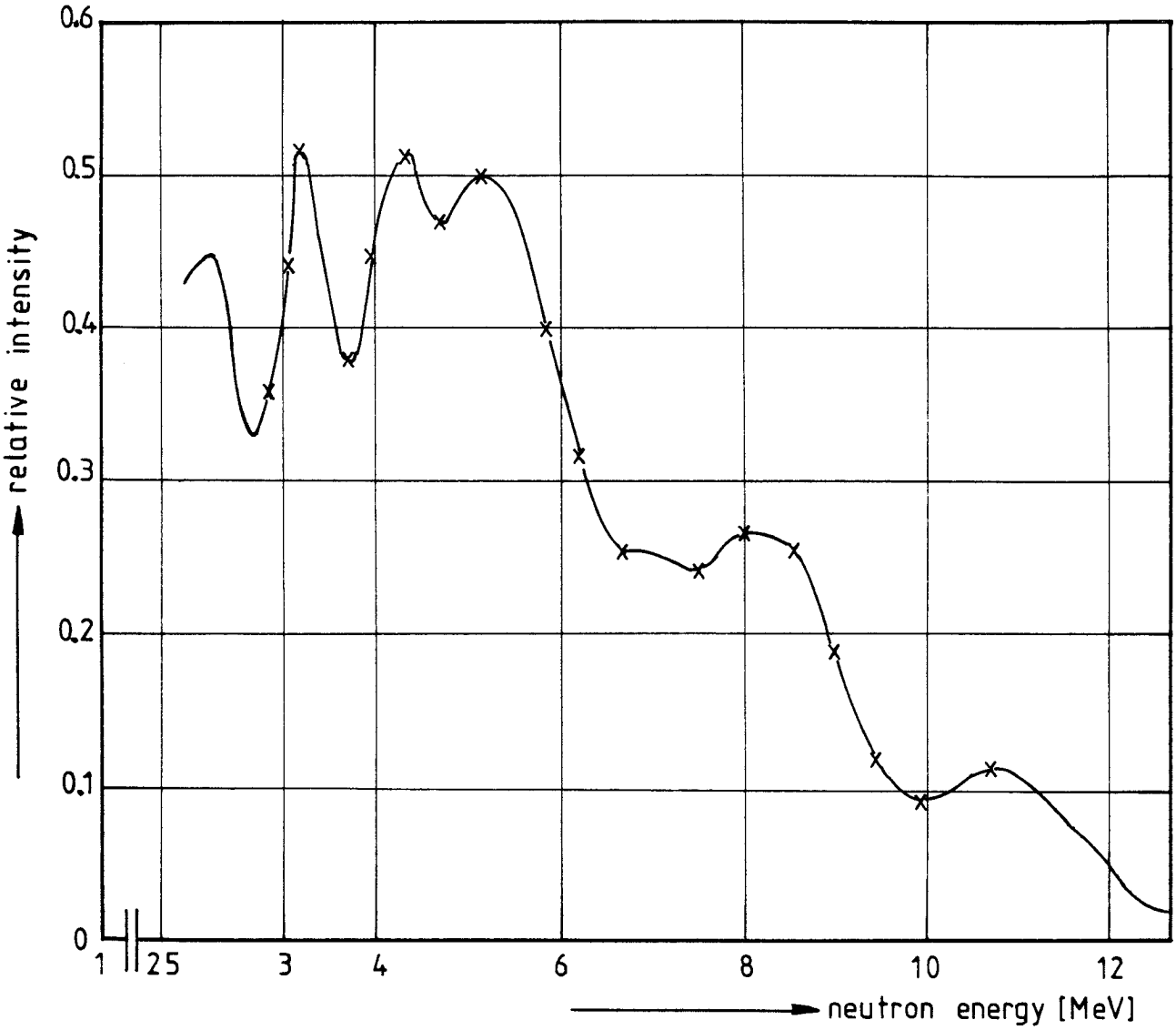

Fig. 5.1: Zeroth iteration neutron spectrum of Am-Be neutron source with the 2"x2" NE-213 detector

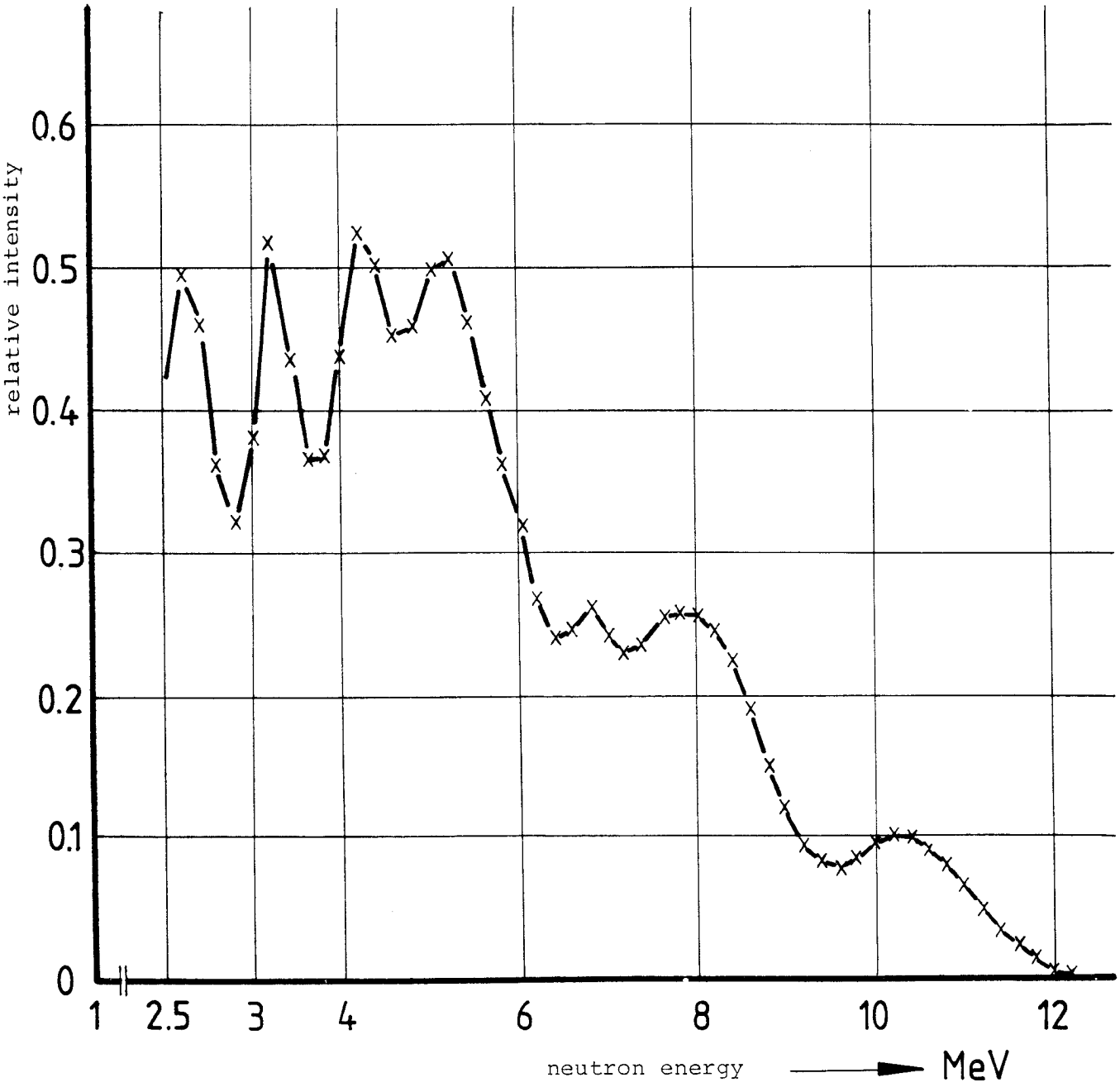

Fig. 5.2: First iteration neutron spectrum of Am-Be neutron source with the 2"x2" NE-213 detector

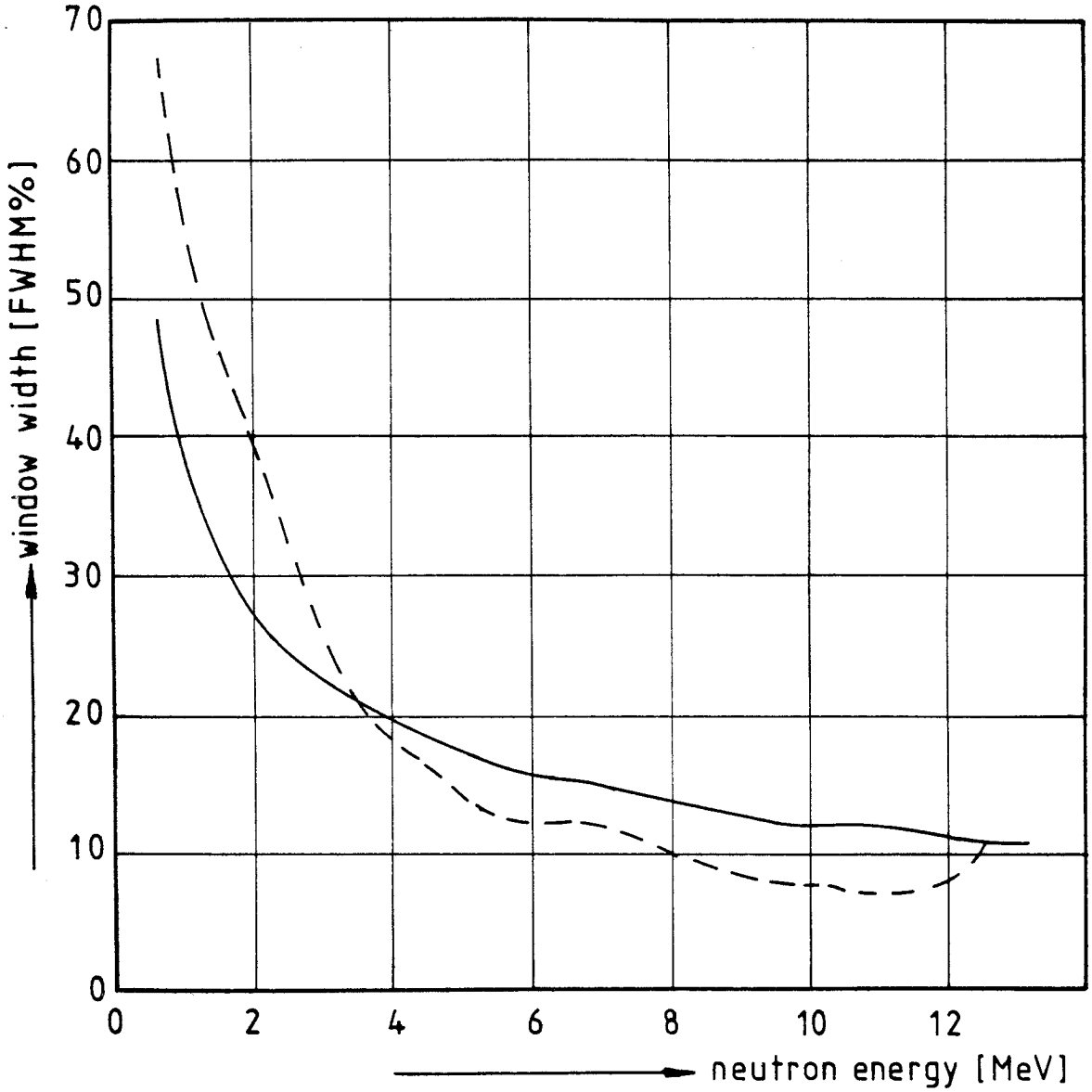

Fig. 5.3: Window widths used in modified FERDOR. The solid line is the logarithmic window widths. These were used in the zeroth iteration. The dashed line is the first iteration of window widths for the Am-Be neutron spectrum with the 2"x2" NE-213 detector

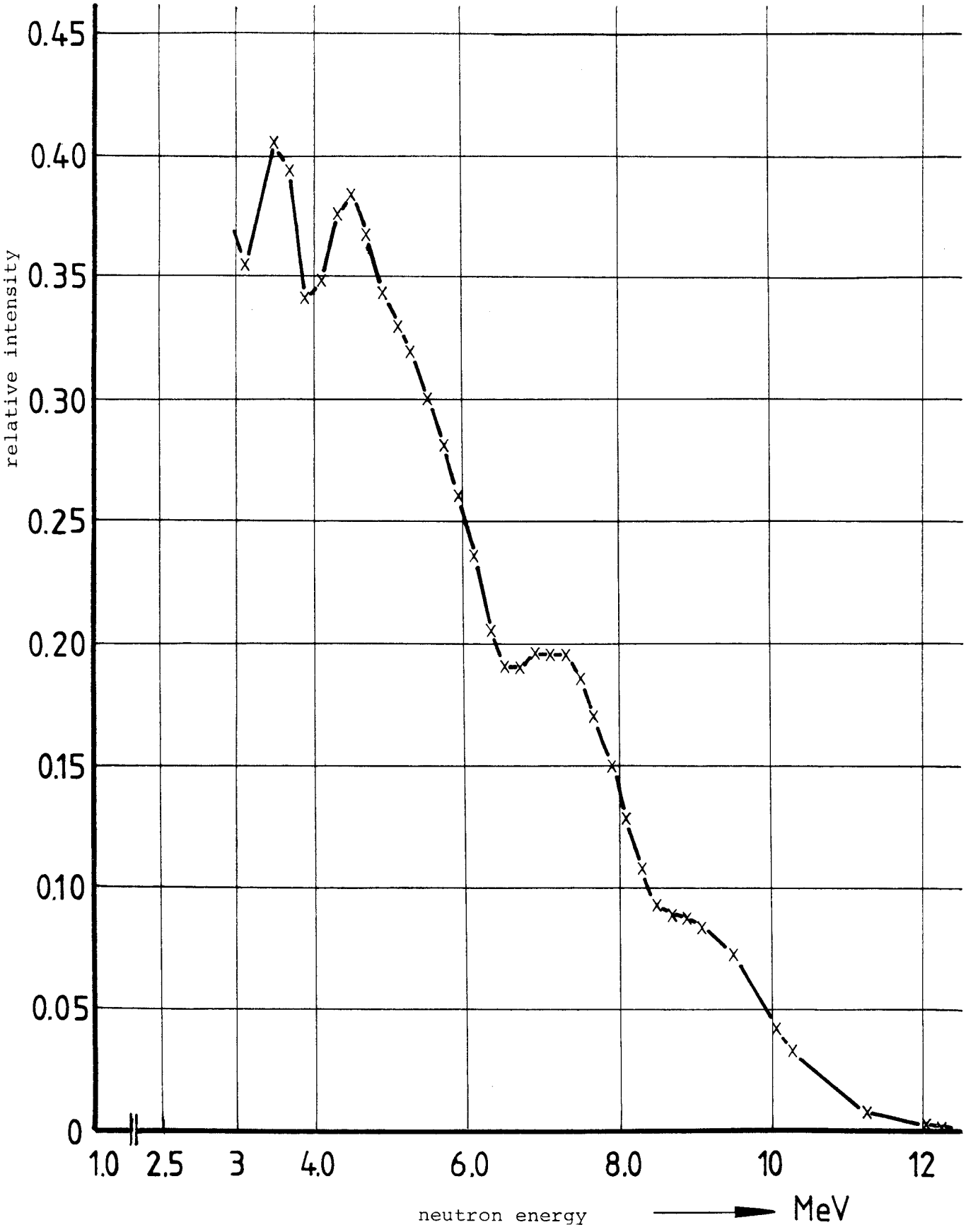

Fig. 5.4: The first iteration neutron spectrum of Am-Be neutron source with the 2"x5" NE-213 scintillator

These unfolded Am-Be spectra are in good agreement with similar recent measurements /43-45/. Peaks are observed at approximately 3.3, 4.3, 5.1, 6.8, 7.8 MeV and a shoulder at 9.5 MeV. All this detail is well established, although slight variations in the energies and the intensity of the peaks are quoted. It is well known that the spectral features are dependent on the source construction and especially on the particulate size of the AmO_2 and Be powder /46/, as this will strongly influence the distribution of alpha particle energies. In particular, the relative intensity of the various neutron groups present in the spectrum depends on this energy distribution.

5.2 252-Californium Neutron Spectrum

The unfolded ^{252}Cf fast neutron spectrum measured with the 2"x5" NE-213 scintillator is illustrated in Fig. (5.5). Although overall agreement between the published spectra /47/ and our measurements is good, some oscillations exist in the FERDOR spectrum around 2.5 and 3.5 MeV.

5.3 D-T Neutron Spectrum

The pulse height distributions for a D-T neutron source measured with both NE-213 scintillators were unfolded using the modified version of FERDOR. The desired statistical error was 3%. The zeroth iteration spectra are shown in Figs. (5.6) and (5.7) for the 2"x2" and 2"x5" scintillators respectively. The first iteration spectra are shown in Figs. (5.8) and (5.9) for both detectors. The sample set of window widths (zeroth iteration) is shown in Fig. (5.10) as the solid line, the first iteration set of window widths is shown as the dased curve. When such a monoenergetic neutron source is measured and unfolded with FERDOR, a peak is obtained, but the shape of the response

function of NE-213 causes the low-energy side of the peak to have significantly higher statistical error than the high-energy side of the peak. Unfolding the same monoenergetic neutorn source with the modified version of FERDOR results in a neutron peak with low- and high-energy sides having comparable statistical errors. This is accomplished by iterating to obtain and use noticeably larger window widths on the low-energy side of the peak than on the high-energy side, thus producing structure in the window widths. Such structure is seen in the first iteration set of window widths for the D-T source measurements. This iterative smoothing technique helped to optimize the resolution of the unfolded spectra especially for the smaller scintillator.

Oscillations in the flux at lower energies in the unfolded spectra are very noticeable. These oscillations could be caused either by deficiencies in the FERDOR unfolding method or by inaccuracies in the response matrix. The cause of these oscillations was investigated for the 2"x5" scintillator by unfolding column 57 of the response matrix using the modified version of FERDOR. This column is the pulse height spectrum corresponding to the response function for a unit source of 13.90 MeV neutrons. The column was assumed to have a statistical error of 19 The desired statistical error of the unfolded neutron spectrum was 3%. The zeroth iteration unfolded "spectrum" is shown in Fig. (5.11). The first iteration unfolded "spectrum" is shown in Fig. (5.12). Neither the zeroth iteration nor the first iteration unfolded "spectra" have oscillations below the peak energy. These facts indicate that the oscillations observed in measurements of monoenergetic spectra are due to inaccuracies in the response matrix and are not due to deficiencies in the FERDOR unfolding method.

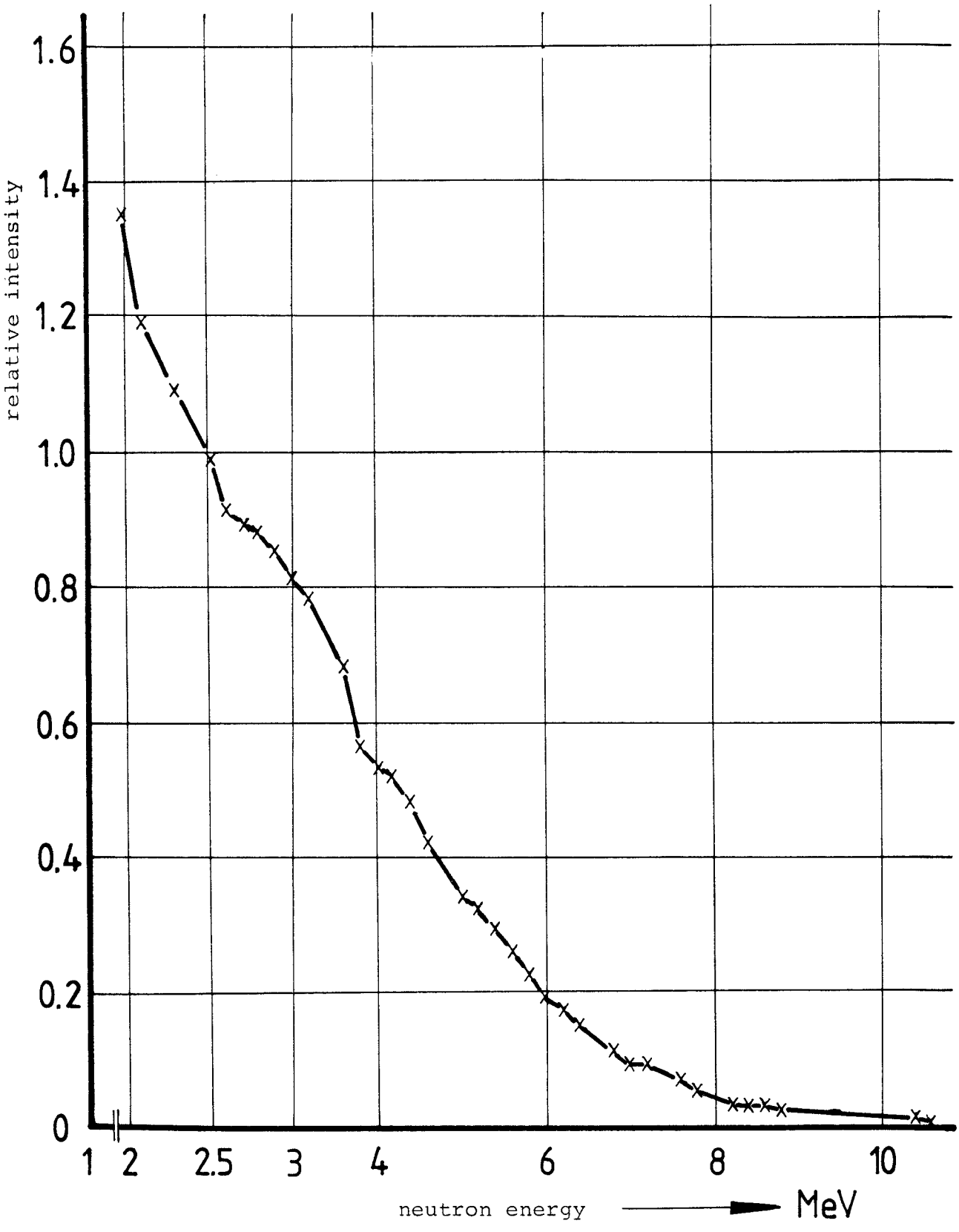

Fig. 5.5: The unfolded ^{252}Cf neutron spectrum measured with the 2"x5" NE-213 scintillator

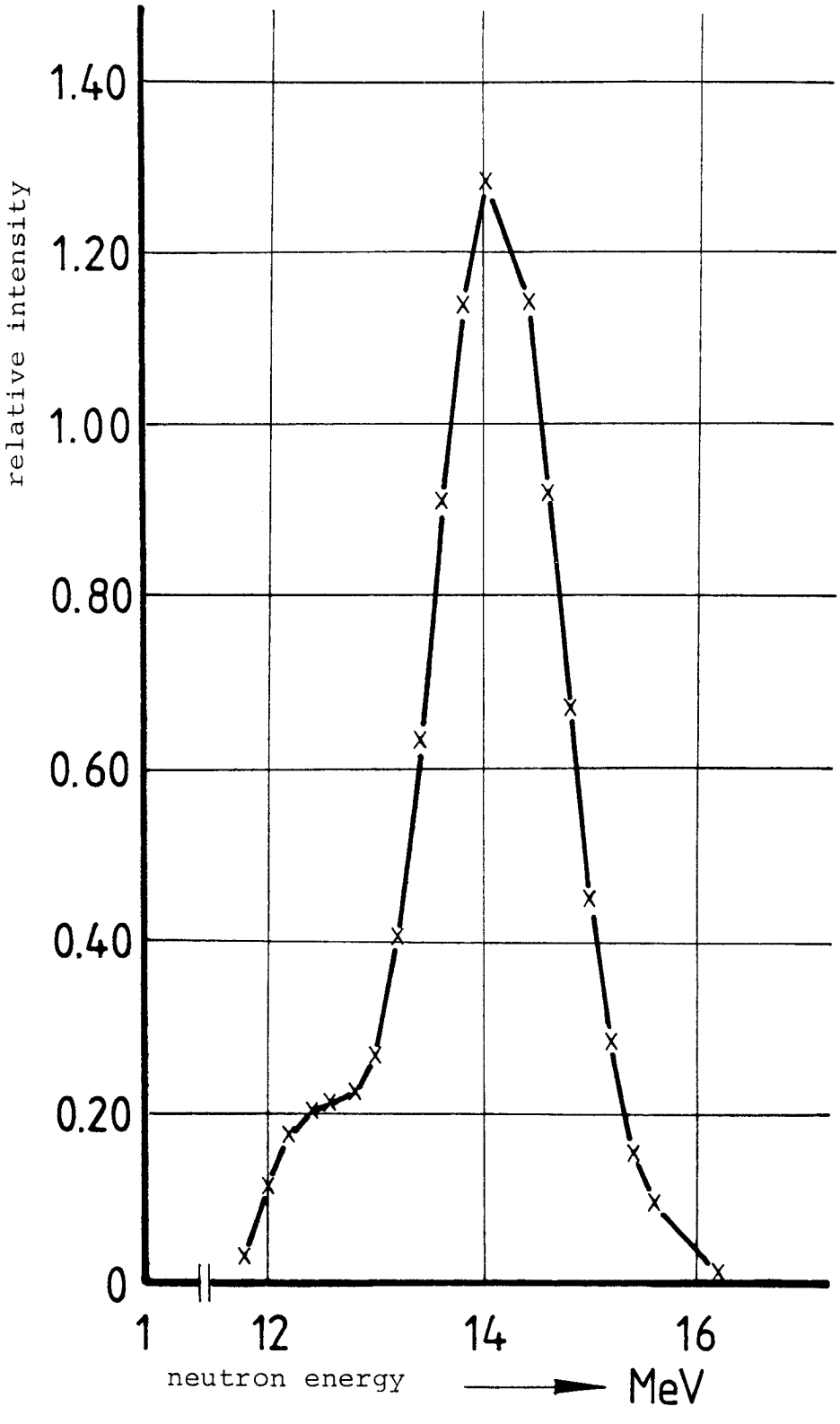

Fig. 5.6: Zeroth iteration neutron spectrum of 14 MeV neutrons with the 2"x2" NE.213 detector

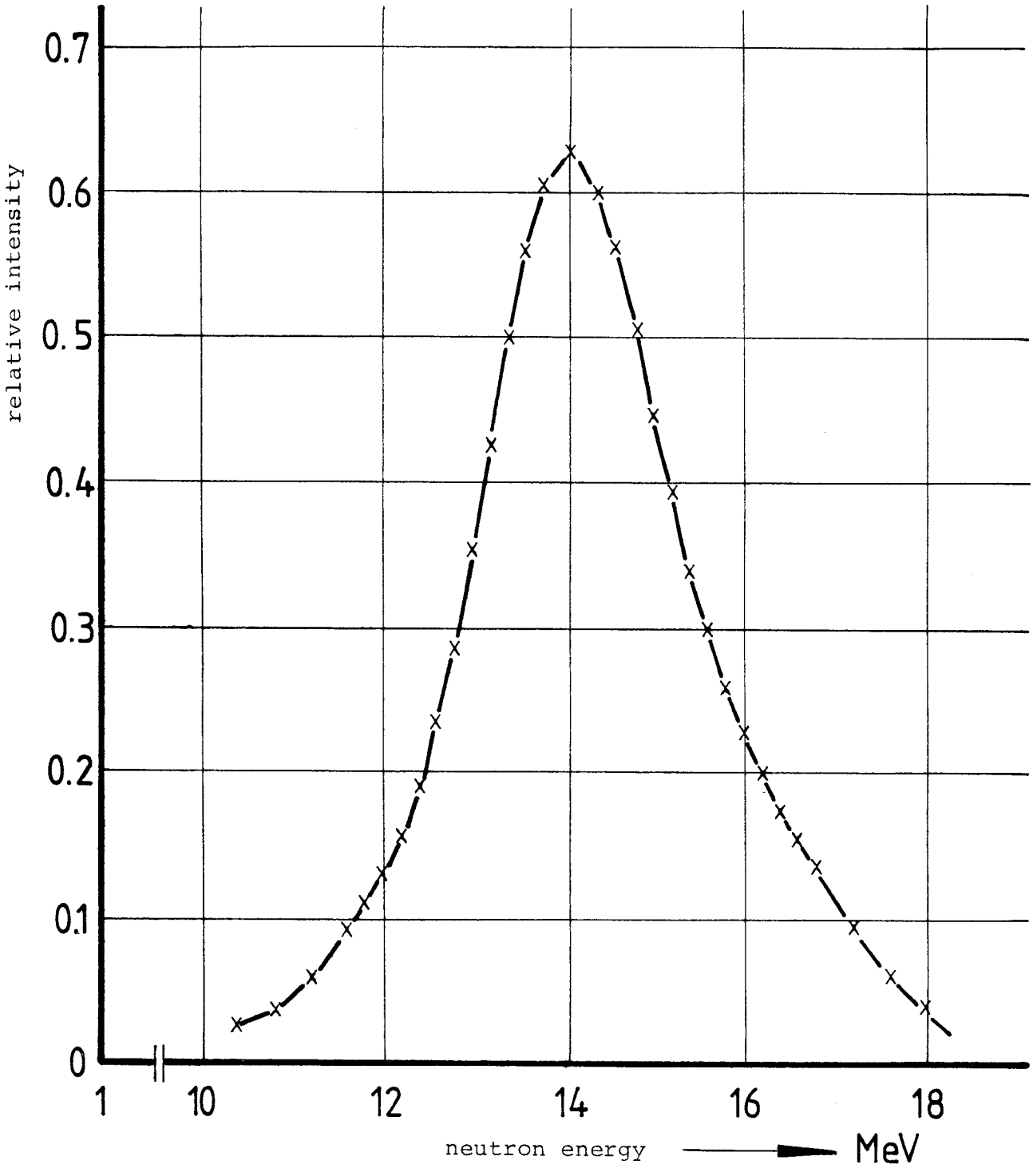

Fig. 5.7: Zeroth iteration neutron spectrum of 14 MeV neutrons with the 2"x5" NE-213 detector

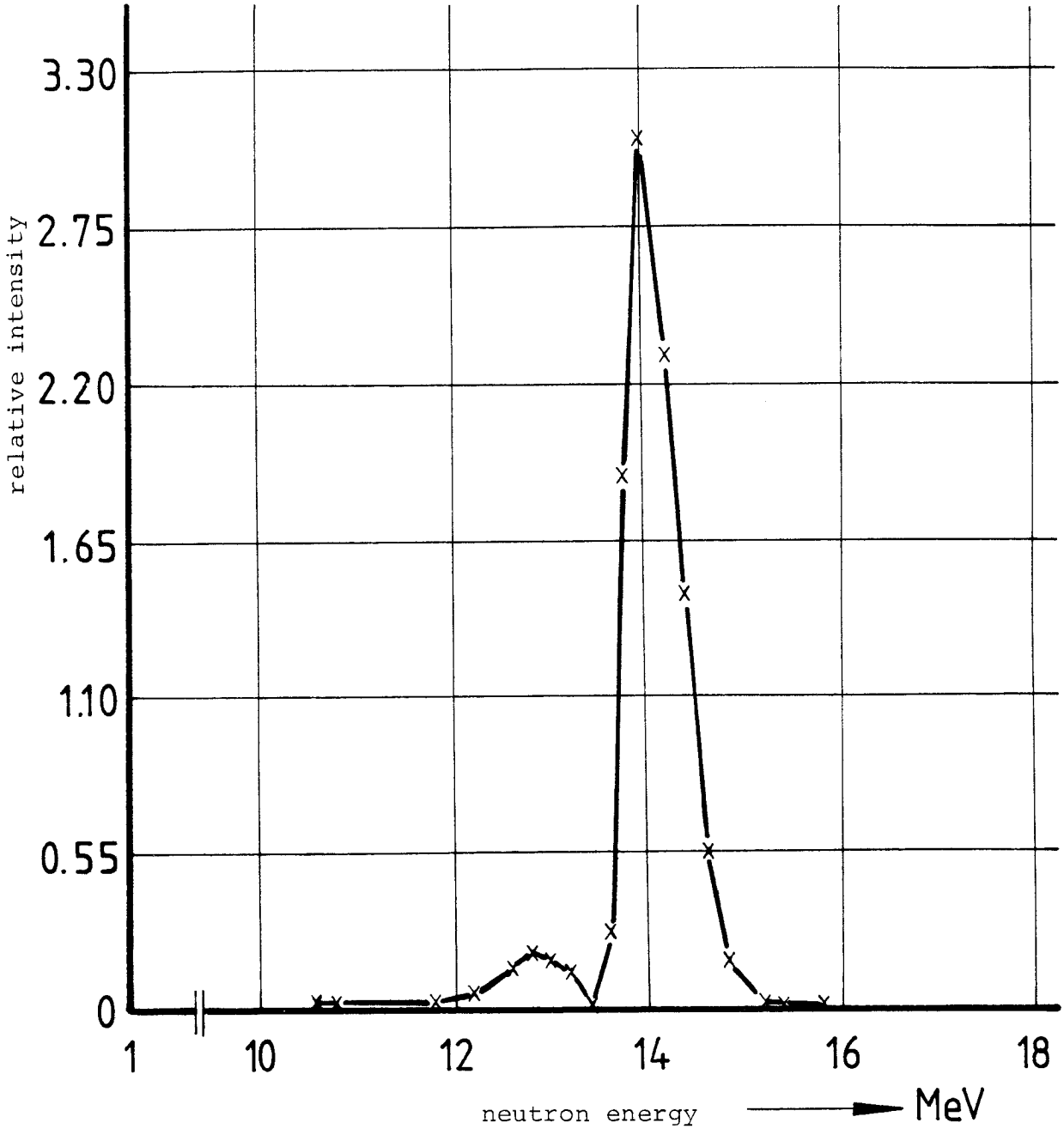

Fig. 5.8: First iteration neutron spectrum of 14 MeV neutrons with the 2"x2" NE-213 detector

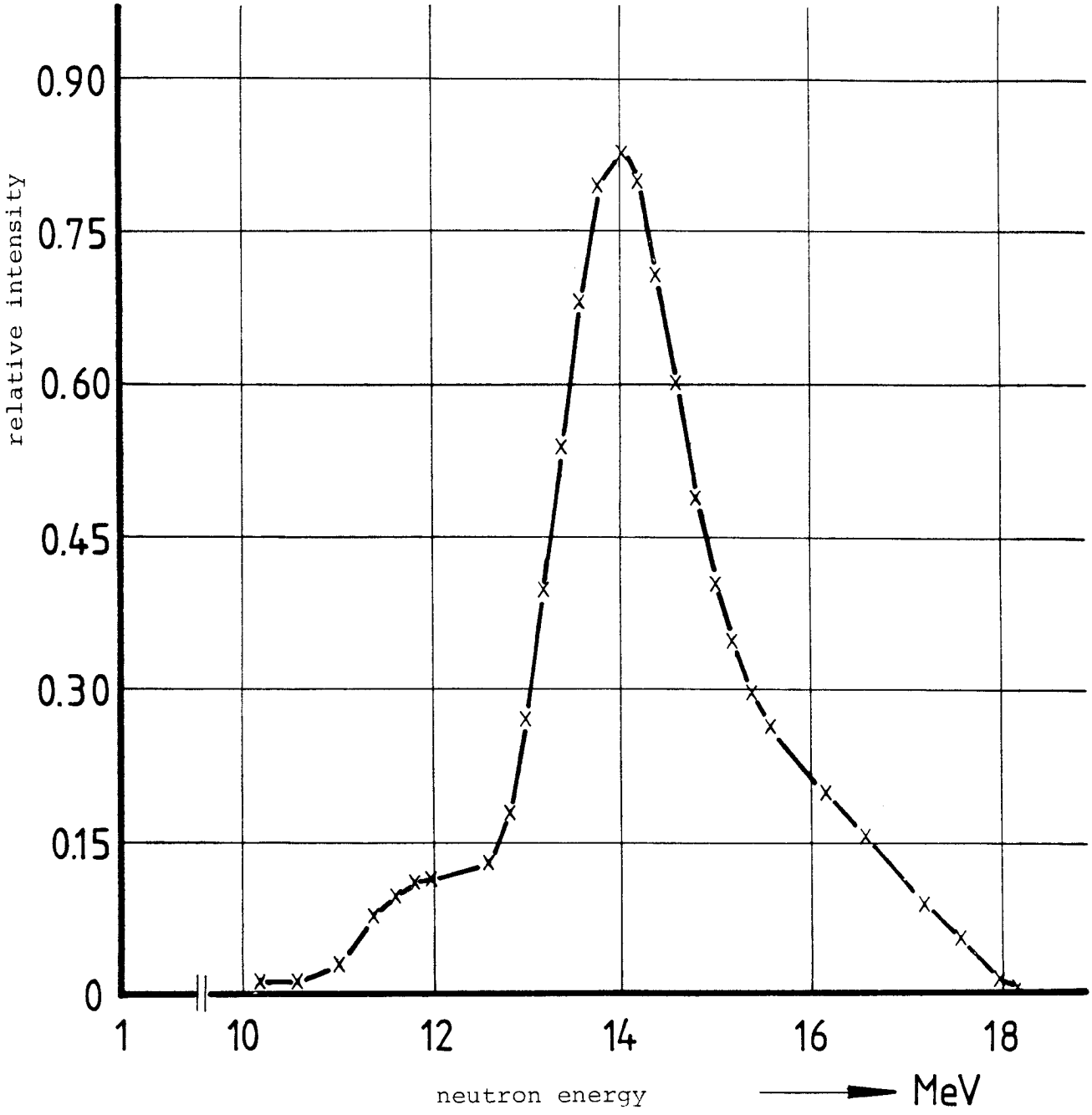

Fig. 5.9: First iteration neutron spectrum of the 14 MeV neutrons with the 2"x5" NE-213 detector

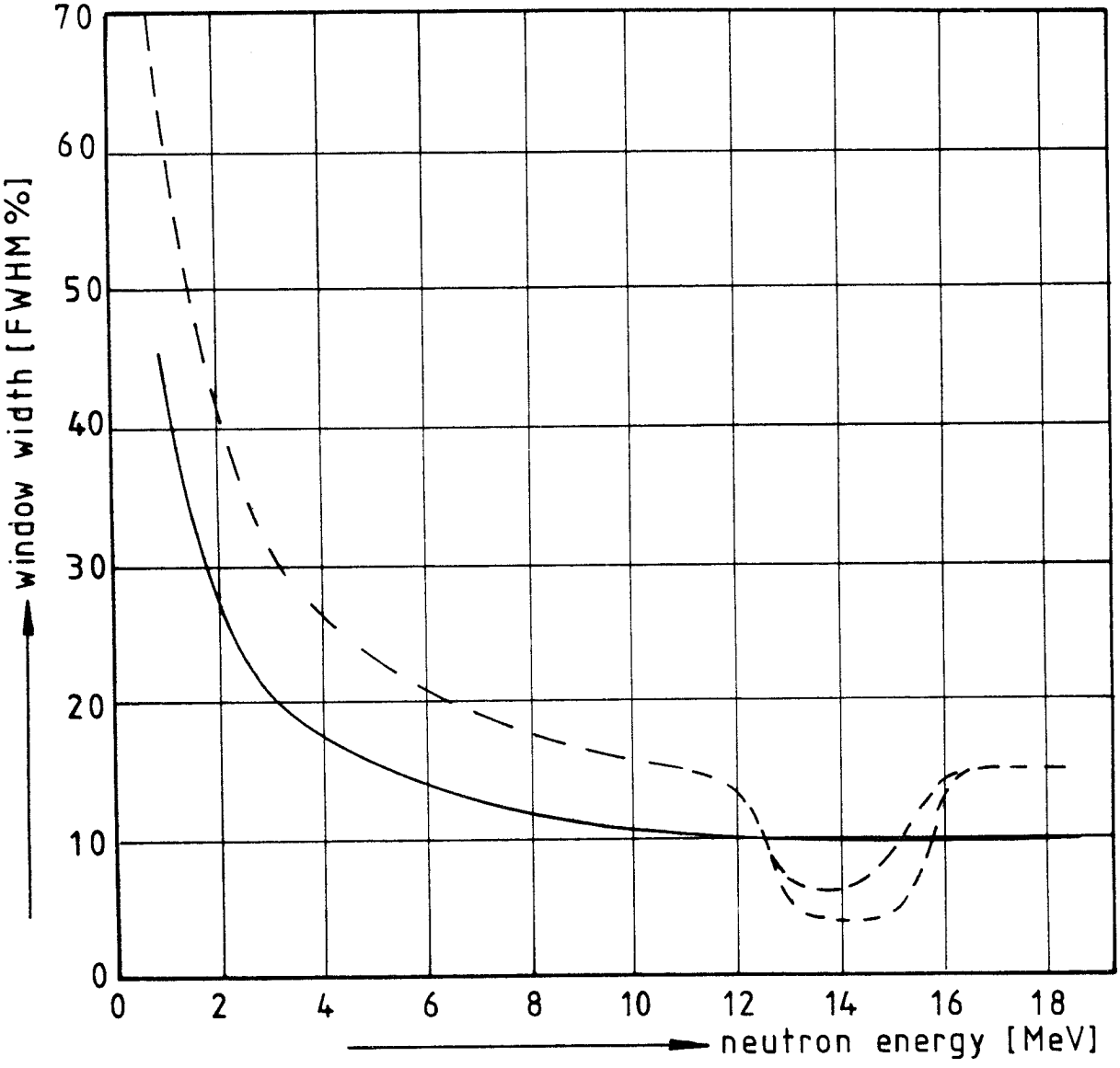

Fig. 5.10: Window widths used in modified FERDOR. The solid line is the zeroth iteration set of window widths, while the dashed one is the first iteration window widths

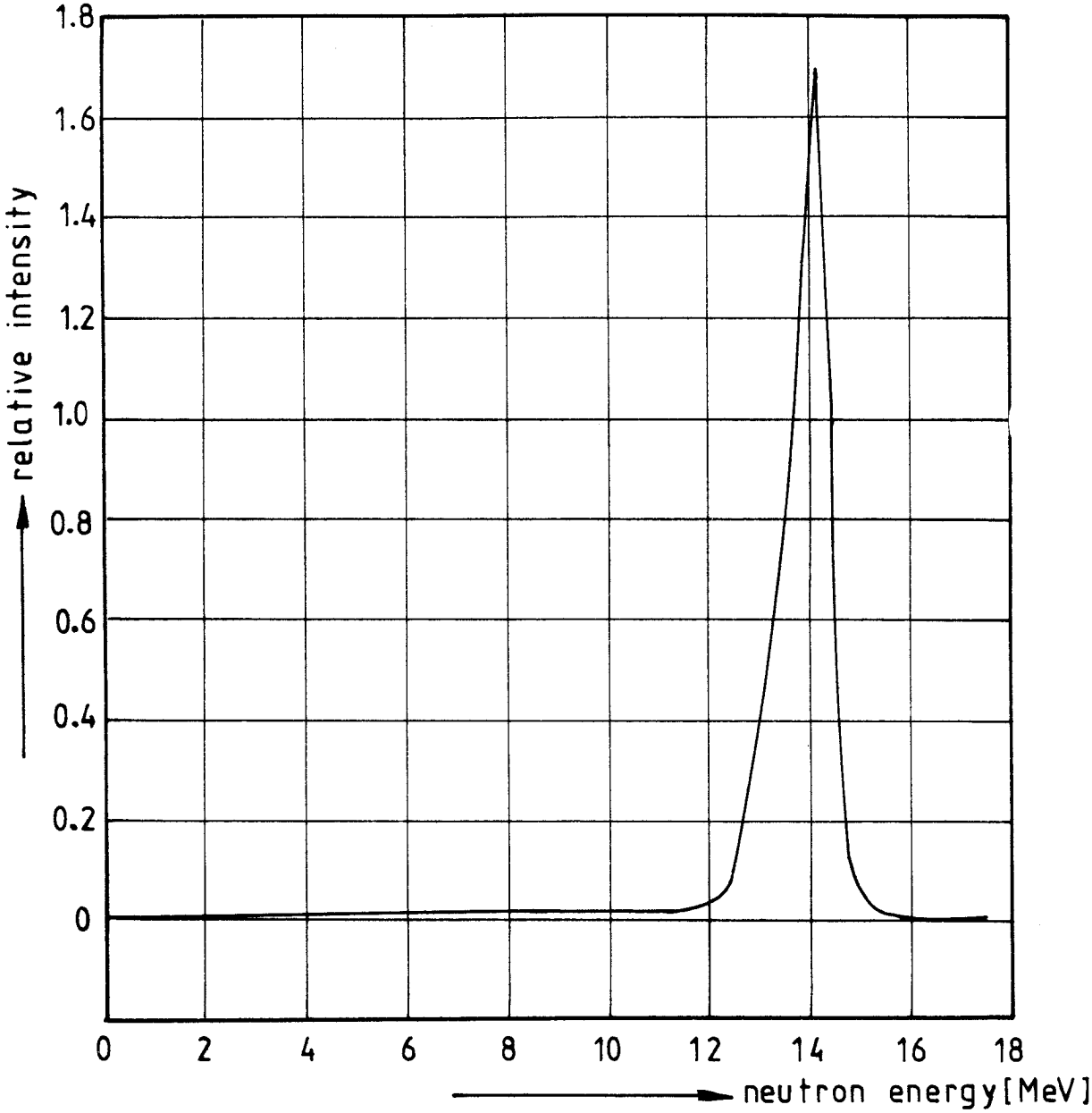

Fig. 5.11: Zeroth iteration neutron "spectrum" for column 57 of the response matrix of 2"x5" NE-213 scintillator

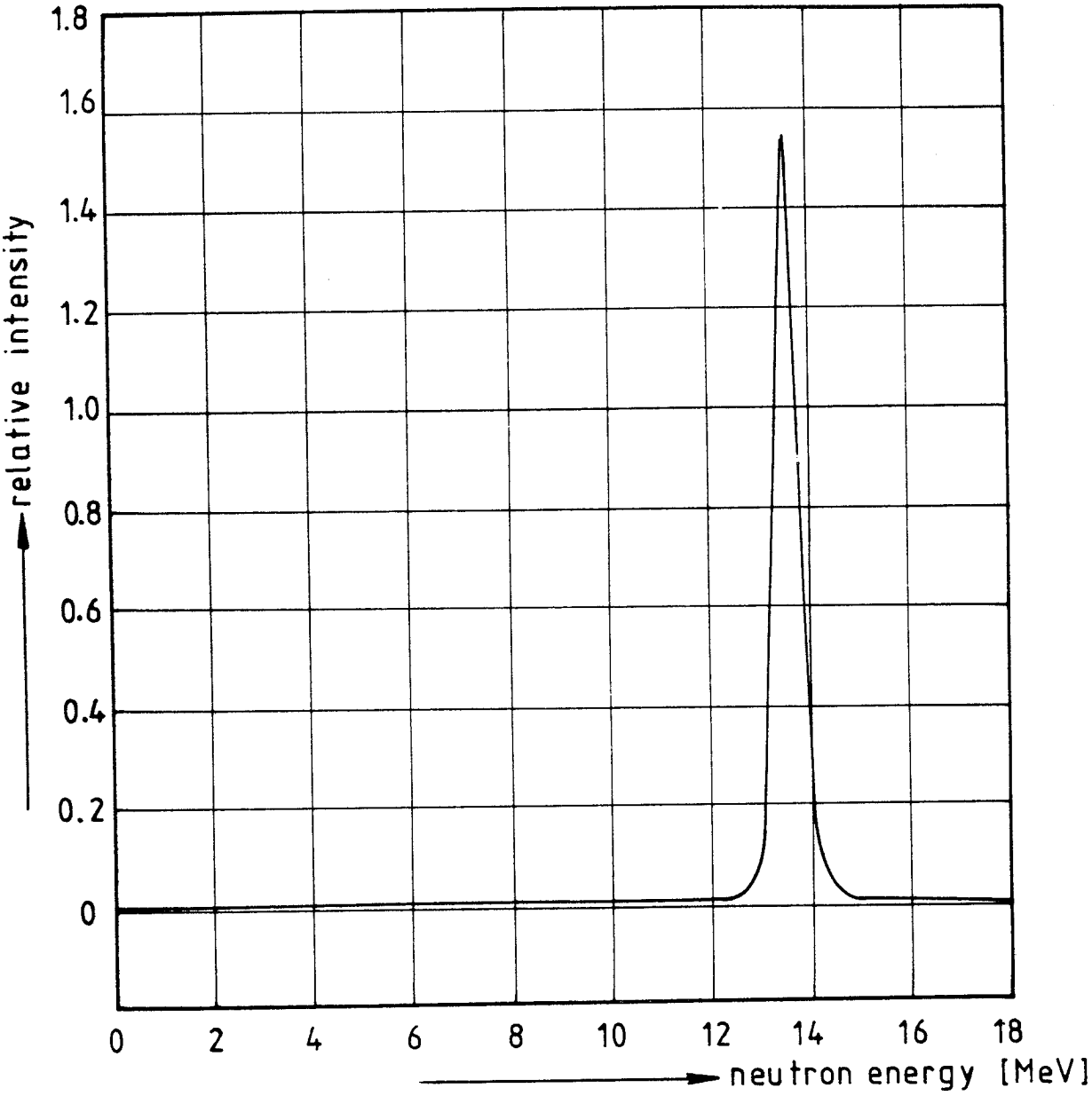

Fig. 5.12: First iteration neutron "spectrum" for column 57 of the response matrix of 2"x5" NE-213 detector

5.4 D-D Neutron Spectrum

The pulse height distributions for a D-D neutron source measured with both NE-213 detectors, 2"x2" and 2"x5" were unfolded using the modified version of FERDOR. The desired statistical error was +3%. The zeroth iteration spectra are shown in Figs. (5.13) and (5.14). In Figs. (5.15) and (5.16) the first iteration spectra are are illustrated. The window widths for both zeroth and first iterations are shown in Fig. (5.17). The structure of the first iteration window widths is similarly interpretated as that of the D-T neutron spectrum shown in Fig. (5.10). This structure results in a neutron peak with low- and henergy sides having comparable statistical errors and the optimization of the peak resolution.

The oscillations in the flux at lower energies (lower than 2.5 MeV) in the unfolded flux are investigated in the same manner as in D-T spectrum by unfolding column 10 of the response matrix of 2"x2" scintillator using the modified version of FERDOR where no oscillations are resulted in the unfolded "flux". So these oscillations are again due to uncertainties in the calculations of the response matrices of both detectors.

5.5 Comparison Between the Two NE-213 Detectors

In choosing a size for a recoil proton scintillator, several compromises must be struck depending on the purpose for which it will be applied. The first involves a trade off of counting efficiency versus energy resolution. These are the two important factors, efficiency and energy resolution, taken in consideration when the recoil proton scintillator is used for fusion plasma diagnostic. By making the scintillator thick, the efficiency is obviously enhanced. For example, in the thick scintillator (2"x5", i.e. 12.7 cm thick) interaction probabilities

of at least 50 percent will hold for neutrons whose energy is less than 2 or 3 MeV. As the neutron energy increases, the detection efficiency will decrease, and consequently there will be strong motivation to make the scintillator large. In Figs. (3.2) and (3.3) the calculated efficiency for both the small (2"x2") and the large (2"x5") detectors are shown, where the efficiency advantage of the larger detector over the smaller one is obviously. However, it is more difficult to achieve uniform light collection from a large volume scintillator, and the energy resolution will worsen. A comparison of the energy resolution of the two detectors is presented in Figs. (5.8) and (5.9) for D-T neutrons and in Figs. (5.15) and (5.16) for D-D neutrons. The resolution of the 2"x2" NE-213 spectrometer is 3 percent at neutron energy 14 MeV and 5 percent at 2.5 MeV. The resolution of the 2"x5" Ne-213 spectrometer is 6 percent at neutron energy 14 MeV and 10 percent at 2.5 MeV. A significant better resolution is indicated for the smaller scintillator. Although more data are desirable, the two-point comparison indicates a difference in resolution as a function of energy for the two spectrometers.

Another factor that often limits scintillator size is the pulse rate due to gamma rays interacting within the detector. In many applications, this rate exceeds that from fast neutrons, and the scintillator must be kept sufficiently small so that the pile-up of gamma ray events is not a problem.

In small scintillators, a typical neutron is likely to scatter only once, and the energy spectrum of proton recoils will closely approximate the rectangular distribution. As long as the scintillator dimensions are larger than a few millimeters, escape of protons from the surface is unlikely, and the response function of the detector is simple and easily calculated. As the detector dimensions are increased, multiple scattering of the neutrons becomes more likely and the response function

is more complicated and harder to predict. Because an accurate knowledge of the response function is critical for the unfolding process, one would like to keep the scintillator small so that these complicating effects do not introduce large uncertainties.

Another factor that affect the energy resolution of the scintillator detector is the light collection condition. In any scintillation detector, one would like to collect the largest possible fraction of the light-emitted isotropically from the track of the ionizing particle. Two effects arise in practical cases which lead to less than perfect light collection: optical self-absorption within the scintillator and losses at the scintillator surfaces /48/.

The light collection conditions affect the energy resolution of a scintillator in two distinct ways. Firstly, the statistical broadening of the response function will worsen as the number of scintillation photons which contribute to the measured pulse is reduced. The best resolution can therefore be achieved only by collecting the maximum possible fraction of a photons emitted in the scintillation event. Secondly, the uniformity of the light collection will determine the variation in signal pulse amplitude as the position of the radiation interaction is varied throughout the scintillator. Perfect uniformity would assure that all events which deposit the same energy, regardless of where they occur in the scintillator, would give rise to the same mean pulse amplitude.

The phenomena can interpret the difference in resolution between the two detectors. With the small detector, uniformity of light collection is seldom a significant contributor to the overall energy resolution. In the thicker detector, variations in light collection efficiency can dominate the energy resolution.

It must be noted that the energy resolution of these detectors are measured taking in consideration the effect of the sources of random noise within the instrumentation system (electronic noise). There are another potential sources of fluctuations in the response of these detectors which result in imperfect energy resolution. Among these is the statistical noise arising from the discrete nature of the measured signal itself. This arises from the fact that the charge Q generated within the detector by a quantum of radiation is not a continuous variable but instead represents a discrete number of charge carriers (in the scintillation detector they are the number of electrons collected from the photocathode of the photomultiplier tube). The number of carriers is discrete and subject to random fluctuation from event to event even though exactly the same amount of energy is deposited in the detector. A limiting resolution, R, due only to statistical fluctuations in the number of charge carriers is calculated as /48/

$$R = 2.35(N)^{-1/2}$$

where N is the total number of charge carriers generated in the detector on the average. In the case of liquid scintillators there are so many charge carriers generated per event that this limiting resolution is so small compared to the measured resolution.
In the measurements of the monoenergetic neutron sources with the neutron generator arises another source of fluctuation in the response of the detectors. Since the target has a finite thickness, deutrons of all energies from the bombarding energy (300 keV) to their energy at the point they leave the active area of the target will yield neutrons. The shape of the neutron spectrum will be a function of the energy loss of deutrons in the target. This energy loss was calculated /56/ to be 109 keV. Assuming that this energy loss has the same distribution as that of the bombarding energy, i.e. Gaussian-Quadratic distribution. Then this will give 30 keV fluctuation to the measured neutron spectrum. If each source of fluctuation is independent, then the over all or the measured energy resolution is

$$\Delta E^2 = \Delta E^2_{\text{statistical}} + \Delta E^2_{\text{noise}} + \Delta E^2_{\text{energy loss in target}} + \Delta E^2_{\text{detector}} + \cdots$$

Each term on the right-hand side is the square of the subtitle source of fluctuation.

According to the previous discussion and calculation of the different sources of fluctuations, the resolution of the detectors must be corrected as follows. The resolution of the 2"x2" NE-213 spectrometer is 2.7 percent at neutron energy 14 MeV and 3.8 percent at 2.5 MeV. The resolution of the 2"x5" NE-213 spectrometer is 5.7 percent at neutron energy 14 MeV and 8.8 percent at 2.5 MeV.

Considering the different values of energy resolutions one must also think about the finite angle subtended by the detector and scattering of the primary source neutrons by target and detector assemblies or by the wall and structure of the beam room, especially for the 14 MeV neutrons. One must not forget the effect of the uncertainties in the response matrices of the detectors and those in the unfolding system, which affect also the energy resolution, but cannot be precisely calculated.

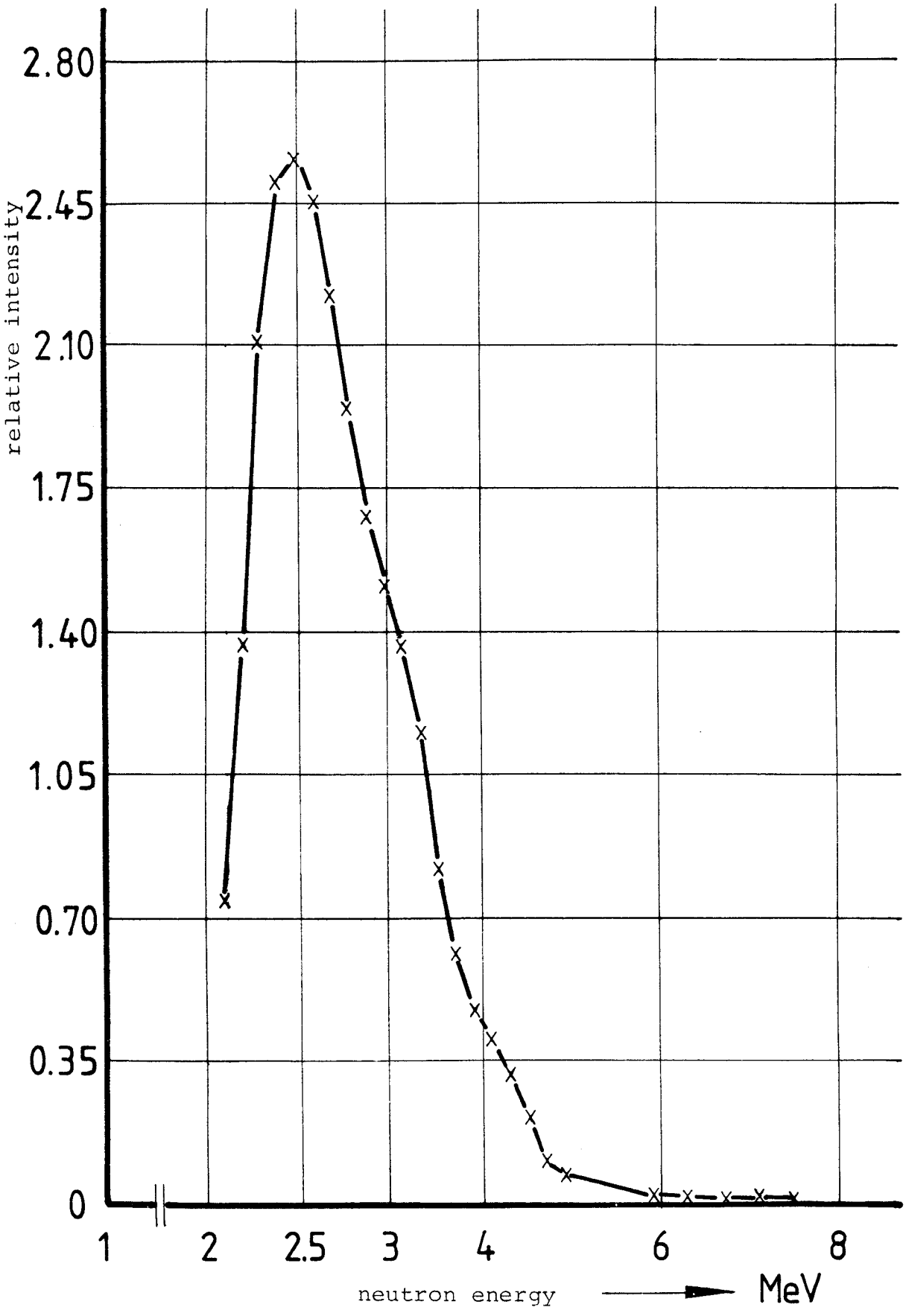

Fig. 5.13: Zeroth iteration neutron spectrum of D-D neutrons with the 2"x2" NE-213 scintillator

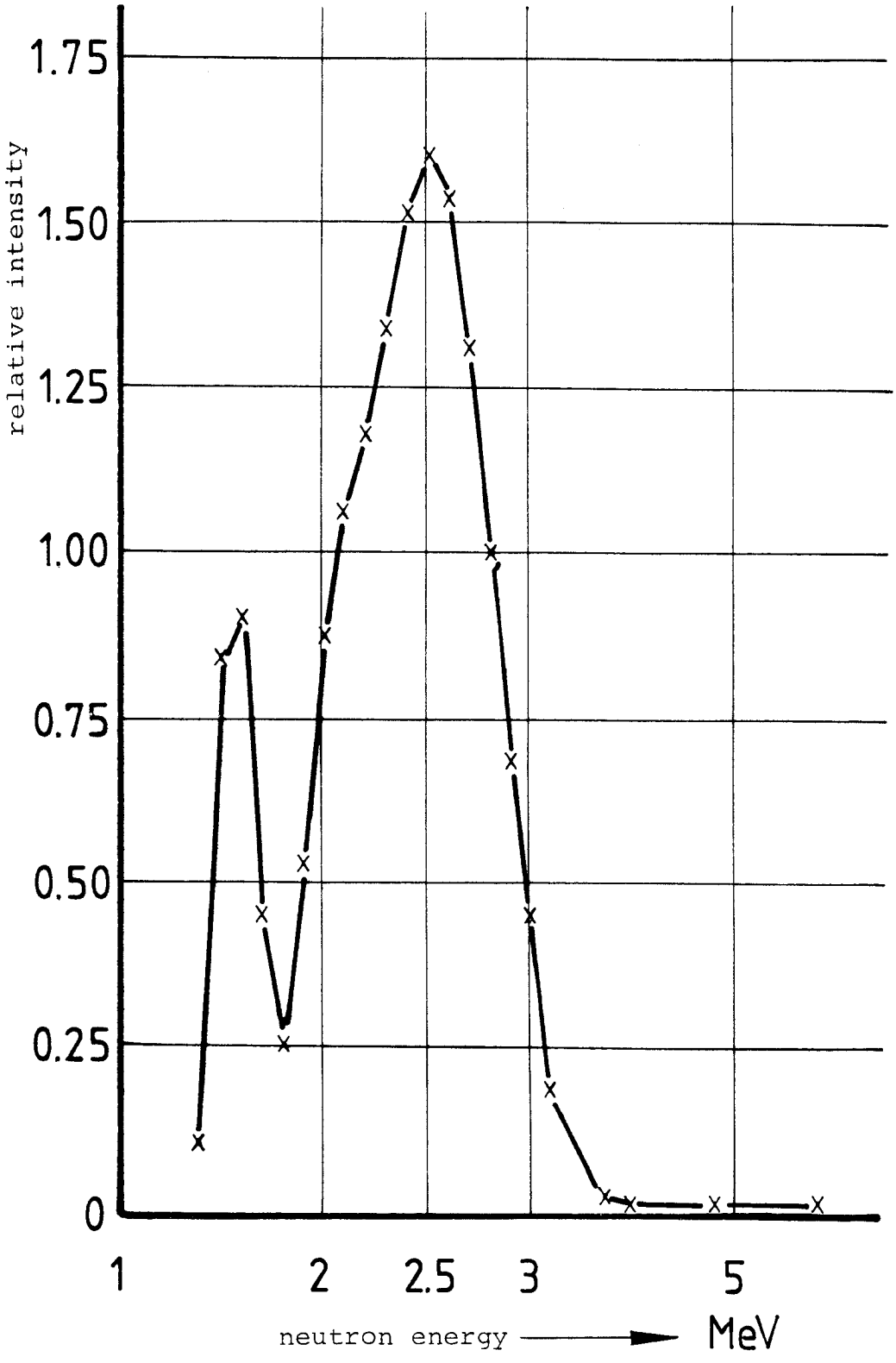

Fig. 5.14: Zeroth iteration neutron spectrum of D-D neutrons with the 2"x5" NE-213 detector

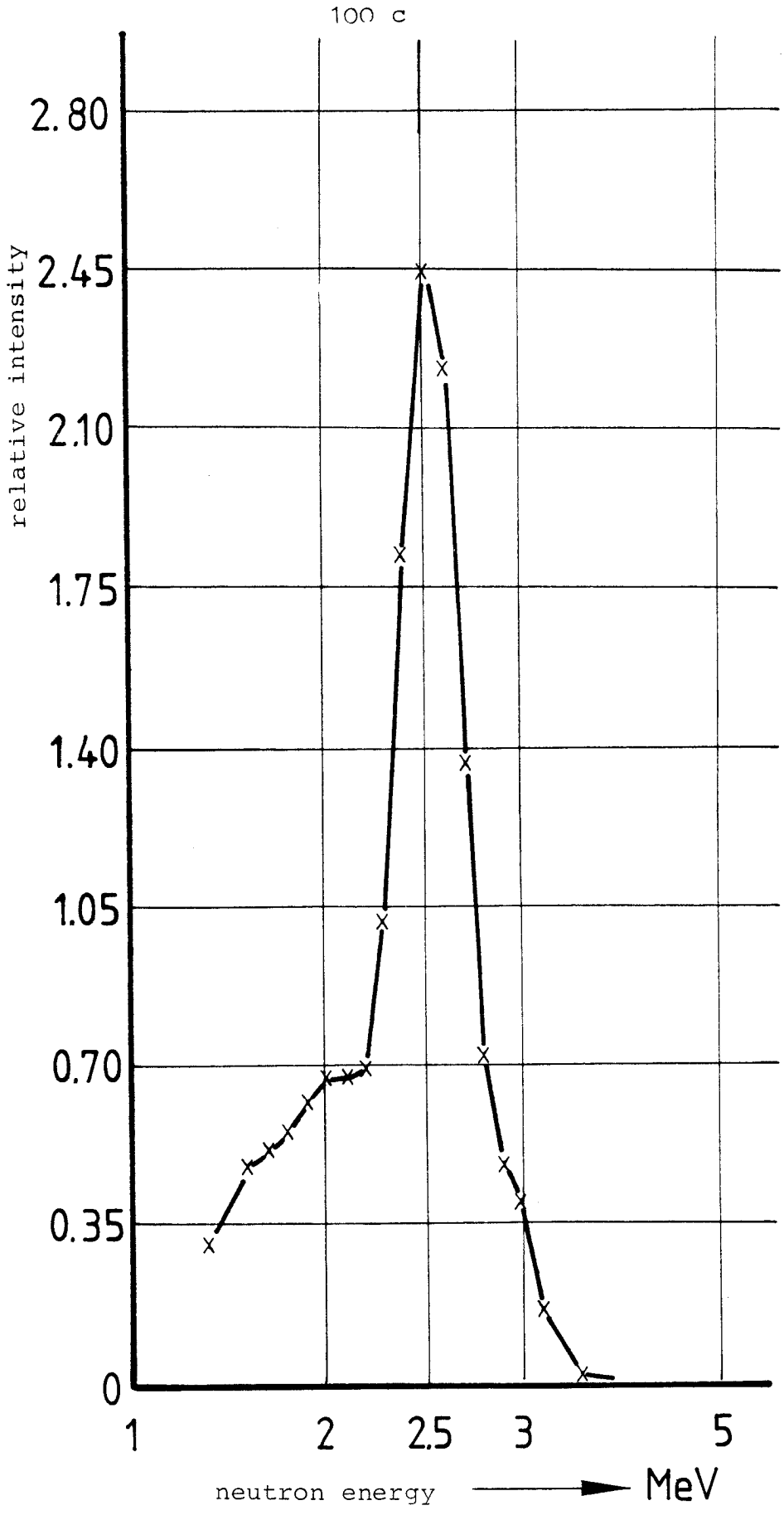

Fig. 5.15: First interation neutron spectrum of D-D neutrons with the 2"x2" NE-213 scintillator

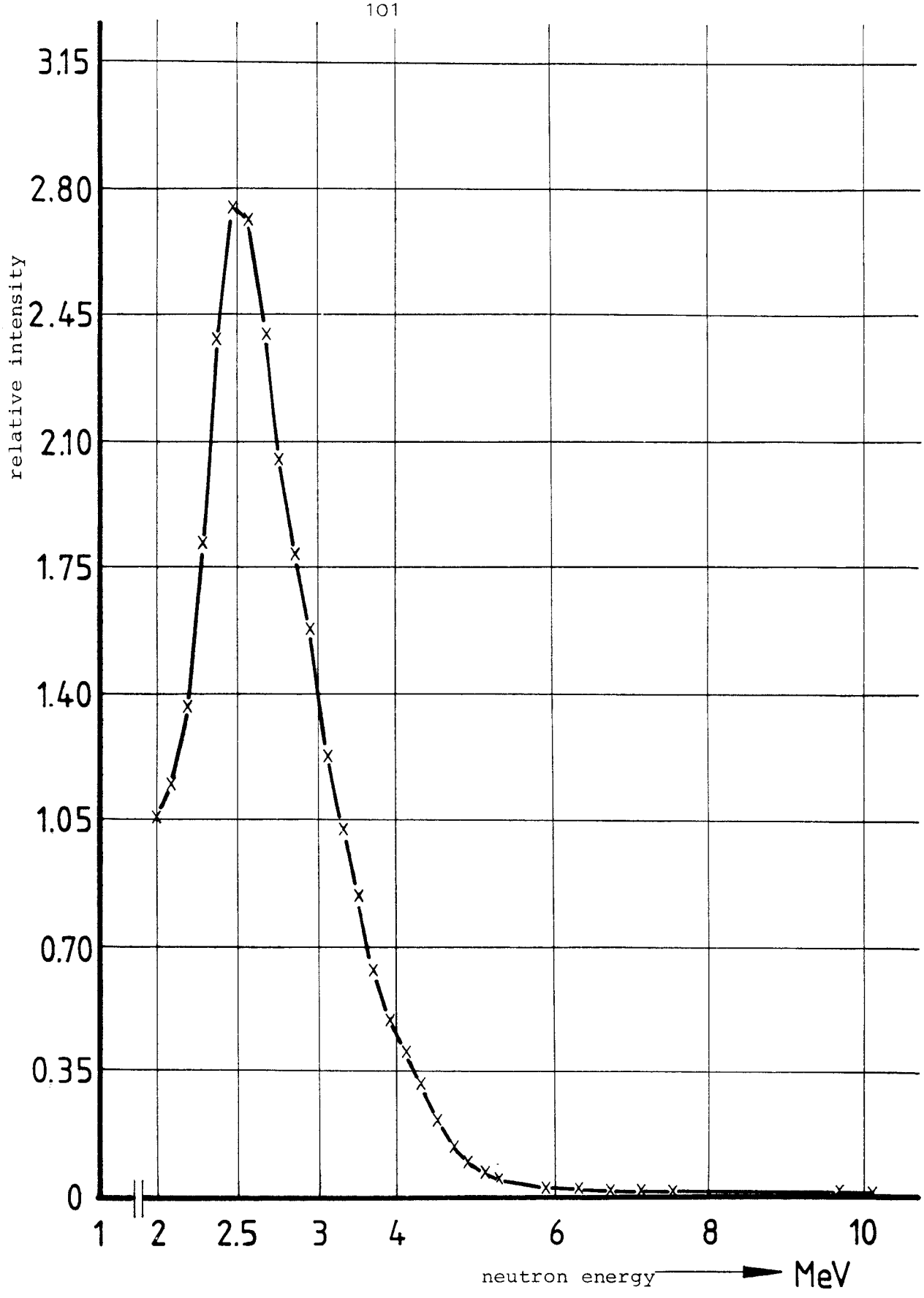

Fig. 5.16: First iteration neutron spectrum of D-D neutrons with the 2"x5" NE-213 scintillator

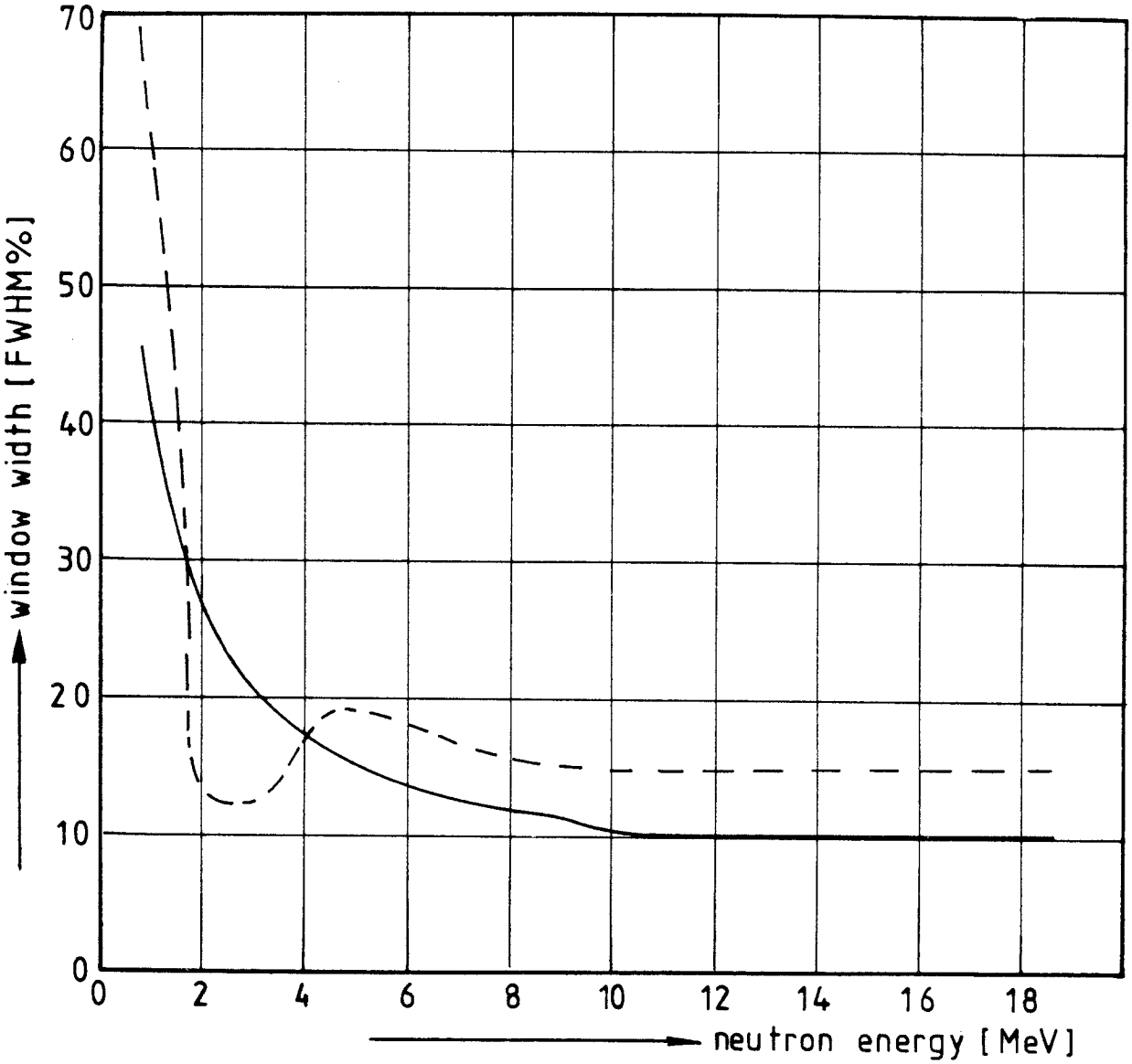

Fig. 5.17: Window widths used in modified FERDOR. The solid line is zeroth iteration set of window widths, while the dashed one is the first iteration window widths

6. HELIUM-3 SEMICONDUCTOR SANDWICH NEUTRON SPECTROMETER

6.1 Neutron Detector

The configuration of a neutron sensitive target surrounded on both sides by a semiconductor detector is most commonly used with ^{6}Li as the target. Less attention has been given to the use of ^{3}He as the target material. Yet, a comparison of the properties of ^{3}He- and ^{6}Li-semiconductor sandwich spectrometers reveals several attractive advantages of the former, the most important of which are:

1. Considerably higher efficiency at equal energy resolutions,
2. well-known shape of resonance-free cross section,
3. gaseous target.

These points should be briefly explained. The higher efficiency of the ^{3}He-spectrometer results from higher values of the ^{3}He-(n,p)t cross section and from the fact that in the ^{3}He-reaction only particles with one elementary charge are emitted whereas, in the $^{6}Li(n,\alpha)t$ reaction, also particles with two elementary charges are generated. Hence with the same resolution we can store much more reacting atoms in a ^{3}He- than in a ^{6}Li-spectrometer. As ^{6}Li cannot yet be used in its elemental form in such spectrometers. Combining all effects we get an efficiency which is 20-50 times higher than for a ^{6}Li-spectrometer /49/. This is very important, since the severest limitation of semiconductor neutron spectrometers is irradiation damage by fast neutrons which may change the properties of the diodes and thus require permanent control of the detector bias and time resolution. If ^{6}Li spectrometers are used, neutron fluences must be on the order of magnitude where radiation damage is felt (10^{14} n/cm^{2}) to get spectra with reasonable statistics, whereas these fluences are much more lower for ^{3}He-spectrometers.

For the interpretation of spectrum measurements primarily the shape of a cross section, not its absolute values, are of interest. For ^{3}He this shape was calculated with sufficient accuracy (2-5%) from the inverse reaction p(t,n) ^{3}He /53/, in the energy range between 10 keV and about 5 MeV.

In principle, the gaseous state of the target allows a correction to be made for energy losses of the reaction products in the target. These advantages of the ^{3}He-spectrometer are counteracted by disadvantages which must be overcome for the spectrometer to be used successfully for fast-neutron spectrum msurements. Since the reaction energy for the He^{3}(n,p)t reaction (764 keV) is much lower than for the $^{6}Li(n,\alpha)t$-reaction (4.78 MeV), gamma and neutron spectra are no longer separated, but overlap over a broad energy range, depending on the depletion depth of the semiconductor diodes and their geometry.

The ^{3}He(n,p)t-reaction with Q-value of 0.764 MeV leads to reaction products with energies E_p = 0.573 MeV and E_H = 0.191 MeV (in the case of thermal neutron). Several competing reactions must be considered in any detector based on this reaction The (n,p) reaction and simple elastic scattering of the neutrons from helium nuclei account for all the important features of ^{3}He detector response for all but the highest neutron energie ^{3}He spectrometer would not be useful beyond approximately 7 MeV because of the greater active volume needed in the detector to stop the high energy proton, this would cause even more Si (n,charged particle) background. Also, higher gas pressure would cause serious impairement of the resolution due to gas scattering. Therefore, this spectrometer is used to measure only D-D neutron spectrum where cross-section for the Si (n, charged particle) reactions are not overwhelming.

6.2 Electronic Circuit

The neutron spectrometer system, that includes a detector unit and a group of electronic modules, is shown in Fig. 6.1. The detector unit contains two surface-barrier detectors mounted in a face-to-face sandwich geometry. Between the two faces there is an active face separation of 1 mm which is filled with ^{3}He at a pressure of 5 atm as a neutron sensitive material.

The resulting pulses from the two detectors are amplified and shaped in two separate channels and then summed to produce a single pulse. Background counts are minimized by imposing fast coincidence and threshold restrictions, so that only those pulses that measure the total effect of each single neutron will be counted. The gated biased amplifier expands the portion of interest in the total energy spectrum and provides the input for the multichannel pulse height analyzer. Each detector output is furnished to a timing single-channel analyzer and the outputs from the two single-channel analyzers are examined in a fast coincidence circuit. The fast coincidence output controls a gate for the linear signal in the biased amplifier. A pulse generator is provided for calibrating and checking the system operation.

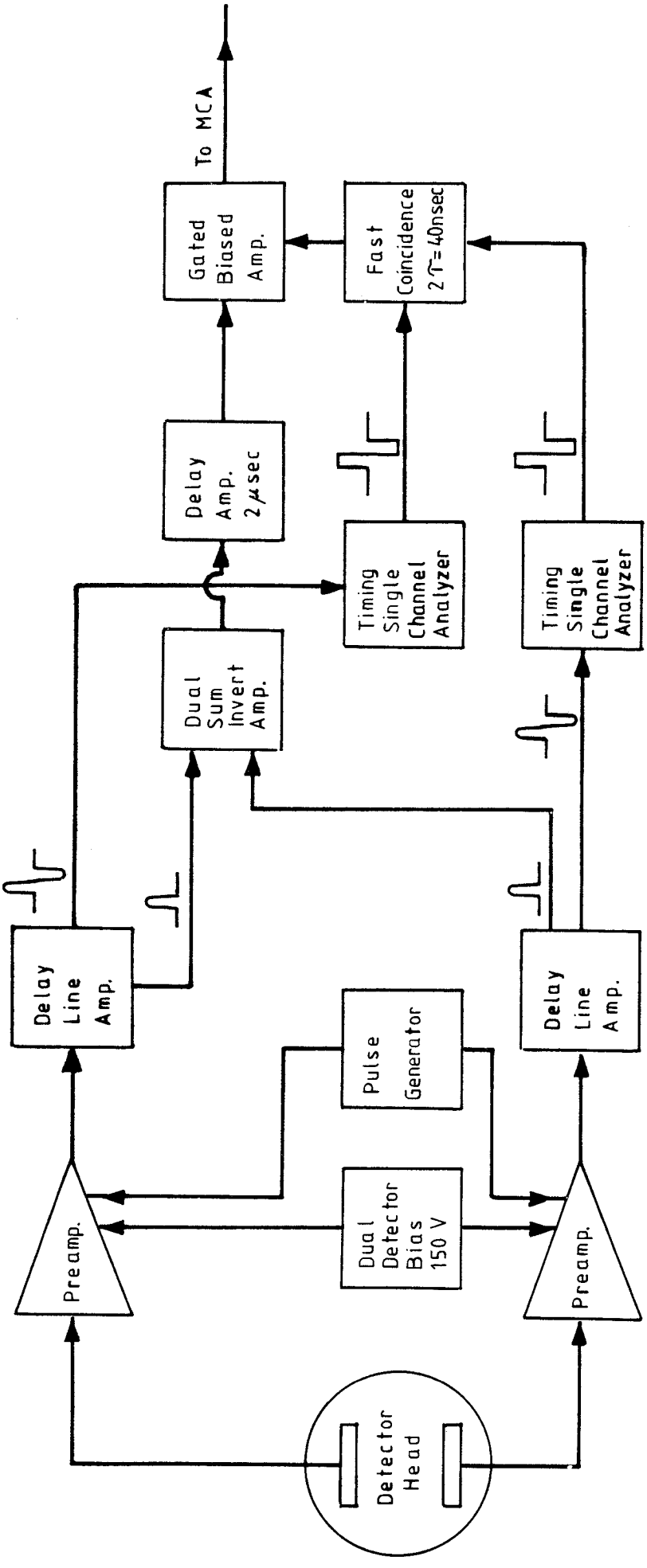

Fig 6.1 Neutron Spectrometer System Diagram

6.3 Energy Calibration

In order to calibrate the spectrometer system, a lithium semiconductor sandwich detector is used. The ^{6}Li (n,α)T reaction with Q-value of 4.78 MeV

$$^{6}_{3}Li + ^{1}_{0}n \rightarrow ^{3}_{1}H + ^{4}_{2}\alpha + Q$$

leads to reaction products with energies (for negligible incoming neutron energy).

$$E_{3H} = 2.73 \text{ MeV}, \quad E_{\alpha} = 2.05 \text{ MeV}$$

An Am-Be neutron source with suitable moderator material (Polyethylene) is used as thermal neutron source. The spectrum from the separate semiconductor detectors of both the ^{3}He- and ^{6}Li-sandwich detectors are obtained only for energy calibration. The triton line from the ^{3}He detector cannot be obtained because of its very low energy (0.191 MeV). Both of the triton line and the summed peaks line obtained from the ^{6}Li sandwich detectors are taken as points for energy calibration but the alpha line is not so sharp as those points. Photos of the spectrum obtained are shown in Fig. 6.2 and 6.3. In Fig. 6.4 the thermal peak of the ^{3}He (n,p)T reaction is shown with the pulse generator line which is a check for the system operation. The linearity of the spectrometer with both ^{3}He and ^{6}Li detectors is shown in Fig. 6.5.

6.4 Measurement of the Neutron Flux

As a source for 2.45 MeV monoenergy neutrons, a D-D neutron generator is used. In order to determine the neutron flux of this neutron generator, the arrangement shown in Fig. 6.6 is prepared. Ten foils of In-115m are distributed equally around

the Al circle. Indium is particularly well suited as an activation detector for 2.5 MeV neutrons since the ^{115}In (n,n') ^{115m}In is a threshold reaction whose cross section falls just below a neutron energy of 2.5 MeV and has its maximum about this energy /54,55/. Due to the nature of this cross section, activation by scattered neutrons is of reduced importance since the scattering process tends to reduce the neutron's energy below the threshold. The activity of each foil is measured. The radioactivity is identified by measurement of the gamma emission unique to each decaying radionuclide. The gamma spectra were measured with a high resolution Ge(Li) γ-spectrometer. The result is shown in Fig. 6.7. Neutron scattering and absorption out of infoils is neglected in the calculation of neutron flux and this gives a rough estimate of about 20 %. Under the operating conditions up to 3.7×10^8 neutrons/sec are produced.

6.5 Measurement with Neutron Generator

In order to determine the resolution and efficiency of the spectrometer system, a series of measurements were made with the D-D neutron generator. The neutron spectrum was measured at different beam to neutron emission angles. These angles were 0^o, 45^o, 90^o, 135^o. At angle 90^o the energy of the neutrons is 2.42 MeV. The dependence of neutron energy on the angle is shown in Fig. 6.8.

In Fig. 6.9 is shown the line width of the neutron peaks at different angles, it is clear that the best result is at angle 90^o with line width 50 keV full width at half maximum. The energy resolution is found to be 2 % at angle 90^o (Fig. 6.10). The change of efficiency with angle gives the best efficiency at angle 90^o of about 0.9×10^{-6} as shown in Fig. 6.11. Photos of the different neutron spectrum obtained are shown in Figs. 6.12-6.15.

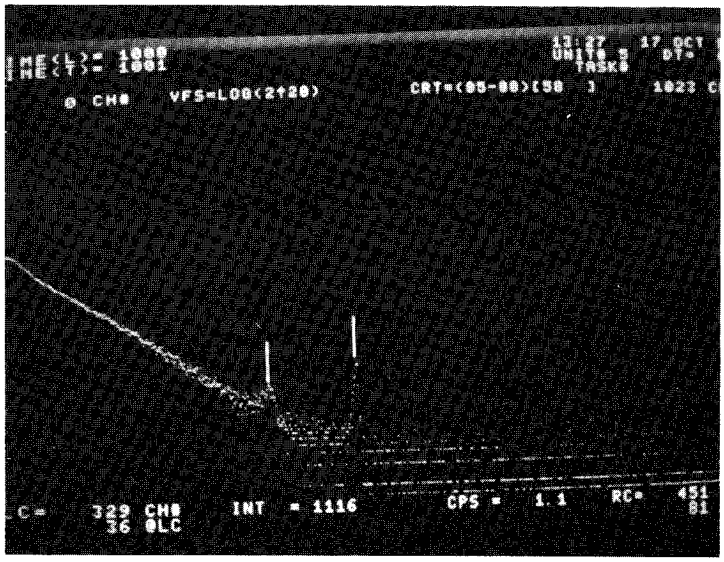

Fig. 6.2: Pulse height spectrum of the separate alpha and triton peaks of the ^{6}Li (n,α)T reaction

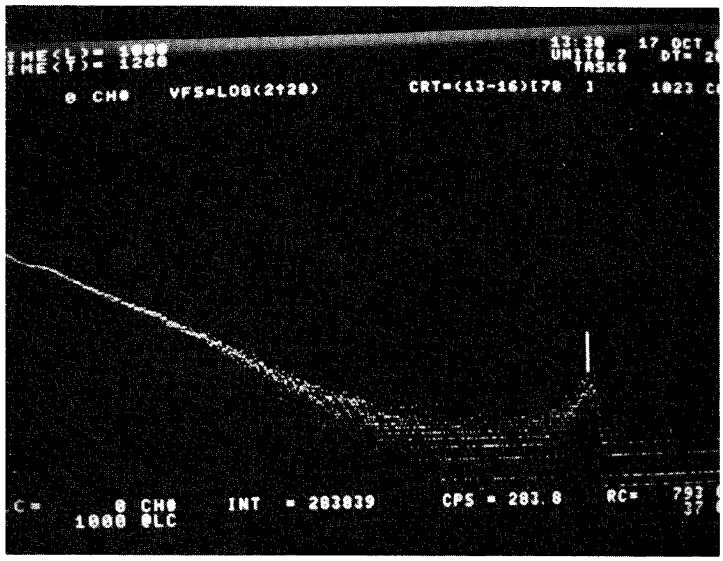

Fig. 6.3: Pulse height spectrum of the summed peak of the ^{6}Li (n,α)T reaction

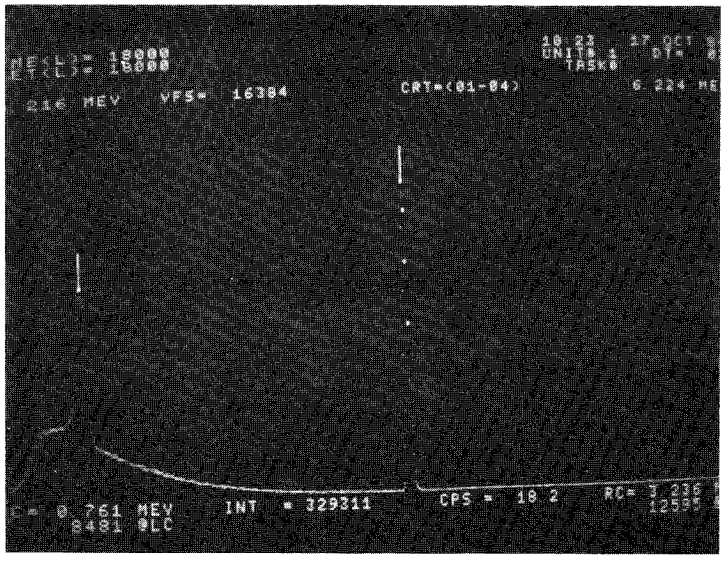

Fig. 6.4: Pulse generator line with a fwhm of about 20 keV and thermal peak of the $^{3}He(n,p)T$ reaction with a fwhm of about 40 keV

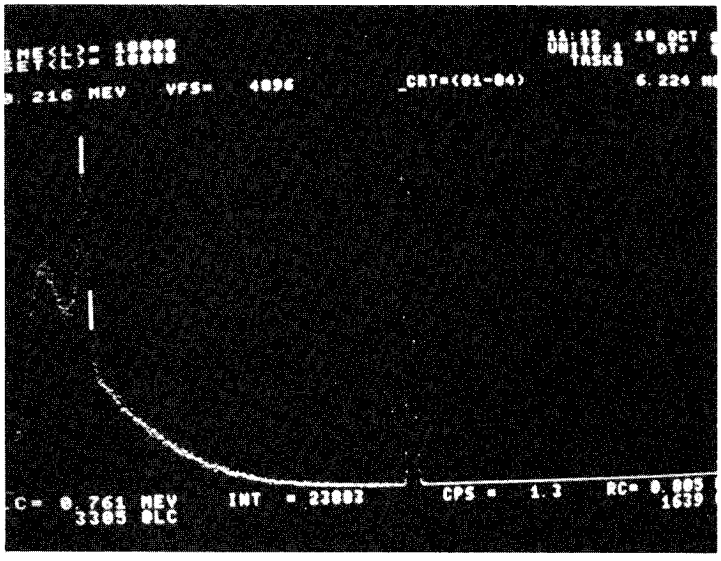

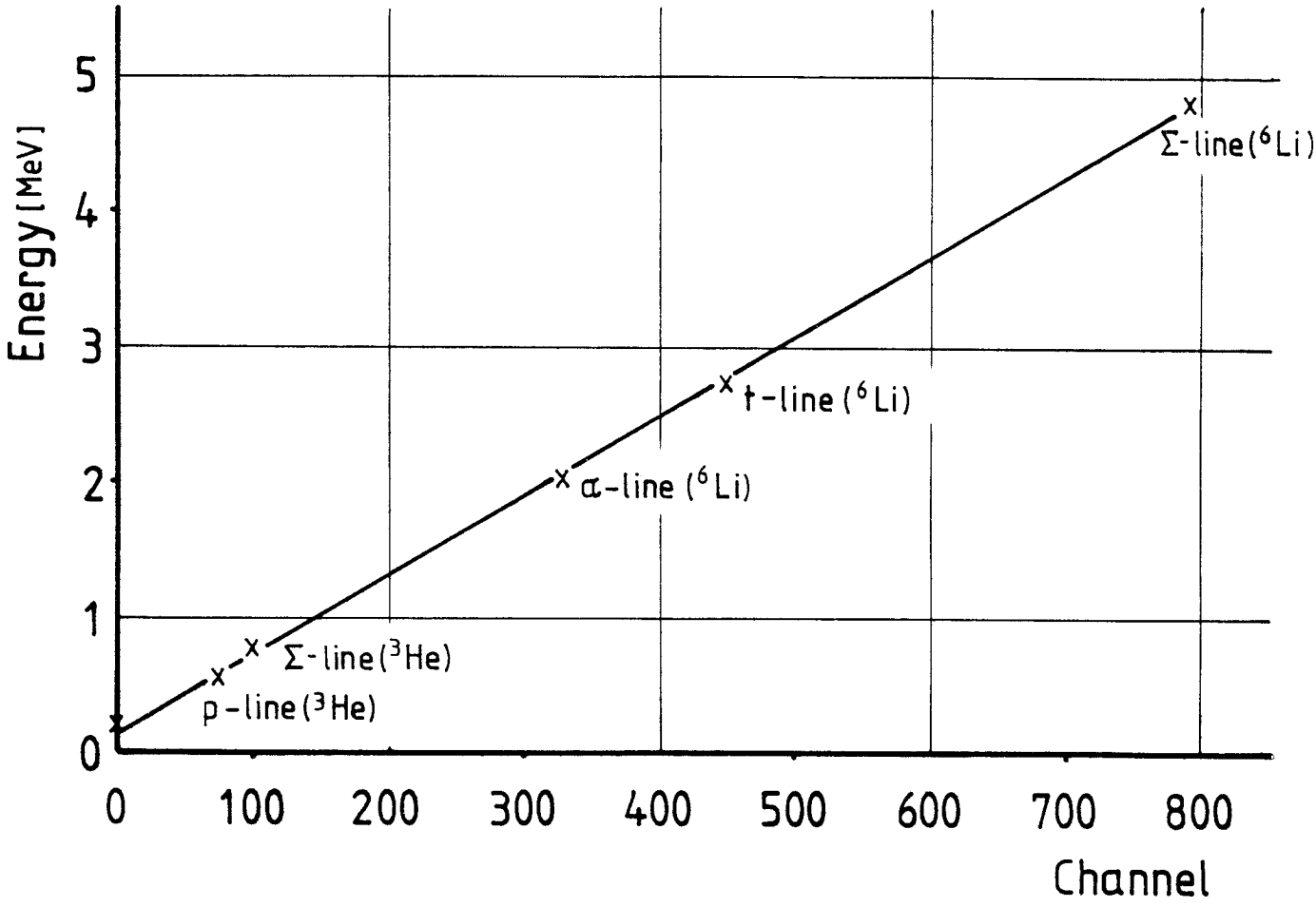

Fig 6.5 Linearity of the spectrometer with both ^{3}He and ^{6}Li detectors

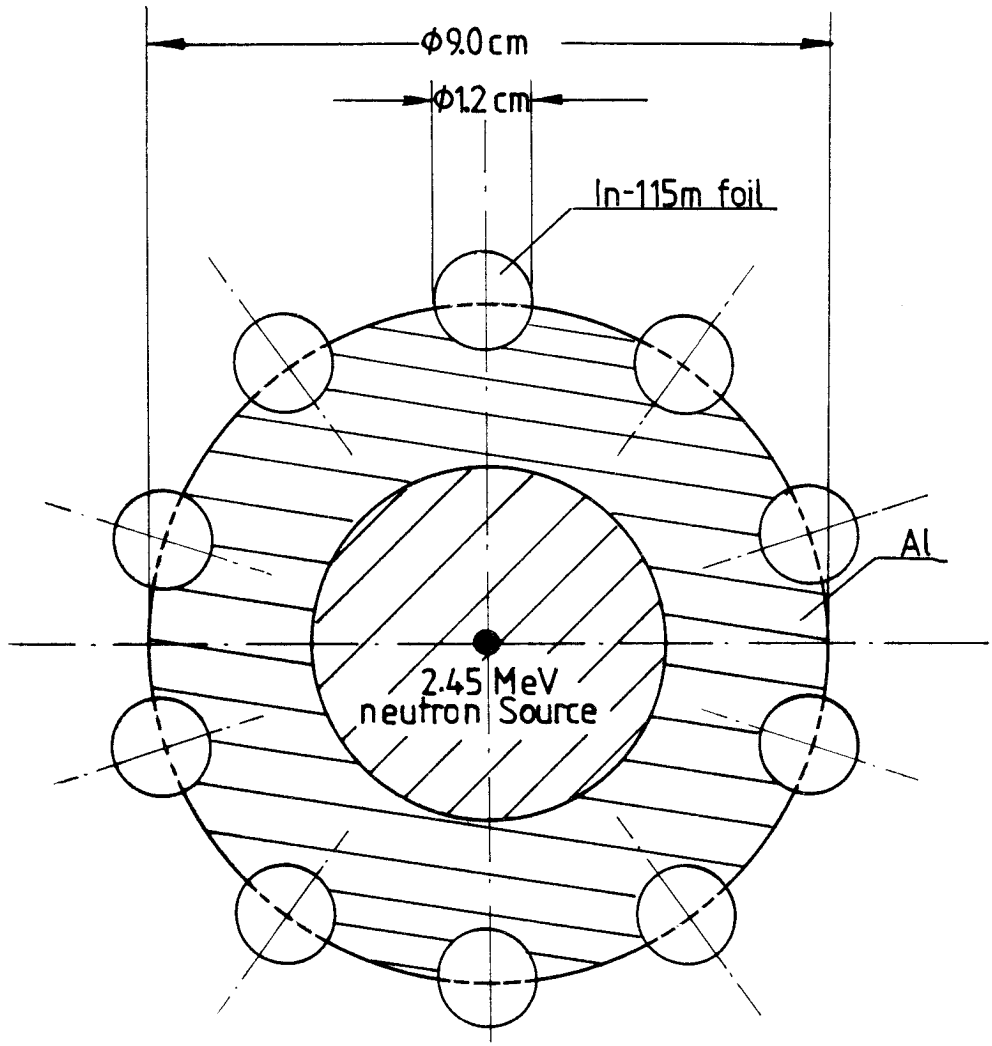

Fig 6.6 Arrangement to measure the neutron source output

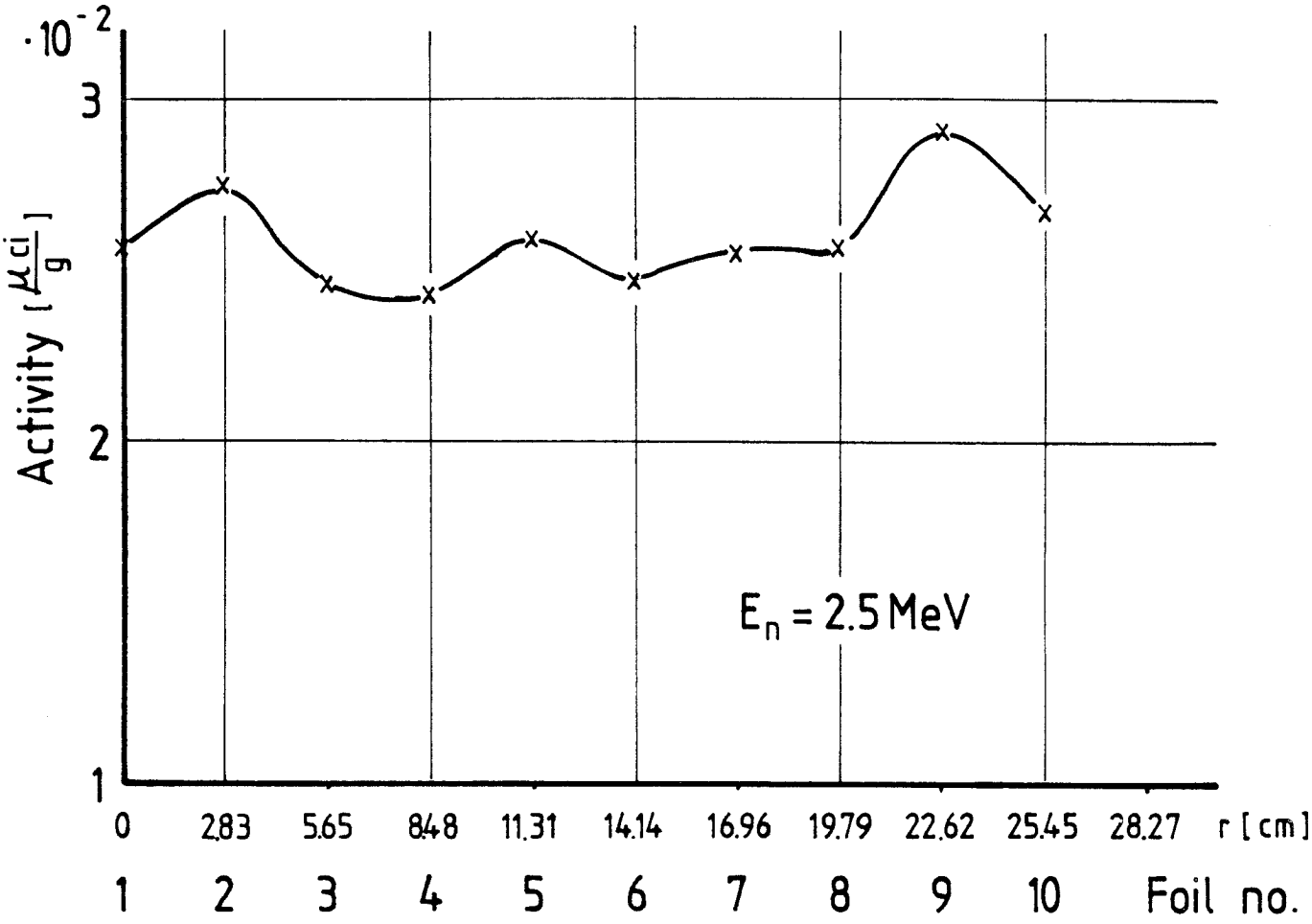

Fig 6.7 The specific activity of ^{115m}In foils

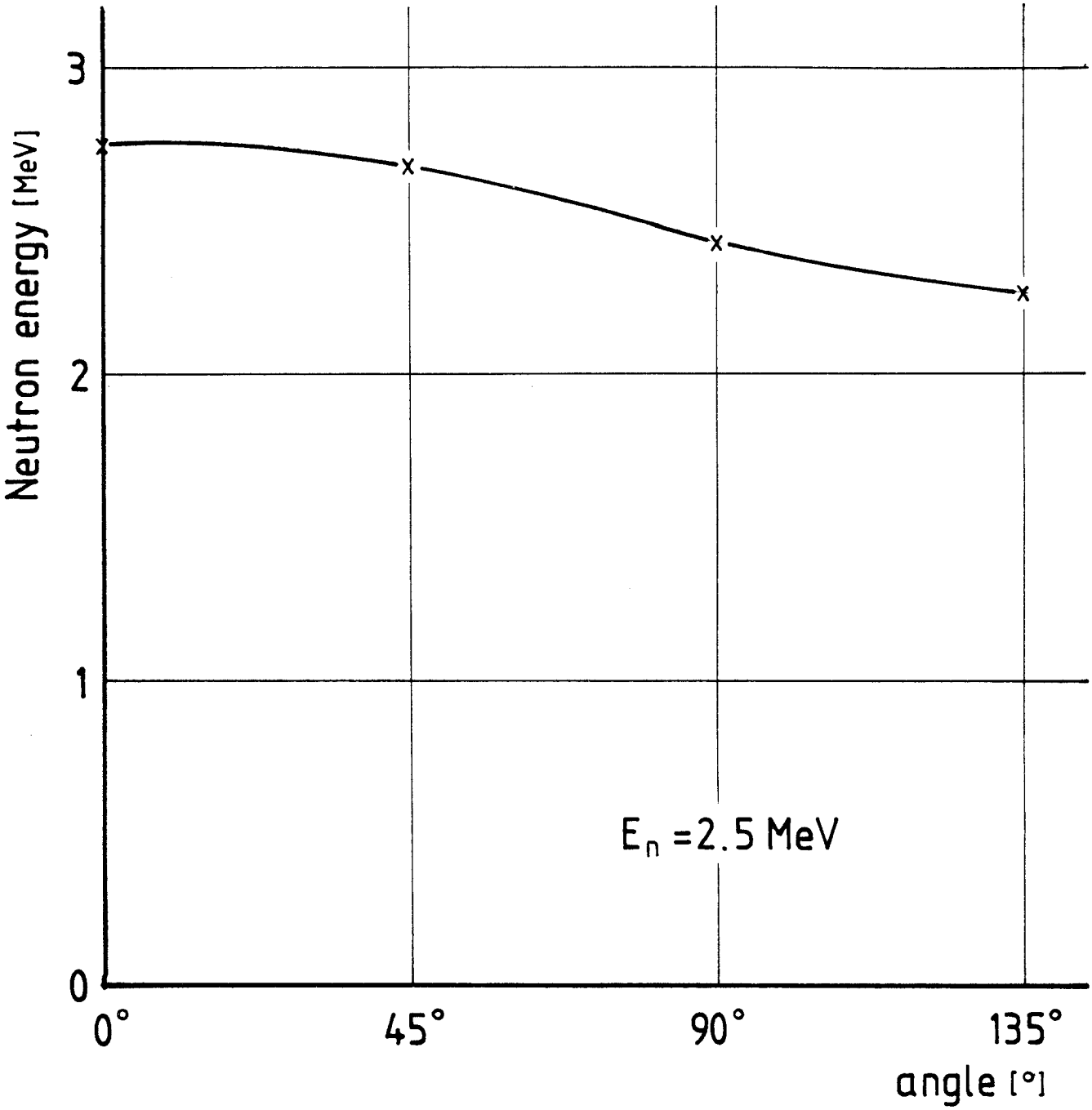

Fig 6.8 The energy of D-D neutrons from neutron generator as a function of the angle of detector position w.r.t. neutron emission direction (α)

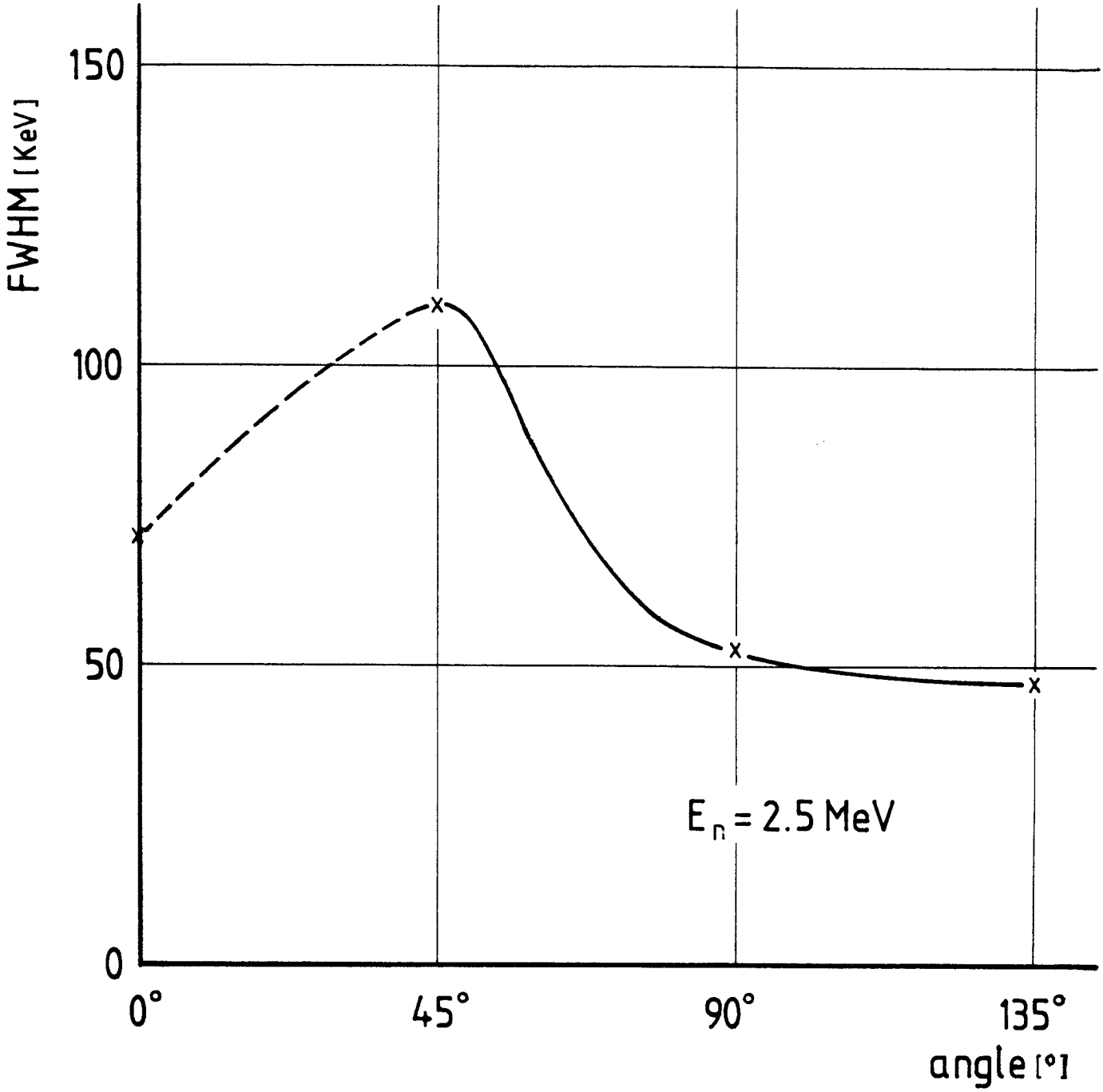

Fig 6.9 The FWHM of neutron lines at different angles

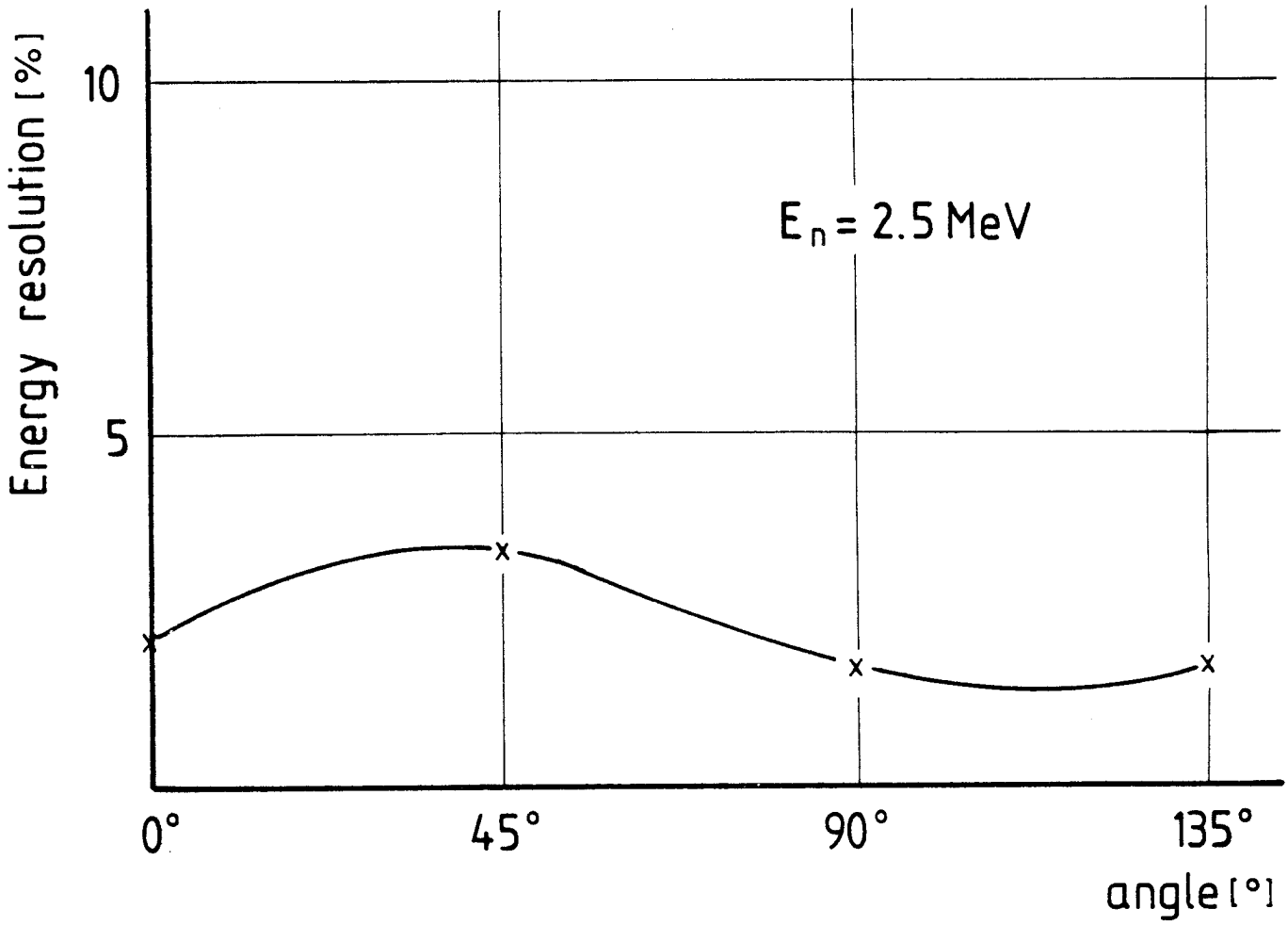

Fig 6.10 The energy resolution of the spectrometer at different angles

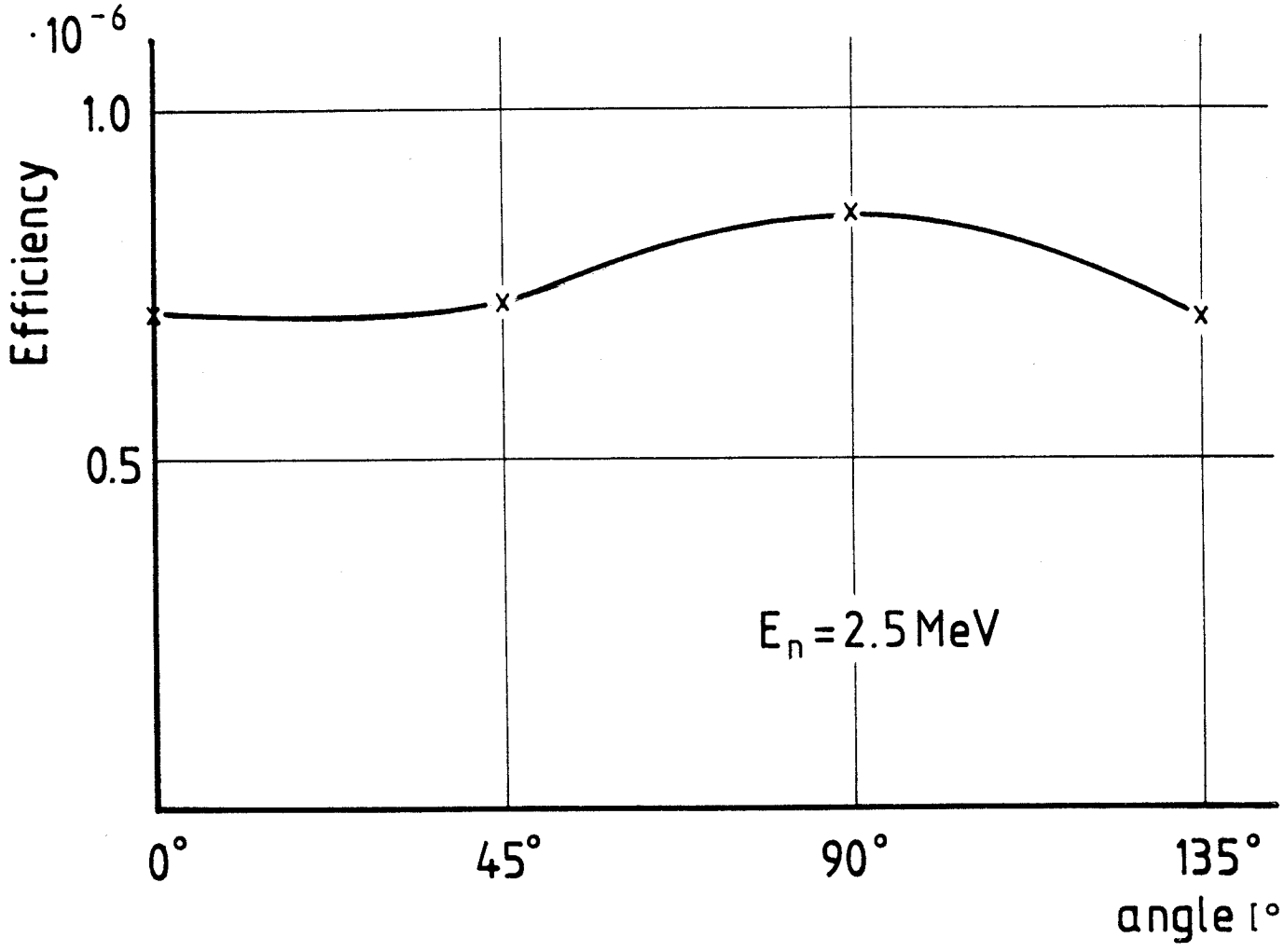

Fig 6.6 The efficiency of the spectrometer at different angles

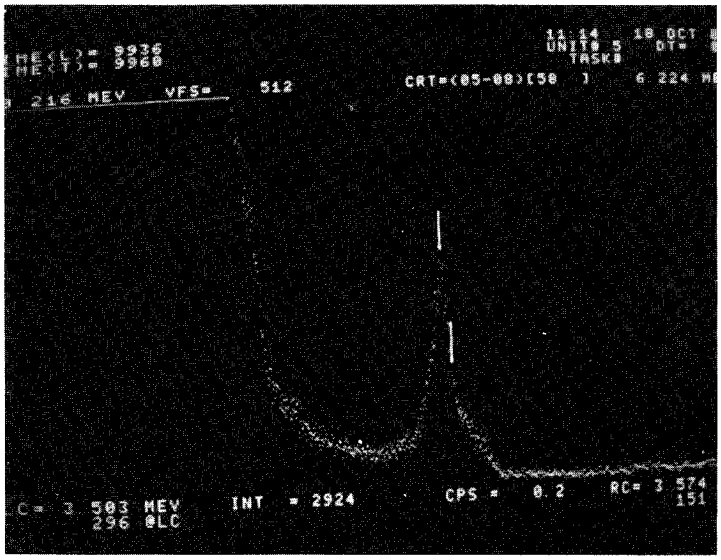

Fig. 6.12: The D-D neutron line at angle 0^{o}

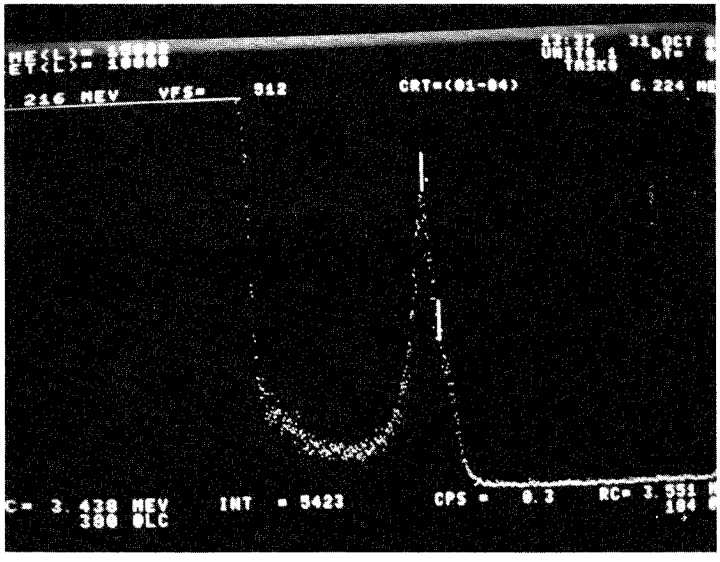

Fig. 6.13: The D-D neutron line at angle 45^{o}

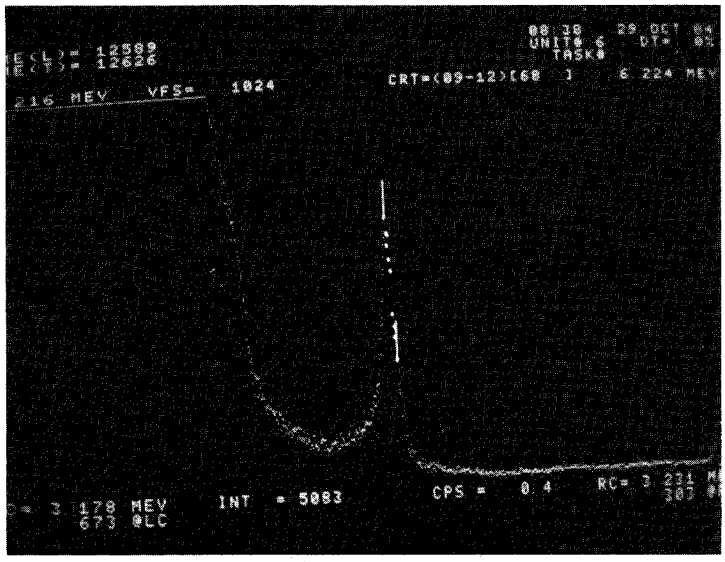

Fig. 6.14: The D-D neutron line at angle 90^{o}

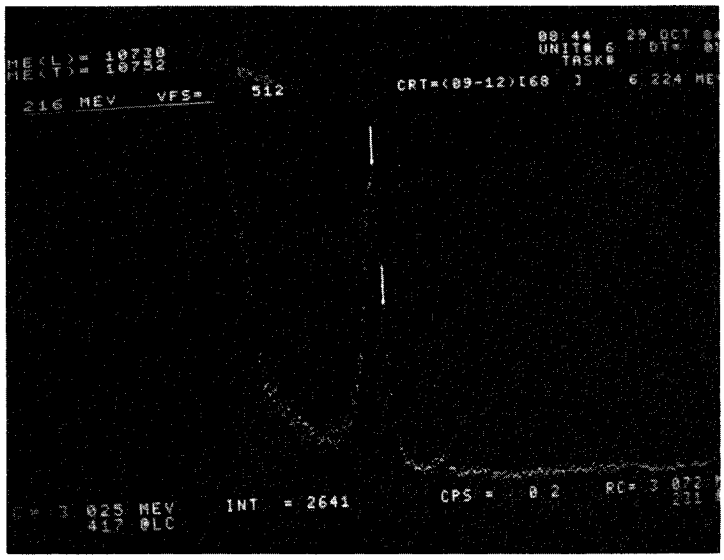

Fig. 6.15: The D-D neutron line at angle 135^{o}

7. SUMMARY

The present work introduces two possible systems of spectrometers to be used for observing the neutrons emitted from fusion plasmas, with the objective of deducing the optimum amount of information concerning the parameters of the reacting plasmas, in particular, the temperature and density. As mentioned before, good energy resolution with suitable efficiency is an essential feature of the diagnostic system.

An NE-213 neutron spectrometry system, with two different detector sizes, was assembled for measurements of D-D and D-T neutron spectra. The spectrometers were calibrated and used to measure the pulse height distribution for several neutron sources. Pulse shape discrimination against gamma ray events was used. The efficiencies and response functions were calculated with CECIL Monte Carlo code. Several improvements have been made for the Monte Carlo code to agree with the measurements of the spectrometers. A "Rubber Sheet" was used to generate a response matrix for each detector using the Monte Carlo calculations and suitable binning structure. Neutron energy spectra were obtained by unfolding the measured pulse height spectra. A modified version of the FERDOR unfolding code have been used in unfolding the present measurements. It was obvious that the thick detector has the advantage of higher efficiency than that of the smaller one, while the latter has the advantage of better energy resolution for both D-D and D-T neutrons.

The second spectrometer system used a ^{3}He semiconductor sandwich detector to measure the neutron spectrum for D-D neutrons. The spectrometer was calibrated and the neutron energy spectra were measured to determine the energy resolution, while the detector efficiency was calculated. Actually, it must be stressed that the ideal spectrometer, i.e. that spectrometer which has a high efficiency together with a high energy resolution

and which can explore a wide energy range, does not exist since those features do not jointly exist. Consequently a choice must be made between those characteristics.

The ^{3}He spectrometer has a high energy resolution of about 50 keV full width at half maximum at 2.45 MeV with the advantage of getting the neutron spectrum directly from the measurement, i.e. it needs no unfolding as the NE-213 detector. The lower efficiency of this spectrometer, about 10^{-6} together with the difficulty to discriminate against gamma rays are the most important disadvantages. The poor resolution of the NE-213 scintillator is compensated for by the possibility of getting the 2.45 MeV and the 14 MeV neutron spectra with the same spectrometer and primarily by the opportunity of achieving higher counting rate.

One of the most important features of the fusion neutron source is its time duration which is rather short in the experiments carried out until now it has reached few seconds. With ion temperature of about 2 keV to 3 keV the neutron production rate in a Tokamak is so low that a single discharge (shot) is not enough to obtain sufficiently accurate results. Typically, a series of several similar discharges or some tens of discharges or even more will be needed to get a reasonable spectrum.
A neutron output of about 10^{8} $n/cm^{3}/sec$ with temperature of one keV and one second plasma discharge will be needed to measure a useful D-D neutron spectrum with the ^{3}He spectrometer in one discharge. With the NE-213 spectrometer, neutron output of 10^{6} $n/cm^{3}/sec$ with 1.5 keV temperature are the fusion plasmas conditions required to measure a D-D neutron spectrum while for D-T neutron spectrum, lower plasma temperature (about 1 keV) with the same discharge duration are good conditions to get useful information about the density and temperature of the plasma from such spectra.

REFERENCES

/1/ G. Lehner, F. Pohl, Garching-Report, IPP 1/60 (1967)

/2/ O.N. Jarvis, AERE G 1644, January 1980

/3/ D.L. Book, "NRL Plasma Formulary", 1978 revised

/4/ D.W. Muir, LA-5411-MS (1973)

/5/ W.A. Fischer et al., Nucl.Instr. and Meth. 219 (1984) 179

/6/ G.L. Morgan, A.C. England, Nucl.Instr. and Meth. 129 (1975) 1

/7/ J.D. Strachem et al., "Joint Varena-Grenoble International Symposium on Heating in Toroidal Plasma", Grenoble 1 (1978) 25

/8/ J.D. Strachem et al., Nature (London) 279 (1979) 626

/9/ W.A. Fisher et al., Nucl.Instr. and Meth. 219 (1984) 179

/10/ M. Chatelier, I. Ihmtal, A. Lagattu, A. Lepers, Nucl.Instr. and Meth. 190 (1981) 107

/11/ D.S. Pappas, F.J. Wysocki, R.J. Furnstahl, MIT Report, PFC/RR-82-14 (1982)

/12/ D.R. Slaughter, H.S. Spracklen, R. Delvasto, Nucl.Instr. and Meth. 215 (1983) 443

/13/ F. Hoenen, Nucl.Instr. and Meth. 223 (1984) 150

/14/ T.H. Elevemt, M. Olsson, Nucl.Instr. and Meth. A240 (1985) 383

/15/ P. Sperr, H. Spieler, M.R. Maier, D. Evers, Nucl.Instr. and Meth. 116 (1974) 55

/16/ J. Kasagi, T. Murakami, T. Inamura, Nucl.Instr. and Meth. A236 (1985) 426

/17/ H.H. Knox, T.G. Miller, Nucl.Instr. and Meth. 101 (1972) 519

/18/ K.F. Flynn, L.E. Glendenin, E.P. Steinberg, P.M. Wright, Nucl.Instr. and Meth. 27 (1964) 13

/19/ N.A. Lurie, L. Harris, Jr., J.C. Young, Nucl.Instr. and Meth. 129 (1975) 543

/20/ J.B. Birks, "The Theory and Practice of Scintillation Counting", Pergamon Press (1964)

/21/ S.T. Stanton, COO-1545-92 (February 1971)

/22/ R.A. Cecil, B.D. Anderson, R. Madey, Nucl.Instr. and Meth. 161 (1979) 439

/23/ W.W. Lindstrom, B.D. Anderson, Nucl.Instr. and Meth. 98 (1972) 413

/24/ S.T. Thornton, J.R. Smith, Nucl.Instr. and Meth. 96 (1971) 25

/25/ M. Drosg, Nucl.Instr. and Meth. 105 (1972) 573

/26/ V.V. Verbinski, W.R. Burrus, T.A. Love, W. Zobel, N.W. Hill, Nucl.Instr. and Meth. 65 (1968) 8

/27/ W.R. Burrus, R.M. Freestone, ORNL-TM-2594 (1969)

/28/ W.R. Burrus, V.V. Verbinski, Nucl.Instr. and Meth. 67 (1968) 181

/29/ H. Kendrick, S.M. Sperling, Gulf Radiation Technology, GA-9882 (1970)

/30/ H. Kendrick, L. Harris, Jr., Gulf Radiation Technology, Gulf-RT-A10821 (1971)

/31/ W.R. Burrus, Oak Ridge National Laboratory, ORNL-3743 (1965)

/32/ C.E. Clifford et al., Nucl.Sci.Eng. 27 (1967) 299

/33/ E.A. Straker, Nucl.Sci.Eng. 34 (1968) 114

/34/ R.E. Maerker, Oak Ridge National Laboratory, ORNL-TM-3871 ENDF-170, revised (1972)

/35/ W. Meyer et al., Department of Nuclear Engineerng, Kansas State University, COO-2049-10 (1971)

/36/ W. Meyer, D.W. Prigel, Trans.Am.Nucl.Soc. 16 (1973) 361

/37/ V.V. Verbinski, W.R. Burrus, Phys.Rev. 177 (1969) 1671

/38/ W. Meyer, W.H. Miller, Trans.Am.Nucl.Soc. 21 (1975) 535

/39/ B.W. Rust, D.T. Ingersoll, W. Burrus, Oak Ridge National Laboratory, ORNL/TM/8720 (September 1983)

/40/ R.H. Johnson, Urbana-Champaign, Ill, University of Illinois, Diss. (1975)

/41/ H. Kendrick, L. Harris, Gulf Radiation Technology, Gulf-RT-A10821 (1971)

/42/ H. Kendrick, S.M. Sperling, Gulf Radiation Technology, GA-9882 (1970)

/43/ E.A. Lorch, International Journal of Applied Radiation and Isotopes 24 (1973) 585

/44/ P. Cloth, R. Hecker, Nukleonik 12 (1969) 163

/45/ H. Werle, Nucl.Res. Centre Karlsruhe, Report INR-4/70-25 (1970)

/46/ H.B. Greiss, Nukleonik 10 (1968) 283

/47/ B.F. Walts, Phys.Rev. 87 (1952) 1037

/48/ G.F. Knoll, "Radiation Detection and Measurement", John Willey & Sons (1979)

/49/ H. Bluhm, Nucl.Instr. and Meth. 115 (1974) 325

/50/ T.R. Jeter, M.C. Kennison, IEEE Trans.Nucl.Sci, NS-14(1), (1967) 422

/51/ M.E. Lee, M.L. Awcock, Neutron Dosimetry, Vol. 1, (IAEA Proc., Vienna 1963) 441

/52/ T.R. Herold, Nucl.Instr. and Meth. 71 (1969) 46

/53/ J. Als-Nielsen, CCDN-NW/6 (1967)

/54/ H. Liskien et al., Nucl.Sci.Eng. 67 (1978) 334

/55/ G. Zankl et al., Nucl.Instr. and Meth. 185 (1981) 321

/56/ T.W. Armstrong, K.C. Chandler, Nucl. Instr. and Meth. 113 (1973) 313

APPENDIX

A. Layout of the NE-213 scintillator calculations

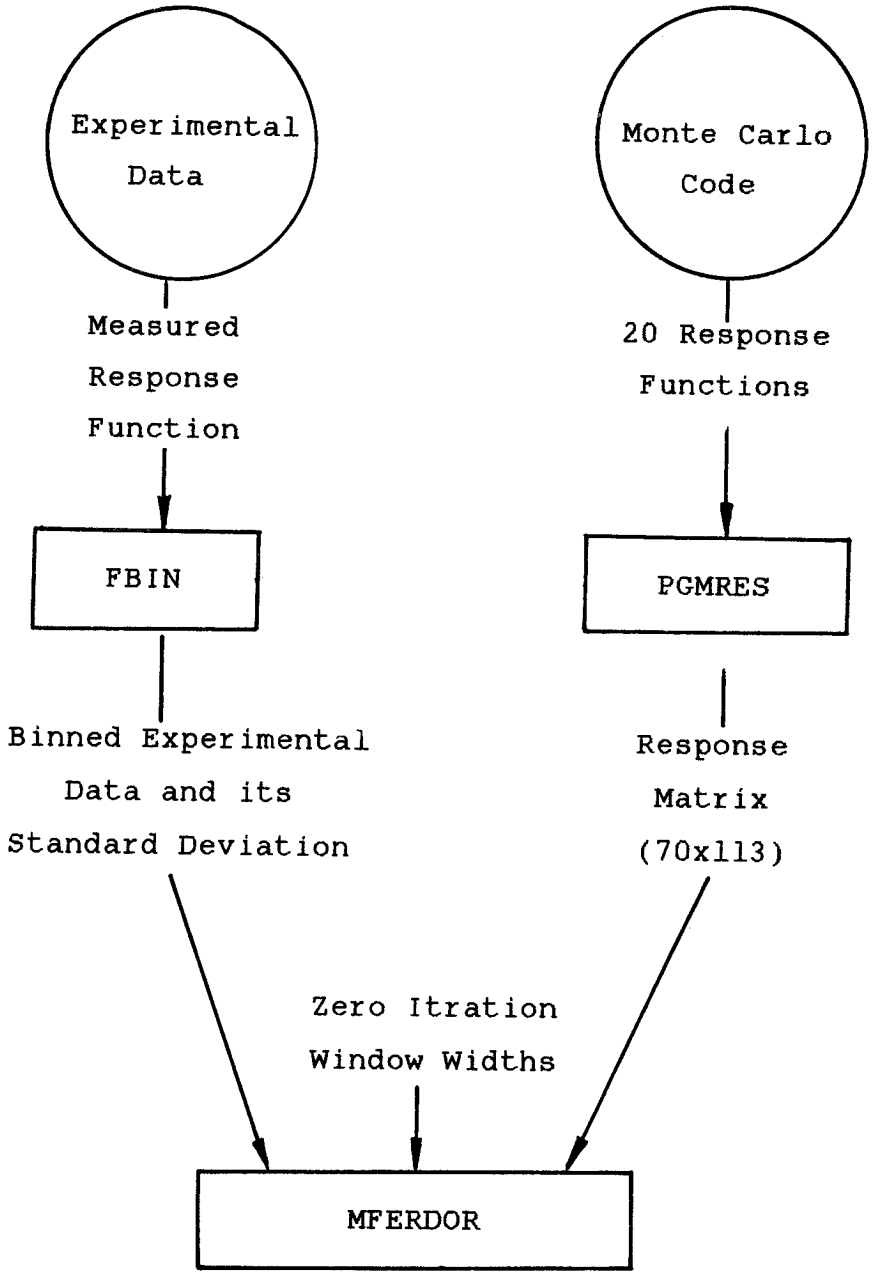

General flow diagram of the NE-213 scintillator calculations